Charles University in Prague
Faculty of Mathematics and Physics

DOCTORAL THESIS

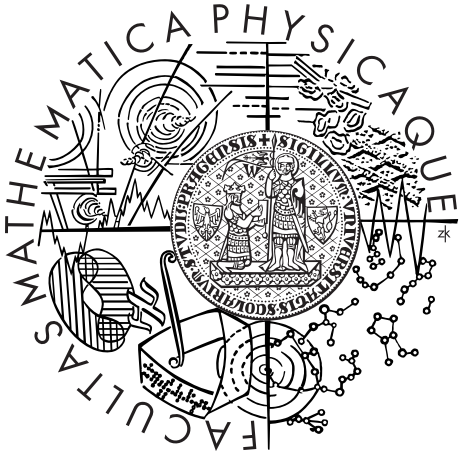

Jiří Eliášek

Low-energy processes in H + H$^-$ collision

Institute of Theoretical Physics

Supervisor of the doctoral thesis:	doc. RNDr. Martin Čížek, Ph.D.
Study programme:	Physics
Specialization:	Theoretical Physics, Astronomy and Astrophysics

Prague 2014

I would like to thank Ivana Paidarová for providing unpublished data for potential curves of $^2\Sigma_g^+$ state.

My thanks also belong to Štěpán Roučka et al. for providing us with unpublished results of their measurement of reaction rate for charge transfer.

The help of my supervisor Martin Čížek is greatly appreciated. This work wouldn't exist without him and without large quantity of matcha tea that was consumed during my work on this thesis. I would like also to thank to my colleagues at the Institute of Theoretical Physics for their support and advices.

This work was partially supported by Grant No. GACR 208/10/1281 of the Czech Science Foundation.

I declare that I carried out this doctoral thesis independently, and only with the cited sources, literature and other professional sources.

I understand that my work relates to the rights and obligations under the Act No. 121/2000 Coll., the Copyright Act, as amended, in particular the fact that the Charles University in Prague has the right to conclude a license agreement on the use of this work as a school work pursuant to Section 60 paragraph 1 of the Copyright Act.

In ..... date ..... signature of the author

Název práce: Nízkoenergetické procesy při srážce H + H^-

Autor: Jiří Eliášek

Katedra: Ústav teoretické fyziky

Vedoucí disertační práce: doc. RNDr. Martin Čížek, Ph.D., Ústav teoretické fyziky

Abstrakt: V této práci se zabýváme teoretickým popisem srážek atomu vodíku s vodíkovými anionty při nízkých energiích. Pro tento systém jsme rozšířili stávající model pro nelokální rezonanční dynamiku o další diskrétní stav a dvě k němu příslušející kontinua. Provedli jsme numerické výpočty účinných průřezů asociativního odtržení elektronu, jež hraje důležitou roli v modelech raného vesmíru. Přidáváme účinné průřezy pro kolizní odtržení a ukazujeme spektra odlétávajících elektronů. Ukazujeme, jak se v této reakci projeví izotopický efekt. Zabýváme se přenosem náboje a elastickým rozptylem při srážce vodíku a deuteriového aniontu. Naše výsledky porovnáváme s aktuálními experimenty a diskutujeme jejich spolehlivost.

Klíčová slova: srážka H + H^-, asociativní odtržení, přenos náboje, isotopický efekt

Title: Low-energy processes in H + H^- collision

Author: Jiří Eliášek

Department: Institute of Theoretical Physics

Supervisor: doc. RNDr. Martin Čížek, Ph.D., Institute of Theoretical Physics

Abstract: In this work we generalize existing theory of low-energy collisions of atomic hydrogen with its anion. We extend the non-local resonance model for this system by adding new discrete state and two continua that are coupled with it. We calculate numerically cross sections for associative electron detachment process that is important for models of early universe. We add cross section for collision detachment and show spectra of outgoing electrons. We show how the isotopic effect is involved in studied collision. We also calculate charge transfer, elastic scattering cross sections, and reaction rates for hydrogen collisions with deuterium anion. We compare our results with recent experiments and we discuss their reliability.

Keywords: H + H^- collision, associative detachment, charge transfer, isotopic effect

Contents

1. Introduction

In this thesis we will be interested in collisions of atoms with negative ions. Since our primary interest lies in theory, we consider both atoms and ions with small proton number. These reactions are interesting as the systems are small enough to be accurately described using the most advanced ab initio methods. In the same time they are complicated enough to produce interesting and sometimes unexpected physics. The reactions occurring in such collisions at low energies can be classified as associative detachment (AD)

$$\mathrm{A} + \mathrm{B}^- \rightarrow \mathrm{AB} + \mathrm{e}^-, \tag{1.1}$$

collision detachment (CD)

$$\mathrm{A} + \mathrm{B}^- \rightarrow \mathrm{A} + \mathrm{B} + \mathrm{e}^-, \tag{1.2}$$

charge transfer (CT)

$$\mathrm{A} + \mathrm{B}^- \rightarrow \mathrm{A}^- + \mathrm{B}, \tag{1.3}$$

and elastic scattering (ES)

$$\mathrm{A} + \mathrm{B}^- \rightarrow \mathrm{A} + \mathrm{B}^-. \tag{1.4}$$

Closely related to the reaction (1.1) is its reverted form, so-called dissociative attachment

$$\mathrm{AB} + \mathrm{e}^- \rightarrow \mathrm{A} + \mathrm{B}^-. \tag{1.5}$$

Investigation of negative ion atom collisions, from theoretical and experimental point of view has much in common with investigation of electron molecule collisions, but we will not discuss this subject here. For details about this topic we refer to recent book by Čárský and Čurík [1] and references therein.

Among the reactions introduced above, perhaps the most interesting one is the associative detachment (1.1). Its vital role in creation of free electrons in lower ionosphere by reaction of negative oxygen ion with atomic or molecular oxygen was deduced from measurement of low-frequency radio measurement by Doherty [2]. The same process, as well as reaction of molecular and atomic oxygen with O_2^-, was measured directly using flowing afterglow technique by the Fehsenfeld et al. [3, 4].

Gordillo-Vazquez and Luque [5] lately pointed out that the same associative detachment may play significant role in the conductivity of atmosphere in presence of sprites. In 2012 the same authors tried to explain the delayed sprites by associative detachment of oxygen anions [6], but Neubert et al. [7] suggested that only long-lasting space charge structures are affected by the associative detachment, and this process cannot directly explain the delays of sprites. These reactions are also of some significance in other atmospheres. For example models of Titan atmosphere introduced by Vuittona et al. [8] attribute them to the measured loss of negative ions in the atmosphere.

The role of AD in interstellar medium was discussed by Black et al. [9], who suggested that there should be evidence of associative detachment (of hydrogen

and its anion) in the spectra of planetary nebulae. However, direct verification was experimentally inaccessible at that time. But it is one of the crucial sources of hydrogen molecules in plasma with temperatures of few thousands of Kelvins. This is used also by Jenkins et al. [10].

The associative detachment for hydrogen colliding with carbon chain anions was studied by Barchholtz et al. [11]. Eichelberher et al. [12] studied associative detachment with the same (hydrogenised) carbon chains, but with hydrogen, nitrogen and oxygen. These reaction could be the starting point for creation of more complex organic compounds in interstellar environments. These were motivated by discovery of such a chains in these environments. Snow et al. [13] and Yang et al. [14, 15] continued with measurement of reaction rates for more complex organic anions with hydrogen as it is important for the ionic reactions in the interstellar medium.

Perhaps the most important role of associative detachment in astrophysics is its significance for creation of hydrogen molecules and their isotopes in environment with electron abundance. These are of a great importance for models of the early universe. Molecules are important coolants as they have finer spectrum than atoms and so they can cool the gas to much lower temperatures and allow it to compress and create protogalxies and the first stars. The most important molecules are H_2. HD is also important (but it is created usually from H_2 molecule) as it has finer vibrational structure than lighter H_2 and can thus cool the gas to even lower temperatures. The D_2 is even better in this aspect but the small abundance of the deuterium isotope makes its creation nearly impossible. The astrophysical models of these processes depend greatly on the accurate associative detachment rates of creation of hydrogen molecules. The studies of such a models ([16, 17] and reference therein) led to the need of more precise calculations as well as experimental measurements in the energy region of few eV and lower.

The primordial chemistry depends on the rotation-vibrational distribution of the final products of associative detachment of $H + H^-$ collision as it is not in local thermal equilibrium as was showed by Coppola et al. [18].

We already mentioned some experimental works. Let us now add few more, that are of interest, as they measured directly the processes in which we are interested in, or measured aspects of system that are interesting for us. Considering the details of the associative detachment dynamics, one of the most interesting experiments was done by Zwier et al. [19] who measured associative detachment for $H + Cl^-$. The authors were able to determine information about vibrational state of the HCl molecule by means of infra-red chemiluminescence. The same technique was later used for the associative detachment of $H + F^-$ by Zwier et al. [20] and to study isotopic effect for this species (collision of $D + F^-$) by Smith and Leone [21]. The next experiment that provided insight into the structure of the products of associative detachment appeared much later. In 2002, Živanov et al. [22] studied the electron spectrum for reactions of hydrogen with anions of halides. In the last year Jusko et al.[23] also build experimental set-up for measurement of electron spectrum of associative detachment. They tested this set-up for reaction of oxygen anion with molecular hydrogen, deuterium and carbon monoxide. There was also experiment with ultracold atoms of rubidium and

hydroxide anion by Deiglmayr et al. [24].

The most important for this work are the measurements of associative detachment in H + H^- collision. First measurement of this reaction was done by Schmeltekopf et al. [25] in 1967. They measured reaction rate at 300 K in flowing afterglow-selected ion flow tube experiment. The similar experiment was repeated in 2009 by Martinez et al.[26]. They found reaction rate at 300K only slightly higher ($2 \pm 0.6 \times 10^{-}9$ cm^3 $s^{-}1$) than in the original work [25]. This is nearly two times smaller than the result of Čížek et al. [27]. But at the same time merged-beam experiment by Bruhns et al. [28] shows agreement with Čížek's result and pointed out that the previously mentioned experiment may suffer from an error in calibration by reaction $Cl^- + H \rightarrow HCl + e^-$. These discrepancies stimulated the interest of other experimentalists: in 2012 Gerlich et al. [29] published thermal rates of this reaction for low temperatures that also agree with calculations [27].

We will now give a short outline of theoretical works that are interesting for us. We will mainly focus on works involving H + H^- collisions. Let us start with associative detachment (1.1).

The first theoretical works about associative detachment appeared in the end of the sixties of the last century. The cornerstone for these calculations was set by Chen [30] in 1967. He employs the projection formalism of Feshbach [31] to define the local complex potential approximation applied on atom-anion collision. In the same year Herzenberg [32] published his own version and used WKB approximation to calculate H-H^- associative detachment process for both gerade and ungerade symmetries. Simultaneously Dalgarno and Browne [33] published short paper with reaction rates calculated using WKB approximations and modified theory of radiative associations. One year later Chen and Peacher [34] used semiempirical methods to determine hydrogen-hydrogen ion potential curves and they [35] used WKB approximation and very accurate potential curves for neutral hydrogen molecules by Kołos and Wolnicwicz [36] to determine cross sections. In 1969 Mizuno and Chan [37] published their calculation for this reaction. They also used local complex potential and integrate the coupled Schrödinger equations to find the phase shifts. They compared different complex potentials, previous calculations, and they studied charge transfer and isotopic effect and showed differential cross sections as well.

The next interesting calculation appeared ten years later, when Bieniek and Dalgarno [38] calculated cross sections of AD to specific rotation-vibrational states of created hydrogen molecule. They used the same local potentials as previous calculation and used the full quantum description. The next year Bieniek [39] shows that the local complex potential approximation has problems with curve-crossing processes. He calculated the cross section to different states from T-matrix and compared the sum with the lost of flux from complex phase shift and found that they do not match.

This problem does not appear in the non-local treatment developed by Domcke ([40] and references therein) for the electron molecule collisions. This method was not used for the associative detachment at first but Domcke and collaborators [41, 42] calculated parameters needed to understand e^- + H_2 and H + H^- channels in ungerade symmetry. Meanwhile Senekowitsch et al. [43] calculated accurate adiabatic potential for ground state of H_2^-, that was used by Sakimoto

[44], who calculated cross section for very low energies and by Launay et al. [45]. Both used the local complex potentials. Using the theory developed by Domcke, Čížek et al.[27] have done fully non-local calculation for the H + H^- associative detachment in ungerade symmetry. They used the angular momentum treatment developed by Bieniek [46] for the Penning ionization. This work also includes the electronic spectra for outgoing electrons. In the next years they used this method (non-local resonance model) for calculations of associative detachment in hydrogen colliding with halide anion and compare it with the experimental data (Čížek et al.[47] and Živanov et al.[22, 48]).

Another interesting reaction is the charge transfer (1.3). Older theoretical works suggest, that this reaction strongly depends on potential energy curves of $^2\Sigma_g^+$ and $^2\Sigma_u^+$ states. All theoretical works that we are aware of are few decades old, usually calculated the charge transfer for energy region of no less than 10 eV. Early works were done by Dalgarno and McDowell[49] and Bardsley [50], who used the perturbated stationary state method. Later there were more general papers about the charge transfer by Sinha and Bardsley [51], where the WKB approximation was used and by Davidović and Janev [52], who used adiabatic approximaton. All of them calculated the cross sections or reaction rates for energies higher than few tens eV and they used different ways to treat electronic potentials. Chibisov and Janev [53] wrote the summary about the charge transfer in atom ion collisions in 1988. The experiment by Huels et al. [54] provided the last experimental results that probed the energy region from 7 eV higher.

Calculations of Čížek [27] predicted much larger associative detachment cross sections than their predecessors. This attracted the interest of experimentalist ([17], [29]) and the new data confirmed the accuracy of this calculation.

The main purpose of this work is to extend the non-local calculations for H + H^- to include the excited $^2\Sigma_g^+$ state of H + H^- in addition to the $^2\Sigma_u^+$ ground state. For this we will formulate the theoretical description to contain more discrete states and also more continua. We need to generalize the numerical codes to deal with more complex models and we construct these models and we estimate their reliability. We will also extend the calculation of associative detachment due to $^2\Sigma_u^+$ state to higher energies. In this higher energy region new channel opens – the collision detachment (1.2). The new model, that includes both gerade and ungerade states allows us to study the charge transfer as well as the elastic scattering.

Furthermore we will study isotopic effect in greater detail and we will present the comparison with experimental data, some of which is already published [55, 56] together with our theoretical data. These two papers are included in the appendix B. The appendix A also contains the description of the data collection on the attached DVD.

2. Theoretical framework

In this chapter we summarize the theoretical background of this work. As mentioned in the introduction, the same theory describes also the scattering of electron on neutral molecule [1, 40]. Here we focus on systems with more than two channels. To our knowledge, this has not been done before in the scope of non-local resonance method.

We start this chapter with section about fixed nuclei problem where we describe the parametrization of the electron Hamiltonian. This parametrization is then used in the next section to introduce nuclear dynamics, the partial-wave expansion of which is also discussed. Finally, we conclude this chapter with a few remarks on calculation of the cross sections. Atomic units ($m_e = \hbar = e_0 = 1$) are used throughout this work, unless said otherwise.

2.1 Fixed nuclei

Let us assume a problem of two neutral atoms with fixed nuclei and one additional electron. Neglecting the relativistic corrections, the Hamiltonian reads

$$H_{el} = -\sum_i \frac{|\mathbf{p}_i|^2}{2} + \sum_{i<j} \frac{1}{|\mathbf{r}_i - \mathbf{r}_j|} - \sum_i \frac{N_1}{|\mathbf{R}_1 - \mathbf{r}_i|} - \sum_i \frac{N_2}{|\mathbf{R}_2 - \mathbf{r}_i|}, \tag{2.1}$$

where $\mathbf{r}_i$ is position of ith electron, $\mathbf{p}_i$ its momentum, and $\mathbf{R}_i$ is positions of nucleus with charge N_i. We can simplify this by changing bases so that

$$\mathbf{R}_1 = -\mathbf{R_2} = \frac{R}{2}\mathbf{e}_z, \tag{2.2}$$

where R is the inter-nuclear distance and $\mathbf{e}_z$ is unitary vector in direction of the z axis. For future reference, it is useful to split this Hamiltonian into three parts, namely the kinetic energy of one of the electrons (say, $i = 1$) $T = \frac{|\mathbf{p}_1|^2}{2}$, the interaction potential of the rest of the system with this electron H_{el-M} that contains all potential terms with $i = 1$ and the rest that we will call H_M as it is the electronic Hamiltonian of the neutral molecule. Now we can define $K = T + H_M$ and write

$$H_{el} = T + H_M + H_{el-M} = K + H_{el-M}. \tag{2.3}$$

Finding eigenstates and eigenvalues of this problem is non-trivial and can be solved by using methods of quantum chemistry. This will give us independent eigenvalues and eigenfunctions for every R. An example can be seen in figure 2.1 where we show eigenvalues of system H_2^-. We shown explicitly the spectrum for H_{el} for $R = 2\,\text{au}$, where there are no discrete electronic states, first electronic continuum starts at $E \simeq -0.14\,\text{au}$ and the second continuum at energy $E \simeq 0.1\,\text{au}$. The lower continuum describes $e^- + H_2(X^1\Sigma_g^+)$, i.e. electron plus hydrogen molecule ground state, and the upper is $e^- + H_2(X^3\Sigma_u^+)$, i.e. electron and hydrogen molecule in the first excited state. For larger inter-nuclear separation the bound state $H_2^-(X^1\Sigma_u^+)$ appears (around $R = 3\,\text{au}$). In figure 2.1 we explicitly show this for $R = 4\,\text{au}$, where we have discrete state for $E \simeq -0.05\,\text{au}$

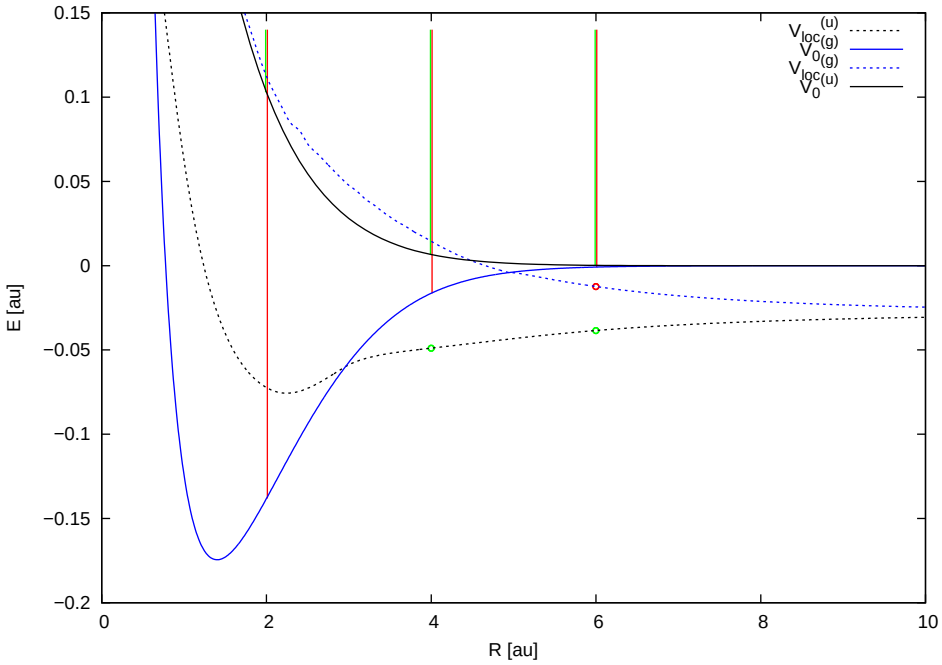

Figure 2.1: Dependence of spectrum of electronic Hamiltonian H_{el} on separation of nuclei R shown on example of H_2^-. Spectrum is explicitly shown for inter-nuclear distances $R = 2, 4, 6$ au. The circles indicate discrete spectrum of the Hamiltonian with all electrons bound. Straight lines show the one electron continuum. Gerade and ungerade symmetry of bound state wave-function is indicated by red and green colour respectively.

and similar continua as for previous case opens successively for energies around -0.016 and 0.007 au. The second bound state $H_2^-(X^1\Sigma_g^+)$ will appear around $R = 5$ au. The last explicitly shown spectrum of the Hamiltonian is at $R = 6$ au. The ungerade state lies around $E \simeq -0.038$ au; energy for gerade bound state is $E \simeq -0.012$ au; both continua opens at nearly the same energy $E \simeq 0$ au. The colour of lines and circles indicate the symmetry of bound state wave-function. The green denotes the ungerade states and the red denotes the gerade ones. It is a custom to use such eigenvalues to describe the dynamics of the system in Born-Oppenheimer approximation. This approximation assumes that the eigenstates of the above problem depends weakly on the inter-nuclear distance, therefore we can neglect their derivatives. Here we face the problem of crossing of the bound states into continuum. The non-local complex approximation solves this problem by introducing so called discrete states and modifying the continuum. The discrete states $|\phi_d^i\rangle$ (index i distinguishes between the states) are chosen to have slow dependence on inter-nuclear distance and are smooth function of R. They can be to a certain degree chosen arbitrary, i.e. we demand that for large inter-nuclear distances it correspond with bound states of electronic Hamiltonian. We further assume that these discrete states are orthogonal on each other and that they form subspace in Hilbert space of our problem corresponding to projection operator Q. The rest of the Hilbert space will then represent a subspace of orthogonalized continuum states $|\phi_k\rangle$. We will assign projection operator P to this subspace. This mean that

$$\begin{aligned} P+Q &= 1, \\ PQ = QP &= 0, \end{aligned} \tag{2.4}$$

$$\begin{aligned} Q &= \sum_i |\phi_d^i\rangle\langle\phi_d^i|, \\ P &= \sum_\alpha \int_{\mathbf{k}} \mathrm{d}\mathbf{k} |\phi_{\mathbf{k}}^\alpha\rangle\langle\phi_{\mathbf{k}}^\alpha|, \end{aligned} \tag{2.5}$$

where $\mathbf{k}$ indicate momentum vector of electron in continuum and α denotes state of the neutral molecule. The pair $(\alpha, \mathbf{k})$ describes state of complex $\mathrm{M}^*(\alpha) + \mathrm{e}^-(\mathbf{k})$. We assume that

$$\langle\phi_d^i|\phi_d^j\rangle = \delta_{ij}, \tag{2.6}$$

$$\langle\phi_{\mathbf{k}}^\alpha|\phi_{\mathbf{k}'}^{\alpha'}\rangle = \delta(\mathbf{k}-\mathbf{k}')\delta_{\alpha\alpha'}, \tag{2.7}$$

$$\langle\phi_d^i|\phi_{\mathbf{k}}^\alpha\rangle = 0. \tag{2.8}$$

To define the states $|\phi_{\mathbf{k}}^\alpha\rangle$ fulfilling these conditions we would like to describe scattering problem in our model. Following Domcke [40] we write the Hamiltonian as

$$H_{el} = K + (H_{el}^P - K) + (H_{el} - H_{el}^P), \tag{2.9}$$

where superscript P stands for projection to orthogonalized continuum, i.e. $X^P = PXP$. The initial sates is eigenstate $|\mathbf{k}^\alpha\rangle$ of Hamiltonian K containing state α of diatomic molecule and free electron with momentum k with energy $E = k^2/2 + V_0^{(\alpha)}(R)$ where $V_0^{(\alpha)}(R)$ is energy of state α of Hamiltonian H_M parametricly dependent on R. We write the Lippmann-Schwinger equations for interaction potentials in bracket above

$$|\phi_{\mathbf{k}}^{\alpha(\pm)}\rangle = |\mathbf{k}^\alpha\rangle + G_0^{(\pm)}(E)(H_{el}^P - K)|\phi_{\mathbf{k}}^{\alpha(\pm)}\rangle, \tag{2.10}$$

$$|\psi_{\mathbf{k}}^{\alpha(\pm)}\rangle = |\phi_{\mathbf{k}}^{\alpha(\pm)}\rangle + G_{bg}^{(\pm)}(E)(H_{el} - H_{el}^P)|\psi_{\mathbf{k}}^{\alpha(\pm)}\rangle, \tag{2.11}$$

where $G_0^{(\pm)}(E)$ and $G_{bg}^{(\pm)}(E)$ are Green functions corresponding to K and H_{el}^P and $E = k^2/2 + V_0^{(\alpha)}(R)$. From the Lippmann-Schwinger equation (2.10) it is clear that $|\phi_{\mathbf{k}}^{\alpha(\pm)}\rangle$ is eigenvector of H_{el}^P and so $Q|\phi_{\mathbf{k}}^{(\pm)}\rangle = 0$. The two sets of vectors $|\phi_{\mathbf{k}}^{\alpha(+)}\rangle$ or $|\phi_{\mathbf{k}}^{\alpha(-)}\rangle$ can be used in equation (2.5) to expand the projection operator P, assuming that the total energy is low enough not to involve two electrons in continuum. Thus the states not included are energetically high enough, that the investigated processes do not depend on them.

Let us define the discrete state potential V_d^{ij} and coupling $V_{d\mathbf{k}}^{i\alpha}$ matrices as

$$V_d^{ij} = \langle\phi_d^i|H_{el}|\phi_d^j\rangle, \tag{2.12}$$

$$V_{d\mathbf{k}}^{i\alpha} = \langle\phi_d^i|H_{el}|\phi_{\mathbf{k}}^{\alpha(+)}\rangle. \tag{2.13}$$

The construction of $|\phi_{\mathbf{k}}^{\alpha(+)}\rangle$ guarantees that

$$V_{\mathbf{k}\mathbf{k}'}^{\alpha\alpha'} = \langle\phi_{\mathbf{k}}^{\alpha(+)}|H_{el}|\phi_{\mathbf{k}'}^{\alpha'(+)}\rangle = \delta_{\alpha\alpha'}\delta(\mathbf{k}-\mathbf{k}')\left[V_0^{(\alpha)}(R) + \frac{1}{2}k^2\right]. \tag{2.14}$$

knowing these function we parametrize H_{el} as

$$H_{el} = \sum_{ij} |\phi_d^i\rangle V_d^{ij} \langle \phi_d^j| + \sum_{\alpha} \int \mathrm{d}\mathbf{k} |\phi_{\mathbf{k}}^{\alpha(+)}\rangle \left[\frac{\mathbf{k}^2}{2} + V_0^{(\alpha)}\right] \langle \phi_{\mathbf{k}}^{\alpha(+)}| + \\ + \sum_{i\alpha} \int \mathrm{d}\mathbf{k} \left[|\phi_d^i\rangle V_{d\mathbf{k}}^{i\alpha} \langle \phi_{\mathbf{k}}^{\alpha(+)}| + \text{c. c.}\right], \tag{2.15}$$

which will be used in dynamics of nuclear motion.

We can use the two potential formula for T-matrix to get the separation of T-matrix to background and resonance terms. This is useful to solve the fixed nuclei scattering of electron and molecule and we can use data from such scattering to construct functions V_d, V_{dk} from fixed nuclei data. It is

$$T(\mathbf{k}', \mathbf{k}) = T_{bg} + T_{res}, \tag{2.16}$$

$$T_{bg} = \langle \mathbf{k}' | H_{el}^P - K | \phi_{\mathbf{k}}^{(+)} \rangle, \tag{2.17}$$

$$T_{res} = \langle \phi_{\mathbf{k}'}^{(-)} | H_{el} - H_{el}^P | \psi_{\mathbf{k}}^{(+)} \rangle. \tag{2.18}$$

The equation (2.11) can formally be solved and express resonant T-matrix in terms of $|\phi_{\mathbf{k}}^{(\pm)}\rangle$. We start by applying projection operator P and Q on the equation

$$P|\psi_{\mathbf{k}}^{(\pm)}\rangle = |\phi_{\mathbf{k}}^{(\pm)}\rangle + PG_{bg}^{(\pm)} P H_{el} Q |\psi_{\mathbf{k}}^{(\pm)}\rangle, \tag{2.19}$$

$$Q|\psi_{\mathbf{k}}^{(\pm)}\rangle = \frac{1}{E \pm i\epsilon} (QH_{el}Q + QH_{el}P)|\psi_{\mathbf{k}}^{(\pm)}\rangle, \tag{2.20}$$

We use first equation to eliminate $P|\psi_{\mathbf{k}}^{(\pm)}\rangle$ which leads to

$$Q|\psi_{\mathbf{k}}^{(\pm)}\rangle = \left[E - QH_{el}Q - QH_{el}PG_{bg}^{(\pm)}(E)PH_{el}Q \pm i\epsilon\right]^{-1} QH_{el}P|\phi_{\mathbf{k}}^{(\pm)}\rangle. \tag{2.21}$$

We can use this to calculate resonant T-matrix:

$$T_{res} = \langle \phi_{\mathbf{k}'}^{(-)} | PH_{el}Q \frac{1}{E - QH_{el}Q - QH_{el}PG_{bg}^{(\pm)}(E)PH_{el}Q \pm i\epsilon} QH_{el}P|\phi_{\mathbf{k}}^{(+)}\rangle. \tag{2.22}$$

QHQ is expressed in terms of V_d^{ij}, PHQ and QHP in terms of discrete-state-continuum coupling $V_{d\mathbf{k}}^{i\alpha}$ and we define level shift operator

$$F_{ij}(E) = \langle \phi_d^i | H_{el} P G_{bg}^{(\pm)}(E) P H_{el} | \phi_d^j \rangle = \sum_{\alpha} \Delta_{ij}^{(\alpha)}(E) - \frac{i}{2}\Gamma_{ij}^{(\alpha)}(E). \tag{2.23}$$

Using the fact that states $|\phi_{\mathbf{k}}^{\alpha}\rangle$ diagonalize operator G_{bg} we can use $V_{d_i\mathbf{k}}$ to express level shift using well known formula $(x + i\epsilon)^{-1} = \text{v.p.}\frac{1}{x} - i\pi\delta(x)$:

$$\Gamma_{ij}^{(\alpha)}(E) = 2\pi \int \mathrm{d}\hat{\mathbf{k}} V_{d\mathbf{k}}^{i\alpha *} V_{d\mathbf{k}}^{j\alpha}, \tag{2.24}$$

$$\Delta_{ij}^{(\alpha)}(E) = \frac{1}{2\pi} \text{v.p.} \int \mathrm{d}E' \frac{\Gamma_{ij}^{(\alpha)}(E')}{E - V_0^{(\alpha)} - E'}. \tag{2.25}$$

So the $V_0^{(\alpha)}$, V_d^{ij} and $V_{d\mathbf{k}}^{i\alpha}$ fully describe the resonant scattering,

$$T_{res}^{\alpha\alpha'}(\mathbf{k}', \mathbf{k}) = \sum_{ij} V_{d\mathbf{k}'}^{i\alpha'*} \left[E - V_d - F(E)\right]_{ij} V_{d\mathbf{k}}^{j\alpha}. \tag{2.26}$$

We have shown how to decompose our scattering problem into two parts – background, which is usually small, and resonant which is usually the dominant part. The choice of Q operator and $|\phi_d^i\rangle$ is the non-trivial part here. A few methods were developed to find states that could be used as discrete states. For our problem, the stabilisation methods for finding resonances in continuum is important. Other possibility is to use state that will slowly change with inter-nuclear distance – based on physical intuition for example fixed state centred around one of the atoms.

In the next sections we will mostly use models with only one discrete state, so we will drop indexes i and j. This covers simple cases of different diatomic molecules like HF, HCl, and HBr [47, 57] as well as molecules consisting of the same or similar atoms like H_2, D_2, and HD. In the case of first molecules, the situation is simple since the electronic states are separated with large gap. The latter case is more interesting – electronic problem has two degenerate sates for large R due to inversion symmetry with respect to the centre between the two nuclei. But thanks to the same symmetry we can decompose Hilbert space into two (gerade and ungerade) sub-spaces and solve each problem separately. We will discuss this symmetry later. Similarly, for clarity's sake, we will drop index α for indexing continuum, but we will return to it later.

2.2 Nuclear dynamics

Let us introduce nuclear dynamics using the separation that we have introduced above. To do this we assume, that the wave function of our problem has the form

$$|\Psi\rangle = |\Phi_d\rangle|\phi_d\rangle + \sum_{\mathbf{k}} |\Phi_{\mathbf{k}}\rangle|\phi_{\mathbf{k}}\rangle, \tag{2.27}$$

where $|\Phi\rangle$ are states in nuclear Hilbert space and $|\phi\rangle$ are the once in electronic space introduced in the previous section. This is the same idea as in Born-Oppenheimer approximation, but instead of using eigenstates of the electron Hamiltonian, we are using discrete states and orthogonalized continuum. If we choose these correctly, they will change slowly with change of the inter-nuclear distance, and Born-Oppenheimer-like approximation will be valid, i.e. we will neglect derivatives with respect to inter-nuclear distance of electronic wave functions.

We can extend projection operators P and Q to Hilbert space of whole problem as

$$P = \int \mathrm{d}\mathbf{R} P_{el} |\mathbf{R}\rangle\langle\mathbf{R}|, \tag{2.28}$$

$$Q = \int \mathrm{d}\mathbf{R} Q_{el} |\mathbf{R}\rangle\langle\mathbf{R}|, \tag{2.29}$$

$$\tag{2.30}$$

where the P_{el} and Q_{el} are the projectors defined by (2.4 and 2.5) for each R. We will assume, that all negative ion bound states (large nuclear separation) are contained in subspace defined by projector Q – so this includes channels like A + B^- at lare internuclear distances. The P space contains channels with bound molecule and electron e^- + AB(α) and dissociated channels e^- + A + B.

Full Hamiltonian reads $H = T_N + H_{el}$, where T_N is kinetic energy operator of nuclei and (2.15) can be used for H_{el}. We will indicate projections with superscripts: $A^{UV} = UAV$; $U, V \in \{P, Q\}$ and we will omit one, if they are duplicate. We will use $H_0 = T_N + H_{el}^P + H_{el}^Q$ as "unperturbed" Hamiltonian. This includes interaction for channels of initial and final asymptotic states in Born-Oppenheimer approximation – neutral with ion A+B^-, electron with molecule e^- + AB(ν) including vibrational and rotational excitation ν and electron with dissociated molecule e^- + A + B. The non-local coupling between the resonance and background sub-spaces $H_I = H_{el}^{PQ} + H_{el}^{QP}$ will be our interaction Hamiltonian. The Lippmann-Schwinger equation for scattering wave function is then

$$|\Psi^{(+)}\rangle = |\Psi_0^{(+)}\rangle + G_0^{(+)} H_I |\Psi^{(+)}\rangle, \tag{2.31}$$

where $|\Psi_0^{(+)}\rangle$ is eigenstate of H_0 with incoming boundary condition.

The choice of separation of Hilbert space by P and Q projectors for which we can neglect the non-diagonal elements of operator T_N applied on $|\phi_{d_i}\rangle$ and $|\phi_{\mathbf{k}}\rangle$ leads to

$$[T_N, P] = [T_N, Q] = 0, \tag{2.32}$$

and Green's function $G_0^{(+)}$ can then be written as

$$G_0^{(+)} = [E - H_0 + i\epsilon]^{-1} = P[E - H_0 + i\epsilon]^{-1} P + Q[E - H_0 + i\epsilon]^{-1} Q = G_0^{P(+)} + G_0^{Q(+)}. \tag{2.33}$$

Now we will use projection operators P and Q on this equation 2.31, and eliminate $P|\Psi^{(\pm)}\rangle$ in the same way as in fixed nuclei case. We will get:

$$Q|\Psi^{(\pm)}\rangle = Q|\Psi_0\rangle + G_0^Q H^{QP}|\Psi_0\rangle + G_0^Q H^{QP} G_0^P H^{PQ}|\Psi^{(\pm)}\rangle. \tag{2.34}$$

This way we reduced the problem to a small subspace Q of the Hilbert space. Equation (2.34) will be basis of numerical method to solve dynamics, but before going into details we will like to give some interpretation of term $H^{QP}G_0^P H^{PQ}$. If we multiply equation (2.34) with inverse Green's function

$$\left[G_0^Q\right]^{-1} = Q\left[E - H_0^Q + i\epsilon\right]Q, \tag{2.35}$$

we will come to inhomogeneous Schrödinger equation with effective Hamiltonian

$$H_{eff} = H^Q + H^{QP}G_0^P H^{PQ} \tag{2.36}$$

and right hand side $H^{QP}|\Psi\rangle$. We can use this and expansion of H_{el} (2.15) to express effective Hamiltonian as

$$H_{eff} = T_N + V_d + F(E) \tag{2.37}$$

where V_d is Born-Oppenheimer potential for discrete state (or potential matrix, if there are more discrete states), and

$$F(E) = \int \mathrm{d}\mathbf{k} V_{d\mathbf{k}}^* \left[E - T_N - V_0 - k^2/2 + i\epsilon\right]^{-1} V_{d\mathbf{k}}, \tag{2.38}$$

is the non-local energy-dependent part of effective potential produced by interaction with channels in P subspace.

We will be mostly interested in associative and collision detachment. Let us express T-matrix for this reaction. The initial state A + B$^-$ (for Hamiltonian H_0) belongs in resonant subspace and assuming that resonant subspace contain only one state we have $|\Psi_0^{(+)}\rangle = |\phi_d\rangle|\bar{\Phi}_d^{(+)}\rangle$. Here super-index (+) indicate incoming boundary condition (the same can be done with outgoing boundary condition – we will indicate it by super-index (−)). States $|\Psi_0^{(+)}\rangle$ as well as $|\bar{\Phi}_d^{(+)}\rangle$ satisfy Schrödinger equations

$$\left[T_N + V_d\right]|\bar{\Phi}_d^{(+)}\rangle = E|\bar{\Phi}_d^{(+)}\rangle, \tag{2.39}$$

$$H_0|\Psi_0^{(+)}\rangle = E|\Psi_0^{(+)}\rangle. \tag{2.40}$$

To solve equation (2.34) we also need $Q|\Psi^{(+)}\rangle = |\phi_d\rangle|\Phi_d^{(+)}\rangle$.This leads to the Lippmann-Schwinger equation:

$$|\Phi_d^{(+)}\rangle = |\bar{\Phi}_d^{(+)}\rangle + G_d^{(+)}(E)F^{(+)}(E)|\Phi_d^{(+)}\rangle, \tag{2.41}$$

where Green's function $G_d^{(\pm)(E)} = (E - T_N - V_d \pm i\epsilon)^{-1}$. And we can express T-matrix of detachment processes as

$$T_D = \langle\Psi_f^{(-)}|H^{PQ}|\Psi^{(+)}\rangle = \langle\nu_f|V_{d\mathbf{k}_f}^*|\Phi_d^{(+)}\rangle, \tag{2.42}$$

where $|\Psi_f^{(-)}\rangle = |\phi_{\mathbf{k}}^{(-)}\rangle|\nu_f\rangle$ is the final state of neutral molecule (or two atoms) plus outgoing electron with momentum $\mathbf{k}$. We will be more specific about vibrational states of neutral molecule $|\nu_f\rangle$ in the next subsection. This is bound by energy conservation law. If E_i denotes centre of mass kinetic energy of incoming molecule and ion and E_a electron affinity (i.e. bounding energy of electron in anion), and E_f is energy of bound state $|\nu_f\rangle$ then $E_i - E_a = E_f + k^2/2$.

2.2.1 Partial wave expansion

Now we introduce partial wave expansion (for details [46, 58]) which will effectively transform this three-dimensional problem to system of one-dimensional ones, that is more suitable for numeric calculations. We assume that all electronic state are of Σ-symmetry. This is true for all electronic states of neutral and discrete states of anions for diatomic molecules considered in this work. Fixed nuclei scattering problem is symmetrical along inter-nuclear axis z and so Hamiltonian commutes with projection operator of angular momentum to this axis L_z. First we will expand electronic wave functions and coupling $V_{d\mathbf{k}}$:

$$|\phi_{\mathbf{k}}\rangle = \sum_{km} Y^*_{lm}(\hat{k})|\phi_{klm}\rangle, \tag{2.43}$$

where $k = |\mathbf{k}|$ and $\hat{k} = \mathbf{k}/k$. Now we use definition (2.13) of coupling and the fact that discrete state has Σ-symmetry.

$$V_{d\mathbf{k}} = \sum_{l} Y^*_{l0}(\hat{k})V_{dk_l} \tag{2.44}$$

and

$$V_{dk_l} = \langle\phi_d|H_{el}|\phi_{klm}\rangle. \tag{2.45}$$

This is still done in coordinate system where both nuclei lie on axis z. Now we transform V_{dk} to coordinate system fixed in space and located in centre of mass. Let $\mathbf{R}$ denote relative position of the two nuclei, $R = \|\mathbf{R}\|$, and $\hat{R} = \mathbf{R}/R$. Than we can use the expansion

$$V_{d\mathbf{k}}(\mathbf{R}) = \sum_{lm} \sqrt{\frac{4\pi}{2l+1}} Y^*_{lm}(\hat{k})Y_{lm}(\hat{R})V_{dk_l}(R). \tag{2.46}$$

Next we want to expand the non-local part F of the effective Hamiltonian. Fist we need expansion of the Green's function $[E - T_N - V_0 + i\epsilon]^{-1}$. We know that the potential V_0 is spherically symmetric and the Green's function is thus diagonal in angular momentum representation

$$\langle\mathbf{R}|[E - T_N - V_0 + i\epsilon]^{-1}|\mathbf{R}'\rangle = \sum_{lm} Y_{lm}(\hat{R})\frac{1}{R}G_{0l}(E, R, R')\frac{1}{R'}Y^*_{lm}(\hat{R}'). \tag{2.47}$$

Now we substitute this expansion and the expansion of the coupling (2.46) into (2.38) and we find partial wave expansion:

$$\begin{aligned}\int \mathrm{d}\hat{R}\mathrm{d}\hat{R}' Y^*_{JM}(\hat{R})Y_{J'M'}(\hat{R}')F(E, \mathbf{R}, \mathbf{R}') = \int \mathrm{d}\mathbf{k}\mathrm{d}\hat{R}\mathrm{d}\hat{R}' \sum_{l_2 l_2 m_1 m_2 L_0 M_0} \\ Y^*_{JM}(\hat{R})Y_{J'M'}(\hat{R}')\sqrt{\frac{4\pi}{2l_1+1}}Y_{l_1m_1}(\hat{k})Y^*_{l_1m_1}(\hat{R})V^*_{dk_{l_1}}(R) \\ Y_{L_0M_0}(\hat{R})\frac{1}{R}G_{0l}(E - k^2/2, R, R')\frac{1}{R'}Y^*_{L_0M_0}(\hat{R}') \\ \sqrt{\frac{4\pi}{2l_2+1}}Y^*_{l_2m_2}(\hat{k})Y_{l_2m_2}(\hat{R}')V_{dk_{l_2}}(R').\end{aligned} \tag{2.48}$$

We can use known properties of spherical harmonics and perform integration over all angular variables; integration over $\hat{k}$ reveals $\delta_{l_1 l_2}$and $\delta_{m_1 m_2}$ and integration over spacial variables leads to Wigner 3-j symbols. This can be further simplified using their orthogonality to get:

$$\int \mathrm{d}\hat{R}\mathrm{d}\hat{R}' Y^*_{JM}(\hat{R}) Y_{J'M'}(\hat{R}') F(E, \mathbf{R}, \mathbf{R}') = \frac{1}{RR'}\delta_{JJ'}\delta_{MM'} f_J(E, R, R') \tag{2.49}$$

where

$$\begin{aligned} f_J = \sum_l f_{J;l} = \sum_{l,J'} (2J'+1) \begin{pmatrix} l & J' & J \\ 0 & 0 & 0 \end{pmatrix} \\ \int \mathrm{d}E' V_{dk'l}(R) G_{0J'} \left(E - k'^2/2, R, R'\right) V^*_{dk'l}(R'). \end{aligned} \tag{2.50}$$

The diagonality of the non-local part of the effective Hamiltonian in angular momentum basis corresponds to its spherical symmetry, and is expected as electronic Hamiltonian as well as discrete state and coupling $V_{d\mathbf{k}}$ depends only on distance R. This means that different partial waves of $|\Phi_d\rangle$ will decouple in (2.41) and we get a set of independent equations. There is still coupling to different continuum states via different $f_{J;l}$. We will assume, that we need only a few of these couplings with small value of l. This can be usually justified by low mass of electron, meaning that centrifugal barrier $\frac{l(l+1)}{2r^2}$ is strong enough that coupling will be negligible for collisions of energy of our interest.

Now we will expand the Lippmann-Schwinger equation (2.41). We start by defining the expansion of

$$\langle R|\bar{\Phi}^{\pm}_d\rangle = N \sum_{lm} i^l \frac{1}{RK} Y^*_{lm}(\hat{k}) Y_{lm}(\hat{R}) \varphi_l(R), \tag{2.51}$$

and

$$\langle R|\Phi^{\pm}_d\rangle = N \sum_{lm} i^l \frac{1}{RK} Y^*_{lm}(\hat{k}) Y_{lm}(\hat{R}) \phi_l(R). \tag{2.52}$$

Here $\mathbf{k}$ is momentum of incoming scattering wave and $N = \sqrt{2/\pi}$ is normalisation constant and $K = \sqrt{2\mu E}$ is momentum. Next we need the expansion of the Green's function G_d:

$$\langle \mathbf{R}|G^{(+)}_d|\mathbf{R}'\rangle = \sum_{lm} Y_{lm}(\hat{R}) \frac{1}{R} G_l(E, R, R') \frac{1}{R'} Y^*_{lm}(\hat{R}'). \tag{2.53}$$

And finally we write equation

$$\phi_J(R) = \varphi_J(R) + \int \mathrm{d}R'\mathrm{d}R'' G_J(E, R, R') f_J(E, R', R'') \phi_J(R''). \tag{2.54}$$

To expand the T-matrix we need to specify the final state of the neutral molecule. The rotational state of diatomic molecule can be described by quantum numbers J and m and the rotational eigenstates are spherical harmonics $Y_{lm}\hat{R}$. Vibrational states $\nu_{n_f J_f}(R)$ of molecule are then dependent on quantum number

J from rotational state of the molecule and n that counts the vibrational states. The expansion of the final states indicated by subscript f is

$$\langle R|\nu_f\rangle = \sqrt{\frac{K}{\mu}}\frac{1}{R}Y_{J_fM_f}(\hat{R})\nu_{n_fJ_f}(R). \tag{2.55}$$

We thus write T-matrix

$$\begin{aligned} T_D(\nu_f,\mathbf{K}) = \langle\nu_f|V^*_{d\mathbf{k}_f}|\Phi^{(+)}_d\rangle = \frac{N}{\sqrt{k\mu}}\sum_{lmJM}\sqrt{(2J_f+1)(2J+1)}i^J(-1)^{M_f} \\ Y_{lm}(\hat{k}_l)Y_{JM}(\hat{k})\begin{pmatrix} J_f & l & J \\ 0 & 0 & 0\end{pmatrix}\begin{pmatrix} J_f & l & J \\ -M_f & m & M\end{pmatrix}t_{Jl}\left(\nu_{n_fJ_f},k_l\right), \end{aligned} \tag{2.56}$$

where k_l is momentum of free electron with angular momentum l, and

$$t_{Jl}\left(\nu_{n_fJ_f},k_l\right) = \int \mathrm{d}R\nu_{n_fJ_f}(R)V_{dk_l}(R)\phi_J(R). \tag{2.57}$$

The differential cross section then reads

$$\frac{\mathrm{d}}{\mathrm{d}\Omega}\sigma_D(\nu_f,\mathbf{K}) = s_i\left[4\pi^2\mu\right]^2|T_D(\nu_f,\mathbf{K})|^2, \tag{2.58}$$

where s_i is statistical factor, that is coming from the model. Typically it is related to multiplicity of incoming state, usually due to symmetry of the problem.

We will be generally more interested in integral cross sections averaged over $\hat{K}$ and integrated over $\hat{k}$. Here we can use the orthogonality of Wigner's 3j-symbols and get:

$$\sigma_D(\nu_f,K) = \frac{4\pi^2}{KE}\sum_{Jl}s_i(2J+1)\begin{pmatrix} J_f & l & J \\ 0 & 0 & 0\end{pmatrix}^2|t_{Jl}\left(\nu_{n_fJ_f},k_l\right)|^2. \tag{2.59}$$

Total cross section can then be obtained by summing this formula over all (energetically accessible) final states, or we can use unitary condition. We know that flux that is lost in discrete channel must contribute to detachment channel. This leads to

$$\sigma_{tot}(E) = \frac{2\mu}{KE}\sum_J s_i(2J+1)\int \mathrm{d}R\mathrm{d}R'\phi^*_J(R)[f_J(E,R,R') - f^*_J(E,R,R')]\phi_J(R'). \tag{2.60}$$

These two ways of getting total associative detachment cross section can be compared to test the numerical accuracy of our calculation. It can be showed that, using expansion of G_{0l}, the two expansions of σ_{tot} are equivalent if there is either no collision detachment, or if we also sum over the discretized continuum in equation (2.59).

2.2.2 Notes on numerical implementation

To calculate the cross section (2.59) we need to calculate the T-matrix element (2.57). To do so we will need wave function $\phi_J(R)$ as well as the bound state

of the neutral molecule $\nu_{n_f J_f}(R)$. To obtain wave function $\phi_J(R)$ we will need the non-local potential $f_{J;l}$, the Green's function G_J and the initial state wave function φ_J and solve equation (2.54).

In the first part of this section, we will explain how we obtain non-local potential $f_{J;l}$ defined by equation (2.50). We will need to find the Green's function G_{0J} (2.47) of neutral molecule and as a by-product we also find the states of the neutral molecule $\nu_{n_f J_f}(R)$. In the next part we will show how to calculate initial state $\varphi_J(R)$ (2.51) that is eigenstate of the system with potential V_d with incoming boundary condition and the expansion of the Green's function G_J for the same system defined by the equation (2.53). And finally we explain the method that we are using to solve the Lippmann-Schwinger equation (2.54).

Calculation of non-local potential

In this section we will now try to refine equation (2.50) to the form suitable for numerical calculation. We will also show how this corresponds with operator F established in (2.23). Let us look at $F(E)$ from equation (2.38) in R-representation. We get

$$F(E, \mathbf{R}, \mathbf{R}') = \Delta(E - T_N - V_0, \mathbf{R}, \mathbf{R}') - \frac{i}{2}\Gamma(E - T_N - V_0, \mathbf{R}, \mathbf{R}'), \tag{2.61}$$

where operator $T_N + V_0$ is Hamiltonian of neutral molecule that we use to define G_{0J} (2.47) and where

$$\Gamma(\bar{E}, \mathbf{R}, \mathbf{R}') = 2\pi \int \mathrm{d}\hat{\mathbf{k}} V_{d\mathbf{k}}(\mathbf{R}) V^*_{d\mathbf{k}}(\mathbf{R}'), \tag{2.62}$$

$$\Delta(\bar{E}, \mathbf{R}, \mathbf{R}') = \frac{1}{2\pi}\mathrm{v.p.} \int \mathrm{d}E' \Gamma(E', \mathbf{R}, \mathbf{R}')/(\bar{E} - E'), \tag{2.63}$$

where $\bar{E} = \mathbf{k}^2/2$. We see that for the case of $\mathbf{R} = \mathbf{R}'$ these equations coincide with fixed nuclei variant of resonant width $\Gamma(\bar{E}, \mathbf{R})$ and energy shift $\Delta(\bar{E}, \mathbf{R})$ (2.24) and(2.25).

Now we will show how we insert operator $T_N + V_0$ into the $F(E, \mathbf{R}, \mathbf{R}')$ in partial wave expansion. We focus only on one element $f_{J;l}$ and use spectral decomposition of the Green function

$$G_{0J}(E - k^2/2) = \sum\!\!\!\!\!\!\int_n \nu_{nl}(R)[E - k^2/2 - E_{nl} + i\epsilon]^{-1}\nu_{nl}(R'), \tag{2.64}$$

where E_{nl} is energy of state ν_{nl} and the n index bound as well as continuum states of neutral molecule. We insert this G_{0J} into equation (2.50) and change the order of integration and summation:

$$\begin{aligned} f_{J;l} = \sum_{J'} (2J'+1) \begin{pmatrix} l & J' & J \\ 0 & 0 & 0 \end{pmatrix} \sum\!\!\!\!\!\!\int_n \nu_{nJ'}(R)\nu_{nJ'}(R') \times \\ \times \underbrace{\int \mathrm{d}k' k'^2 V_{dk'_l}(R)(E - k^2/2' - E_{nJ'} + i\epsilon)^{-1} V_{dk'_l}(R')}_{F_l(E - E_{nJ'}, R, R')}. \end{aligned} \tag{2.65}$$

using Sokhotski formula $\frac{1}{x\pm i\epsilon} = \mp i\pi\delta(x) + \text{v.p.}(\frac{1}{x})$, F_l can be split to hermitian and antihermitian parts

$$F_l(E,R,R') = \Delta_l(E,R,R') + \frac{i}{2}\Gamma_l(E,R,R'), \tag{2.66}$$

where

$$\Gamma_l(E,R,R') = 2\pi V_{dkl}(R)V_{dkl}(R'), \tag{2.67}$$

$$\Delta_l(E,R,R') = \frac{1}{2\pi}\text{v.p.}\int \mathrm{d}E'\Gamma_l(E',R,R')/(E-E'). \tag{2.68}$$

In our calculation, we will discretise the continuous part of decomposition of G_{0J}. We are using discrete variable representation (DVR) with Fourier-sine bases [59] to calculate ν_{nJ} and E_{nJ} for H_2 molecule. This represents also natural way of discretisation of continuum states. Typically in the following sections, we use bases of few hundred of DVR states on the interval of R from 0.01 to 15 au. We confirmed that the results are stable (T-matrix 10^{-4}) with increasing the number of states as well as taking larger interval for DVR calculation. It should be mentioned, that we are expressing F_l in form

$$F_l(R,R',E) = \sum_{ij} g_i(R)h_{ij}(E)g_j(R'), \tag{2.69}$$

where we calculate $g_j(R)$ on our grid and $h_{ij}(E-E_{\nu J})$ for all included states for Hamiltonian H_0. The $g_i(R)$ and h_{ij} can be calculated by (2.67) and for special form of h_{ij} we can use the results of Domcke et al. (used in [60]; see (3.18) for details) we can express the integral in equation (2.68) as convergent series (the g_i is the same for real and imaginary part).

Local potential calculation

In this section we discuss the Lippmann-Schwinger equation for local potential V_d and how to obtain partial wave expansion of $|\bar{\Phi}_d^+\rangle$ as well as irregular solution that we will use later to construct the Green's function G_d respectively their partial expansion φ_J and G_J. The Lippmann-Schwinger equation

$$|\bar{\Phi}^{(+)}\rangle = |k\rangle + \bar{G}_0^{(+)}(E)V_d|\bar{\Phi}^{(+)}\rangle, \tag{2.70}$$

can be expanded to partial waves as the potential V_d is spherically symmetric. The $|k\rangle$ denotes state of free Hamiltonian T_N and the $\bar{G}_0^{(+)}$ is the corresponding Green's function. We use expansion (2.51) and knowledge that the eigenstates of Hamiltonian T_N are spherical Bessel functions and we expand the Green's function of the free Hamiltonian in regular and irregular solutions:

$$\varphi_J(R) = u_J(R) - \frac{2\mu}{K}\int \mathrm{d}R' u_J(R_<)v_J(R_>)V_d(R')\phi_J(R'), \tag{2.71}$$

where $R_<$ and $R_>$ are minimum and maximum of R, R' respectively. And

$$u_J(R) = RKj_J(KR), \tag{2.72}$$

$$v_J(R) = iRKh_J(KR), \tag{2.73}$$

where j_J and h_J are spherical Bessel and Hankel functions respectively. The equation 2.71 is Voltera integral equation and the method we are using was proposed by Horáček [61]. This method gives us the right(incoming) boundary conditions and compared to the direct solution of Schrödinger equation we do not need to calculated derivatives. We rewrite equation (2.71)

$$\phi_J(R) = Au_J(R) - \frac{2\mu}{K}\int_0^R \mathrm{d}R'[v_J(R)u_J(R') - u_J(R)v_J(R')]V_d(R')\phi_J(R'), \quad (2.74)$$

where

$$A = 1 - \frac{2\mu}{K}\int_0^\infty \mathrm{d}R' v_J(R)V_d(R')\phi_J(R'). \quad (2.75)$$

If we now define

$$\begin{aligned} f(R) &= \phi_J(R)/A = [1-\beta(R)]u_J(R) + \alpha(R)v_J(R), & (2.76)\\ \alpha(R) &= -\frac{2\mu}{K}\int_0^R \mathrm{d}R' u_J(R)V_d(R')f(R'), & (2.77)\\ \beta(R) &= -\frac{2\mu}{K}\int_0^R \mathrm{d}R' v_J(R)V_d(R')f(R'), & (2.78) \end{aligned}$$

and we can easily found constant $A = [1-\beta(\infty)]^{-1}$, and elastic T-matrix element is given by

$$t = -\frac{2\mu}{K}\int_0^\infty \mathrm{d}R' u_J(R)V_d(R')\phi_J(R') = \frac{\alpha(\infty)}{1-\beta(\infty)} \quad (2.79)$$

This can be calculated on a grid, because the terms in integrals on right hand side of equation (2.76) with $f(R)$ will subtract.

Next we will need the Green's function G_J. It should satisfy the Schrödinger equation

$$\left(\frac{\mathrm{d}^2}{2\mu \mathrm{d}R^2} + \frac{J(J+1)}{2\mu R^2} + V_d(R) - E\right) G_J(E,R,R') = \delta(R-R'). \quad (2.80)$$

This can be done by expressing the Green's function in terms of regular and irregular solution as

$$G_J = -\frac{2\mu}{K}\phi_{(r)J}(R_<)\phi_{(i)J}(R_>). \quad (2.81)$$

The regular solution is already calculated $\phi_{(r)J}(R) = \varphi_J(R)$. And the irregular equation should have same behaviour in infinity as $v_J(R)$ and it is easy to show that it obeys equation

$$\phi_{(i)J}(R) = v_J(R) - \frac{2\mu}{K}\int \mathrm{d}R' u_J(R_<)v_J(R_>)V_d(R')\phi_J(R'), \quad (2.82)$$

and this can be solved similarly to the previous one, we define $f(R) = \phi_{(i)J}(R)/A$, where

$$f(R) = \phi_J(R)/A = [1-\beta(R)]u_J(R) + \alpha(R)v_J(R), \quad (2.83)$$

$$\alpha(R) = -\frac{2\mu}{K}\int_R^\infty \mathrm{d}R' u_J(R)V_d(R')f(R'), \quad (2.84)$$

$$\beta(R) = -\frac{2\mu}{K}\int_R^\infty \mathrm{d}R' v_J(R)V_d(R')f(R'), \quad (2.85)$$

$$A = 1 - \frac{2\mu}{K}\int_0^\infty \mathrm{d}R' u_J(R)V_d(R')\phi_{(i)J}(R') = 1 + A\beta(0), \quad (2.86)$$

so the $A = [1-\beta(0)]^{-1}$. The method of calculation is similar to case of regular solution. The only difference is that we need to start from high R, so that condition $\phi_{(i)J}(R) = v_J(R)$ is reasonable satisfied. We are calculating this on a uniform grid for $R \in (0.01, 10)$au that has three thousand points, we will use further. But we include secondary grid from 10 to 100 au that will ensure correct inclusion of asymptotic behaviour of potential. This grid is uniform in logarithmic scale. This ensures better precision for lower energy, where it is more relevant. By increasing these parameters we estimate error in T-matrix to be less than 10^{-4}.

Lippmann-Schwinger equation with non-local potential

Finally we need to solve the Lippmann-Schwinger equation (2.54) with non-local potential. This we do using the Schwinger-Lanczos method. We will give here short review of this method, detailed description is given elsewhere [62, 59].

In the Schwinger variation principle T-matrix element

$$T_{fi} = \langle\phi_f|T|\phi_i\rangle = \langle\phi_f|V(V - VG_0V)^{-1}V|\phi_i\rangle \quad (2.87)$$

is given by stationary values of functional

$$T[\psi_-, \psi_+] = \langle\phi_f|V|\psi_+\rangle + \langle\psi_-|V|\phi_i\rangle - \langle\psi_-|V - VG_0V|\psi_+\rangle, \quad (2.88)$$

where V is interaction potential and G_0 is green function of Hamiltonian without interaction potential. The stationary value is obtained, when $|\psi_\pm\rangle$ satisfy corresponding the Lippmann-Schwinger equation. We will use decomposition of $|\psi_\pm\rangle$

$$|\psi_\pm\rangle = \sum_i c_i^\pm |g_i\rangle, \quad (2.89)$$

where $c_i^\pm$ are variational parameters, and the approximation to T-matrix elements are then

$$T_{fi}^N = \sum_{i,j=0}^N \langle\phi_f|V|g_i\rangle(M^{-1})_{ij}\langle g_j|V|\phi_i\rangle \quad (2.90)$$

where the M matrix is given as $M_{ij} = \langle g_i|V - VG_0V|g_j\rangle$ and $|g_i\rangle$ can be chosen arbitrary with condition of regularity of matrix M. The Schwinger-Lanczos method was developed for case of elastic scattering, i.e. calculation of diagonal elements of T-matrix ($|\phi\rangle = |\phi_f\rangle = |\phi\rangle_i$). We will start with $|g_1 = |\phi\rangle\langle\phi|V|\phi\rangle^{-1/2}$

and choose the rest of $|g_i\rangle$ such that the matrix M is tridiagonal, and that these vectors are V-orthogonal:

$$\begin{aligned}
\langle g_i|VG_0V|g_{i-1}\rangle = \langle g_{i-1}|VG_0V|g_i\rangle &= \beta_{i-1}, && (2.91)\\
\langle g_i|VG_0V|g_i\rangle &= \alpha_i, && (2.92)\\
\langle g_i|VG_0V|g_j\rangle &= 0 \qquad \text{for } |i-j|>1, && (2.93)\\
\langle g_i|V|g_j\rangle &= \delta_{ij}. && (2.94)
\end{aligned}$$

We are using symmetric scalar product instead of Hermitian one, since the G_0 is symmetric and non-Hermitian operator.

The desired T-matrix element can be then written as

$$T_{11}^N = \langle\phi|V|g_1\rangle(M^{-1})_{11}\langle g_1|V|\phi_i\rangle = \frac{\langle\phi|V|\phi\rangle}{1-\alpha_1-}\frac{\beta_1^2}{1-\alpha_2-}...\frac{\beta_{N-2}^2}{1-\alpha_N}. \qquad (2.95)$$

We used expansion of matrix element M_{11}^{-1} of tridiagonal matrix in form of continued fraction. We will now outline the Lanczos algorithm of construction of bases $|g_i\rangle$ as well as variables α_i and β_i:

$$\begin{aligned}
|g_1\rangle &= |\phi\rangle\langle\phi|V|\phi\rangle^{-1/2}, && (2.96)\\
\beta_0 &= 0, && (2.97)\\
|r_i\rangle &= G_0V|g_i\rangle - \beta_{i-1}|g_{i-1}\rangle, && (2.98)\\
\alpha_i &= \langle g_i|V|r_i\rangle, && (2.99)\\
|s_i\rangle &= |r_i\rangle - \alpha_i|g_i\rangle, && (2.100)\\
\beta_i &= \langle s_i|V|s_i\rangle, && (2.101)\\
|g_{i+1}\rangle &= \beta_i^{-1}|s_i\rangle. && (2.102)
\end{aligned}$$

In our calculation, we will also need approximation off-diagonal T-matrix T_{fi}^N elements or wave function $|\psi_+^N\rangle$:

$$T_{fi}^N = \langle\phi_f|V|\psi_+^N\rangle = \sum_{i=0}^{N}\langle\phi_f|V|g_i\rangle(M^{-1})_{i1}\langle g_1|V|\phi_i\rangle, \qquad (2.103)$$

where the first column of matrix M^{-1} can be expressed as

$$(M^{-1})_{i1} = \prod_{j=1}^{i-1}\frac{\beta_i}{f_i}\frac{1}{f_N}, \qquad (2.104)$$

and

$$f_i = 1-\alpha_i-\beta^2/f_{i+1},\ f_N = 1-\alpha_N. \qquad (2.105)$$

The method has also been generalised for symmetric treatment of in and out channels [63]. For our purposes, the method described here is sufficient.

Our Schwinger-Lancoz calculation is usually using up to one hundred steps to reach our requested precision of changing relative T-matrix of less than 10^{-13}.

3. Model for H + H$^-$

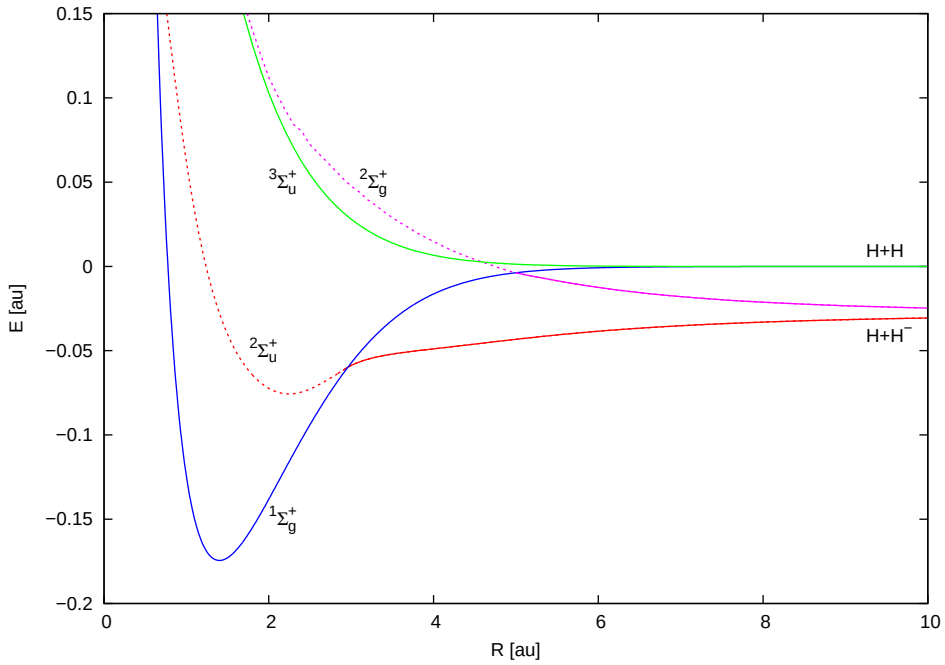

Figure 3.1: Potential energy curves of H_2 and H_2^-. The full lines represent bound states of all electrons of interest. The dashed lines are resonances of the H_2+e$^-$ complex in continuum of neutral molecule. The hydrogen potential curves are well known. The $^1\Sigma_g^+$ is the spin singlet, the 'g' stands for spatially symmetric bound configuration and the spin triplet state $^3\Sigma_u^+$ is the spatially anti-symmetric anti-bound configuration.

The hydrogen molecule potential curves are well known since the twenties of the last century (see for example [64]). We are using data from accurate variational calculation with explicitly correlated wave-functions done by Kołos and Wolniewicz [36] in 1965. These correspond to the $V_0^\alpha(R)$ potentials introduced in section 2.1, which are necessary to construct the final states of detachment processes (2.55) as well as the non-local potential (2.50). We will label these states with the spin state multiplicity, i.e. the state $^1\Sigma_g^+$ as $\alpha = 1$ and state $^3\Sigma_u^+$ as $\alpha = 3$. In our calculations we are using cubic spline to interpolate between the calculated points. We now define the continua (shown as red and green lines in figure 3.1) with energy $V_0^{(\alpha)} + k^2/2$. To construct the model for the nuclear dynamics we will also need the discrete states potentials $V_d^{i,j}(R)$ and the couplings $V_{dk_l}^{i\alpha}$.

We will now discuss the coupling between the discrete state and continuum. We assume that only the lowest two angular momenta of the electron are relevant (i.e. $l \in \{0, 1\}$). For the energies of interest this approximation is valid as the electrons with larger angular momentum are forced out by the centrifugal barrier and their contribution should be much much smaller. We must also consider the role of the symmetry of this molecule. We are dealing with the two lowest electronic states with different parity (gerade and ungerade). For clarity sake we

will use the letters 'u' and 'g' as index for the discrete state (i.e. $i, j \in \{(g), (u)\}$). The symmetry must be conserved throughout the electron detachment process and so not all of the couplings can be non-zero. If parities of a discrete state and a neutral molecule differ, then the electron in continuum must have odd angular momentum to conserve the parity. Conversely if the parities are the same, then the electron has even angular momentum. So in our case the only non-zero couplings are $V^{(u)\to(1)}_{dk_{l=1}}$, $V^{(u)\to(3)}_{dk_{l=0}}$,$V^{(g)\to(3)}_{dk_{l=1}}$,$V^{(g)\to(1)}_{dk_{l=0}}$. We add the symbol $\to$ between the identifier of a discrete state and a neutral molecule for lucidity sake. If we rewrite the equation (2.50) for more continua and discrete states

$$\begin{aligned} f_J^{ij} &= \sum_l f_{J;l} = \sum_{l,J'\alpha} (2J'+1) \begin{pmatrix} l & J' & J \\ 0 & 0 & 0 \end{pmatrix} \\ &\int \mathrm{d}E' V^{i\alpha}_{dk'l}(R) G^{(\alpha)}_{0J'} \left(E - k'^2/2, R, R' \right) V^{j\alpha\,*}_{dk'l}(R'), \end{aligned} \tag{3.1}$$

we see that restricted to the couplings, the matrix f_J^{ij} has the following structure

$$f_J = \left(\begin{array}{c|c} f_J^{(u)} & 0 \\ \hline 0 & f_J^{(g)} \end{array} \right). \tag{3.2}$$

Without loss of generality, we assume that the coupling $V^{(u)\to(3)}_{dkl=0}$ is negligible, because the transition is energetically forbidden as the resonance $^2\Sigma_u^+$ never crosses the potential curve of the anti-bound state $^3\Sigma_u^+$.

The last remaining ingredient to the nuclei dynamics is the discrete potential V_d^{ij}. Because of the symmetry of the problem this decouples to

$$V_d^{ij}(R) = \delta_{ij} V_d^{(i)}(R). \tag{3.3}$$

The equations (3.2) and (3.3) guarantee that the Lippmann-Schwinger equation (2.54) does not couple the two discrete state components and that we can solve the dynamics separately for gerade and ungerade component like in the case of one single discrete state. The potentials $V_d^{(i)}(R)$ do depend on coupling, but can be related to the Born-Oppenheimer potentials. These should be the same as the real part of the local approximation of the non-local resonance model that was derived by Domcke [40] for one continuum and we naturally generalise it to

$$V_d^{(i)}(R) = V_{loc}^{(i)}(R) - \sum_\alpha \Delta^{(i)\to(\alpha)}(R, V_{loc}^{(i)} - V_0^{(\alpha)}). \tag{3.4}$$

Using this equation we can calculate the discrete potential if we know the Born-Oppenheimer potentials of neutral molecule and the system with one more electron. The bound states of H + H^- system are directly accessible by quantum chemistry. We are using data calculated by Senekowitsch et al. [43] for the $^2\Sigma_u^+$ state and by Paidarová [65] for the $^2\Sigma_g^+$ (circles in figure 3.1). The positions of the local potential in the region where it is not bound, should correspond to the resonances. These are obtained from the fixed-nuclei scattering. The $^2\Sigma_u^+$ resonance was described by Berman, Mündel and Domcke [42], who used projection operator calculations. The R-matrix calculation performed by Stibbe and Tennyson [66] revealed the positions and widths of $^2\Sigma_g^+$ resonance.

The determination of couplings $V_{dkl}^{(i)\to(\alpha)}$ is described in the next section. It is obtained from the relation of the square of the coupling to the width of resonance.

For $V_{loc}^{(i)}$ and $V_{d}^{(i)}$ that satisfy the equation (3.4) we get negatively taken double of the imaginary part of the local complex potential

$$\sum_{\alpha} \Gamma^{(i)\to(\alpha)}(R, V_{loc}^{(i)} - V_0^{(\alpha)}), \tag{3.5}$$

where $\Gamma^{(i)\to(\alpha)}$ is related to the coupling V_{dkl} through (2.67). This should be identical with the widths calculated in [66].

As we will be dealing with indistinguishable nuclei (case of H $+\mathrm{H}^-$ and D + D^-), we should take into account the statistic of the identical particles. This determines the factors in the partial wave expansions (2.58) and (2.59), (it is $s_i = \frac{1}{2}$ for the distinguishable nuclei for H + D^- and D + H^-). For fermions, i.e. particles with half-integer spin, we know that the wave function of N of such particles satisfy

$$\psi(n_1, ..., n_N) = \mathrm{sgn}(p)\psi(n_{p_1}, ..., n_{p_n}), \tag{3.6}$$

where the p stands for permutation with sign $\mathrm{sgn}(p)$ and the n_i denote the position and spin of i-th particle. The similar equation holds for bosons (particles with integer spin) but without the sign of permutation.

$$\psi(n_1, ..., n_N) = \psi(n_{p_1}, ..., n_{p_n}), \tag{3.7}$$

We will limit ourselves to the system of two identical particles. The relation between spin and statistics of particles, in special case of two identical particles can be expressed as

$$\psi(n_1, n_2) = (-1)^{2s}\psi(n_2, n_1). \tag{3.8}$$

Swapping the particles is equivalent to

$$\mathbf{R} \to -\mathbf{R}, \tag{3.9}$$

in the spatial part of the centre of mass coordinates system. In the partial wave expansion this leads to the change of sign for odd angular momentum J. The spin part of the wave function χ with total spin S and z-axis component ξ that describe two particles with spin s and z-axis spin projection ξ_1 and ξ_2 as

$$\chi_{S\xi}(\xi_1, \xi_2) = \langle s\xi_1|\langle s\xi_2|Sss\xi\rangle = (ss\xi_1\xi_2|S\xi), \tag{3.10}$$

where the $(ss\xi_1\xi_2|S\xi)$ is a Clebsch-Gordan coefficient. If we use the known relations of these coefficients, we obtain

$$\chi_{S\xi}(\xi_1, \xi_2) = (-1)^{S-2s}\chi_{S\xi}(\xi_2, \xi_1). \tag{3.11}$$

Combining all of these we get relation

$$(-1)^S = (-1)^J, \tag{3.12}$$

that holds for two identical particles. Our wave function also includes an electronic part that depends on the internuclear distance R and we must include this too. (This is special case of geometric Berry phase). Swapping the nuclei

(3.9) leads to a change of the sign of the electronic wave function according to $\phi(\mathbf{r}; -\mathbf{R}) = \phi(-\mathbf{r}, \mathbf{R})$. This means the equation (3.12) can be rewritten as

$$(-1)^S = (-1)^{J+s_{el}}, \tag{3.13}$$

where we denote the symmetry of the electronic part with s_{el} and we set its value to one if the symmetry is ungerade and to zero it it is gerade.

Let us now find what states are allowed for system with two protons (spin one half) and two deuterons (spin 1). We start with two protons. These can have total nuclear spin S zero and one. For $S = 0$ (singlet) we can have even states for ${}^2\Sigma_g^+$ states and odd for the ungerade one. The other total nuclear spin allowed is one (spin triplet) and here it is the other way around.

For deuterium it is almost the same, but we have also the $S = 2$ the spin quintet and it will contribute to the single ones from previous paragraph.

If we sum all this and assume that all states have the same abundance we can determine the statistical factors s_i mentioned in equation (2.58). For hydrogen, these are $s_i = \frac{1}{4}$ for ${}^2\Sigma_g^+$ with odd angular momentum and for ${}^2\Sigma_u^+$ with even angular momentum and $s_i = \frac{3}{4}$ for the rest. For deuterium it is $s_i = \frac{2}{3}$ and $s_i = \frac{1}{3}$ respectively.

In the next section we will talk about long range potential for H + H^- interaction and we will follow with sections about models we are using for our calculations.

3.1 Construction of the model functions

We will start this section by describing the model for the ${}^2\Sigma_u^+$ state ($V_d^{(g)}$, $V_0^{(1)}$ and $V_{dk}^{(u)\to(1)}$) that was used in previous calculation done by Čížek et al. [27, 58]. Next we introduce our new model (with $V_d^{(g)}$, $V_0^{(1)}$ and $V_{dk}^{(g)\to(1)}$) for ${}^2\Sigma_g^+$ and how we construct it. Than we compare it with the model previously published[1] by Beliaev [67] that has both continua – adding coupling $V_{dk}^{(g)\to(3)}$ and anti-bounding hydrogen potential $V_0^{(3)}$ and explain how we modified it to agree with newer calculations of the Born-Oppenheimer potential.

3.1.1 Interactions of the ${}^2\Sigma_u^+$ discrete state

Couplings and location of resonance for ${}^2\Sigma_u^+$ state of H + H^- system was calculated by Berman, Mündel and Domcke [42, 41] using Feshbach projection operator formalism. The Born-Oppenheimer potential $V_{loc}^{(u)}(R)$ for R where all electrons are bound was calculated by Senekowitsch et al. [43]. This was used by Čížek [27, 58] to construct the model presented here. The discrete state potential $V_d^{(u)}$ satisfies the equation (3.4) (with only one term in the sum), where the local potential is assumed to be energy of electronic bound states for larger R and resonances for the small R. Čížek et al. [27] found that these assumptions are accurately satisfied by

[1] Model of Belyaev was proposed for the problem of three-body bound states of H_3^-. Our model is the first non-local model of ${}^2\Sigma_u^+$ and ${}^2\Sigma_g^+$ states for H+H^- collision.

$$V_d^{(u)}(R) = \begin{cases} 1.74\mathrm{e}^{-2.37R} - \frac{94.4\exp(-22.5/R)}{((R-2.54)^2+3.11)^2} + E_a \text{ for } R \leq 10.6au \\ -0.00845R\mathrm{e}^{-0.35R} - \frac{2.25}{R^4} - \frac{97}{r^6} \text{ for } R \geq 10.6au \end{cases} \tag{3.14}$$

and the coupling to continuum

$$V_{dk}^{(u)\to(1)} = \frac{1}{\sqrt{2\pi}} \sum_{i=1}^{3} A_i E^{3/4} \mathrm{e}^{b_i E} g_i(R), \tag{3.15}$$

where $E = k^2/2$ and

$$g_i(R) = exp(-c_i(R - R_0)^2) \text{ for } i = 1, 2, \tag{3.16}$$

$$g_3(R) = exp(-c_3(R - R_0)). \tag{3.17}$$

where $A_1 = 1.6618$, $A_2 = 1.3603$, $A_3 = 1.0467$, $b_1 = 18.8631$, $b_2 = 4.6559$, $b_3 = 1.4503$, $c_1 = 0.2$, $c_2 = 0.3302$, $c_3 = 0.489$, and $R_0 = 1.4014$.

The energy dependence of $\Gamma(E)$ defined by (2.67) in the form of $E^a \exp(-bE)$ is advantageous as it allows to express the Hilbert transform in definition of Δ (2.68) analytically [60] as

$$\begin{aligned} &\text{v.p.} \int \frac{E'^a \exp(-bE')}{E - E'} \mathrm{d}E' = \\ &= \begin{cases} -\Gamma(1+a)(-E)^a \Gamma(-a, -bE) \exp(-bE), & E < 0, \\ E^a \exp(-bE) \left[\pi \cot(a\pi) - \Gamma(a) (bE)_1^{-a} F_1(-a, 1-a; bE)\right], & E > 0, \end{cases} \end{aligned} \tag{3.18}$$

where $\Gamma(a, x)$ is incomplete gamma function and ${}_1F_1(a, b; x)$ is the confluent hypergeometric function. We are using a continuous fraction and a series expansion respectively(see Abramowitz and Stegun [68]) to evaluate them.

3.1.2 Interactions of the $^2\Sigma_g^+$ discrete state

For the bound state of this system we use Born-Oppenheimer potential calculated by Ivana Paidarová [65]. This was calculated using quantum chemistry methods. For system with three electrons the full CI calculations are possible and this leads to very accurate potential curve. In the region where the system is not bound, it is restricted by used bases and so it follows potential curve of neutral molecule, simulating system of neutral molecule with free electron restricted by used bases. The situation of the resonance in continuum is more difficult. It was studied by Bardsley and Cohen [69], who used variational method and found it above the anti-bound hydrogen states $^3\Sigma_u^+$. Bardsley and Wadehra [70] used semi-empirical analysis to find the position of the resonance only few meV above the triplet state of the neutral molecule. Esaulov [71] measured electron detachment and charge exchange for H^- + D with energy between 0 and 1 keV and estimated position of resonance at 0.8 ± 0.3 eV. We are using the more recent calculation done by Stibbe and Tennyson [66]. They calculated scattering of electron on the hydrogen molecule target using R-matrix method and then found position and the width of the resonance using time-delay matrix method and eigenphase sum method.

They mentioned that for inter-nuclear distances around 2.0 au the broadness of the resonance makes it difficult for the fitting procedure to be accurate and for lower R there is avoided crossing with the resonance that lies above. This is in the energy region around 10 eV that is above our energies of interest. For large R the resonance becomes narrower and fitting procedure should be more accurate.

First we develop model based on the data obtained from Paidarová [65], and Stibbe and Tennyson [66] with only one non-zero coupling $V_{dk}^{(g)\to(1)}$. We can separate this task to three parts.

For low $R \in [1.2, 4]$ au we have the positions of resonances and corresponding resonance widths from Stibbe and Tennyson [66]. We use equation (3.5) and Wigner's threshold law [72] to find the $V_{dk}^{(g)\to(1)}$ coupling. At the same time equation (3.4) yields the discrete potential curve $V_d^{(1)}$ that is needed for equation (3.5).

For large R (where the electron is bound to hydrogen as anion) is the coupling small and we use the extrapolation of the coupling constructed it the first region. We are still using equation (3.4 for the discrete potential $V_d^{(1)}$ and local potential calculated by Paidarová. We include correct asymptotic behaviour for even larger values of R.(See the end of this section).

The last region is for R around the crossing, where we don't have accurate local potential curves. We are using polynomial interpolation of $V_d^{(1)}$ as well as extrapolation of coupling mentioned in previous paragraph.

Using this procedure we found coupling in agreement with the widths provided by Stibbe. We will designate this model as (α):

$$V_{dk}^{(g)\to(1)}(R,E) = \frac{1}{\sqrt{2\pi}} \sum_{i=1}^{2} g_i(R) f_i(E), \tag{3.19}$$

$$g_1(R) = 0.53 \frac{0.9}{\left(1 + (R-4.2)^2\right)^{0.3}} \frac{1}{1 + \exp(0.5(R-4.2))}, \tag{3.20}$$

$$g_2(R) = 0.145 \exp(-1.5(R-1.8)^2), \tag{3.21}$$

$$f_1(E) = E^{1/4} \exp(-5E), \tag{3.22}$$

$$f_2(E) = E^{1/4} \exp(-E). \tag{3.23}$$

The factor $E^{1/4}$ is from the Wigner's threshold law, and the factors for energy dependent exponentials are put here by hands and then we estimated the dependence on R and fitted the rest of the parameters. The comparison of this model and the data that we used to construct it is on the figure 3.2 and 3.3 .

We compare this to the model that was constructed by Belyaev et al. in [67]. They used the data from [66] and Bardsley and Wadehra [70] for ${}^2\Sigma_g^+$ potential to construct their model. First we tried to compare this model with our own, and so we take only the coupling with continuum corresponding to ground state of hydrogen molecule and calculate the $V_d^{(g)}$ the same way as we did for our model. We could not use the $V_d^{(g)}$ that was presented with the full model as we are using only part of this model and it would shift the local potential. We will refer to this model as (β):

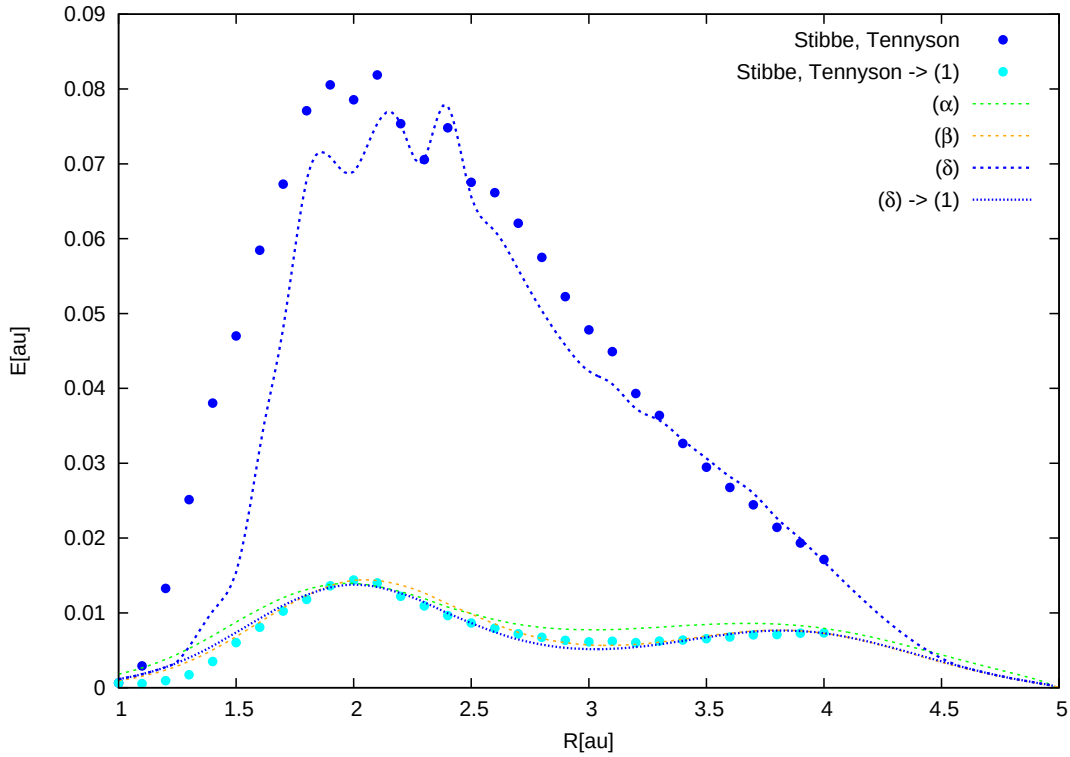

Figure 3.2: Comparison of resonance width presented by Stibbe and Tennyson [66] and the ones calculated from different models. The model (α) and (β) has only gerade coupling and so we comparing them to the $\Gamma^{(g)\to(1)}$ part of the width. We are not presenting the widths here corresponding to the model (γ) as the solution of non-linear equation (3.4) is not unique in most of the region we are interested in and showing all solutions will make this figure less lucid.

$$V_{dk}^{(g)\to(1)} = \frac{1}{\sqrt{2\pi}} \sum_{i=1}^{2} g_i(R) f_i(E), \tag{3.24}$$

$$g_1(R) = 0.33 \exp(-1.2(R-1.8)^2), \tag{3.25}$$

$$g_2(R) = 0.22 \exp(-0.7(R-4)^2), \tag{3.26}$$

$$f_1(E) = f_2(E) = E^{1/4} \exp(-2.7212E). \tag{3.27}$$

We found that this model is similar to the model (α), as can be seen on the figure 3.2 and 3.3.

Next we add the second continuum from Belyaev's model and use their $V_{dk}^{(g)}$ in the system dynamics. We will call this model (γ). The missing coupling is:

$$V_{dk}^{(g)\to(3)}(R,E) = \frac{1}{\sqrt{2\pi}} \sum_{i,j=1}^{2} g_i(R) f_i(E), \tag{3.28}$$

$$g_1(R) = 5.8 \exp(-1.8(R-1.74)^2), \tag{3.29}$$

$$g_2(R) = 4.6 \exp(-0.15(R-3.1)^2), \tag{3.30}$$

$$f_1(E) = f_2^{(u)}(E) = E^{3/4} \exp(-15E). \tag{3.31}$$

Potential for the discrete state is spline interpolation of the table that can be found in the paper by Belyaev et al.[67]. Figure 3.3 shows that these are not in a good agreement neither for bound state nor with the position of the resonance according to the Stibbe et al. We are not presenting the widths for this potential, as there are multiple solutions for the local potential, and the width is not continuous for neither solution we found. As we will be using mostly the next model and use this only for comparison we are not much concerned about this.

The last and final model is constructed from the couplings of Belyaev's model and then we use the same procedure as for models (α) and (β). This model we will mark as (δ) and we use this as the final model. It follows the ab initio data in figure 3.2 and 3.3 reasonably. The discrepancies are of the order of 10%.

The long range potential is important for reaction of our interest. And it has huge impact on cross sections for low energies.

The long range potential for H + H^- like interaction is dominated by polarisation, that is the same for gerade and ungerade state. Polarisation potential is well known:

$$V_{pol}(R) = -\frac{2.25}{R^4} - \frac{97}{R^6}. \tag{3.32}$$

It is important for detachment processes, but has little effect charge transfer. The next correction to long range potential is the interaction between the neutral hydrogen and the loosely bound electron in H^-. This can be described well with the term

$$V_{lr} = \pm \frac{A \exp(-BR)}{R}, \tag{3.33}$$

where $\pm$ is for the gerade and the ungerade state respectively. We used the ab initio data to fit these parameters to $A = 0.439$ and $B = 0.258$ for $R > 10$. In this region we use $V_d = V_{lr} + V_{pol}$ as our discrete state potential.

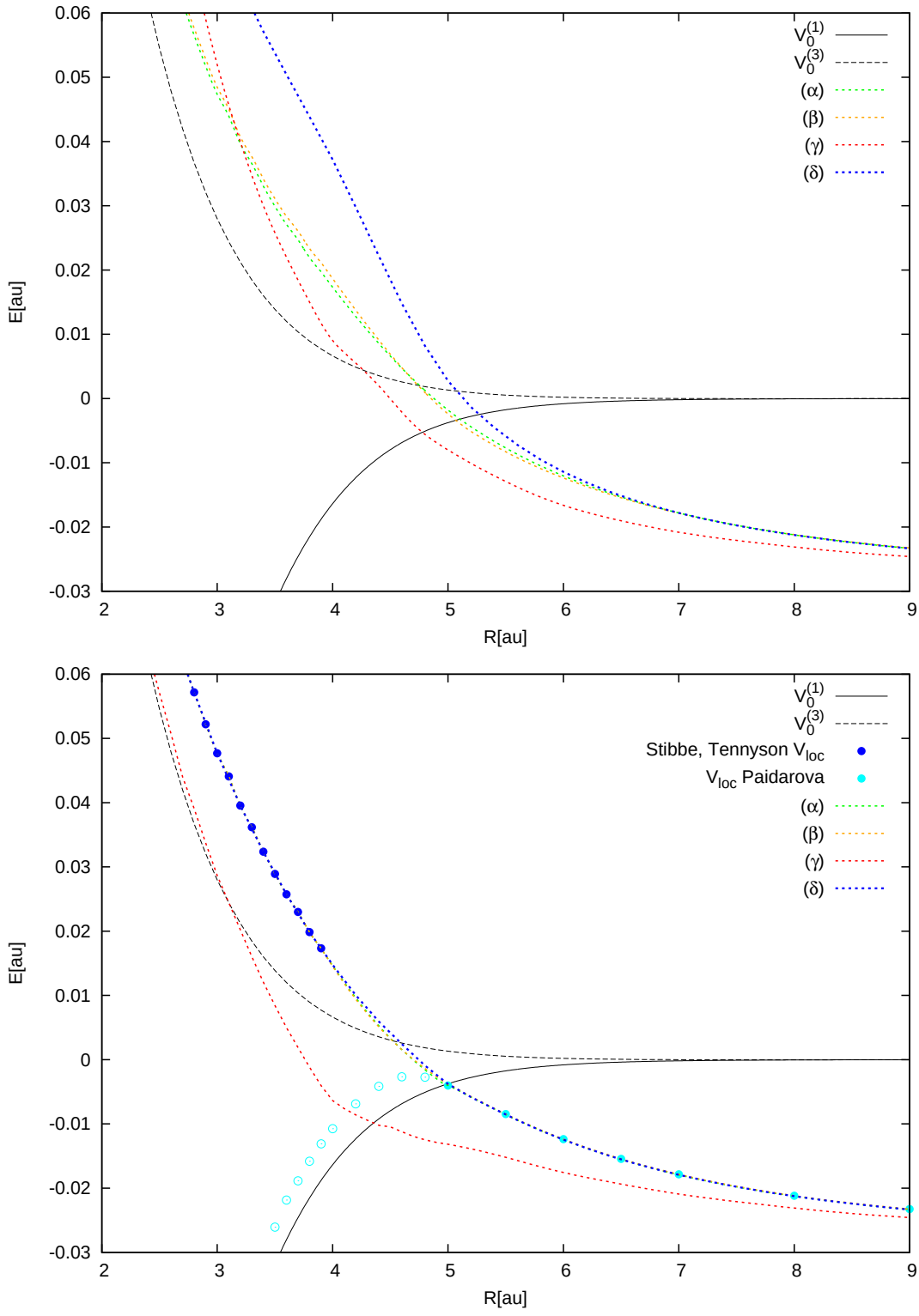

Figure 3.3: Comparison of potential energy curves for different models. On top there are potentials for the discrete state and in the bottom are the local potentials of the $^2\Sigma_g^+$ state/resonance. The calculation from which we construct our models are marked with circles. The empty circles correspond to the calculation by Paidarová [65] that are already in continuum and used method doesn't calculate the energy correctly. Our final model used for calculations is (δ).

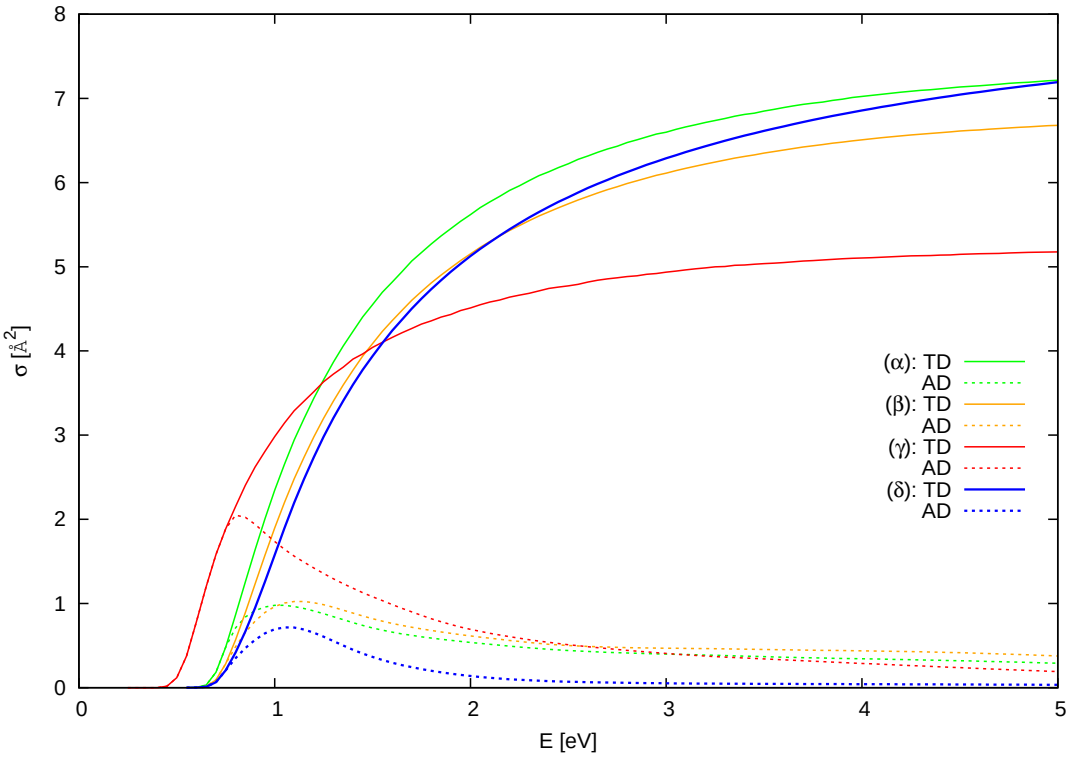

Figure 3.4: Comparison of total detachment (TD) and associative detachment (AD) cross sections for different models for H+D$^-$ collision with initial states in gerade symmetry.

3.1.3 Comparison of models

We constructed these previously described models for state $^2\Sigma_g^+$. We can see that the models (α) and (β) that include only coupling $V_{dk}^{(g)\to(1)}$ are almost identical as the local potential curve V_{loc} and the corresponding width go.

To asses the sensitivity of associative detachment data to uncertainty of the model data we used all four model (α) - (δ) to calculate $^2\Sigma_g^+$ contribution to the total detachment in H + D$^-$. The comparison of the total detachment and the associative detachment cross sections can be seen in figure 3.4. For the total detachment, i.e. the sum of associative (1.1) and the collision detachment (1.2), all models with exception of (γ) agree within $\sim$ 10 % accuracy. Model (γ) is different since it does not use the accurate ab initio data of Paidarová [65], which can be seen in particular on position of the onset of the cross section. Associative detachment is more sensitive to the details of the model. We see that the presence of the second continuum, included only in complete model (δ) makes associative detachment cross section smaller. This opens the possibility, that the system ends up in the second $H_2(^3\Sigma_u^+)$ + e$^-$ continuum, that does not contribute to associative detachment ($^3\Sigma_u^+$ potential does not support the bound states) so it lowers the associative detachment.

4. Results and discussion

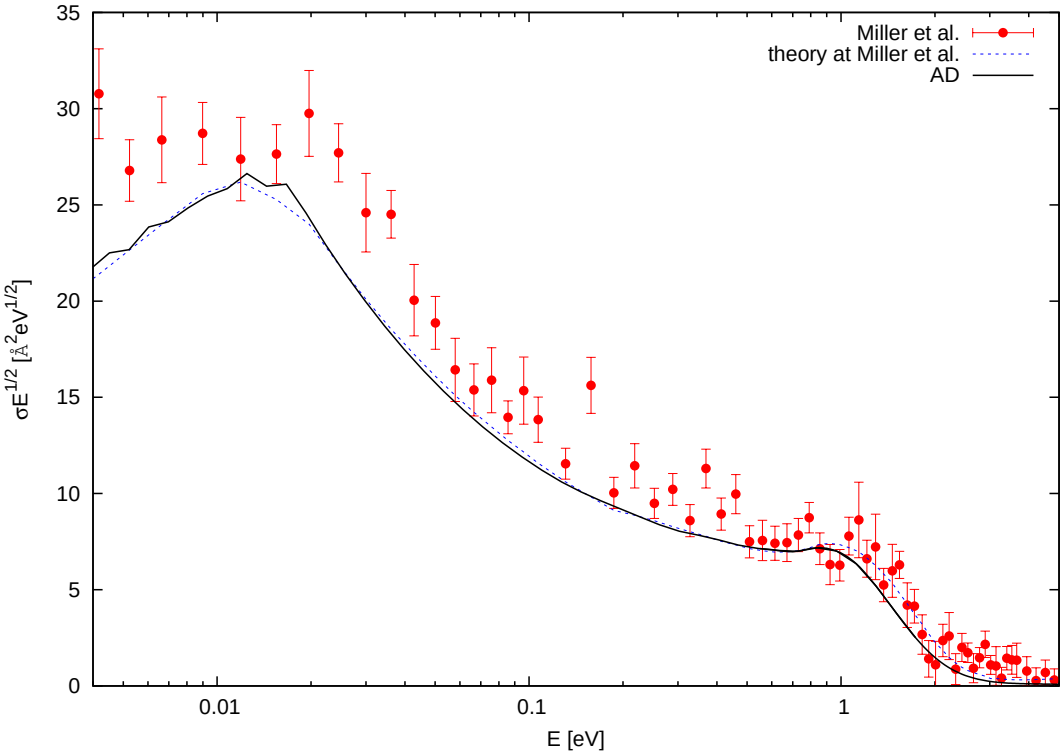

Figure 4.1: Comparison of the cross section of associative detachment for H + H^- measured by Miller et al. [56]. Solid line is and our calculation of associative detachment that includes both $^2\Sigma_g$ and $^2\Sigma_u$ channels. Dashed line includes also the quasi-bound states of H_2, Cross section was multiplied by square root of energy for better lucidity.

As discussed in the introduction the first calculation for the associative detachment in H + H^- fully including the non-local nature of the electron detachment was done by Čížek et al. [27]. It was limited to energies lower than 1 eV.

This collision is interesting for the higher energies as the new channel, the collision detachment, opens. It is also expected that the $^2\Sigma_g$ state will play a role here. We were also motivated by new experimental data for H + H^- measured by Miller et al. [55]. The data can be seen in figure 4.1 together with associative detachment calculation that includes both $^2\Sigma_g$ and $^2\Sigma_u$ contributions and we also show associative detachment with the inclusion of metastable states (blue doted line). The detachment to the metastable states is part of collision detachment, but these states have lifetime long enough to be detected by the experimental set-up as hydrogen molecules. The details about our calculation for this comparison can be found in [55] included in appendix B.

In the following section we will show more detailed analysis of H+H^- collision. We stared with associative and collision detachment in the next section. We show contribution from $^2\Sigma_g$ and $^2\Sigma_u$ states and spectra of outgoing electrons for few selected energies of the collision. Next we will discuss the isotopic effect that was partially published in [56] (also is included in appendix B). And finally we

will talk about the charge transfer and the elastic scattering. These processes were made accessible to our calculation by including both gerade and ungerade symmetries. Our calculation is thus the first one that that treats these processes using the full non-local calculation.

4.1 Associative and collision detachment for H+H$^-$

The associative detachment on fig 4.1 is dominated by the $^2\Sigma_u$ contribution. Contribution from the $^2\Sigma_g$ that we added is highest around 1 eV and even there it is only about 10%. At about the same energy there is steep fall of this cross section as the collision detachment channel opens. We start by comparison of the total detachments, i.e. sum of collisional and associative detachment, for the $^2\Sigma_u$ and $^2\Sigma_g$ states.

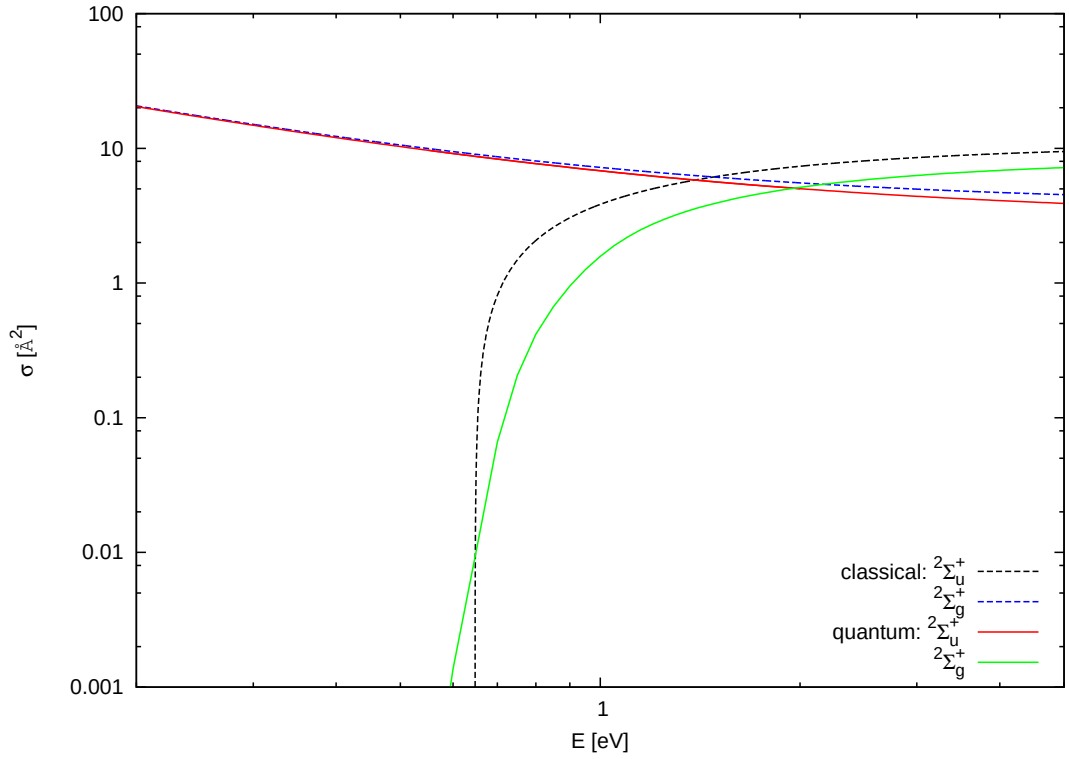

Figure 4.2: Total detachment cross section comparison of classical approximation and quantum calculation for $^2\Sigma_g^+$ and $^2\Sigma_u^+$ initial states.

We start analysis of the total detachment by classical means. This will help us to get better physical intuition for this type of collisions. We can find the maximal impact parameter b, that for all $R > R_x$ satisfies

$$E - V_{loc} - \frac{Eb^2}{R^2} \geq 0, \tag{4.1}$$

where R_x is the position of the crossing of V_0 and V_{loc}. With assumption that the detachment process always occurs when the system gets to the autodetachment domain ($R < R_x$) we can calculate the classical total cross section as πb^2 with this maximal impact parameter. If we have only polarisation potential $V \sim 1/R^4$ this is so called Langevin cross section, that is $\sigma \sim 1/E^{1/2}$. For $^2\Sigma_u$ state the potential is more attractive than the pure polarization term and even the classical calculation gives values larger than Langevin model. The gerade state behaves more like a potential barrier. For this we can estimate the behaviour of cross section as

$$\sigma = \pi a^2 \left(1 - \frac{E_0}{E}\right) \tag{4.2}$$

where E_0 is height of the barrier and a is its position. We have potential curves, that are much more complicated and so we used numerical calculation to determine classical cross section for both gerade and ungerade states. For $^2\Sigma_u$ states the classical calculation agrees closely with full dynamics (figure 4.2).

The situation for $^2\Sigma_g^+$ state is very different from $^2\Sigma_u^+$ state (figure 4.2). Low energy cross section of $^2\Sigma_u^+$ state is dominated by long range polarisation potential and the quantum effects make it even larger. For $^2\Sigma_g^+$ state, the low energy behaviour is dominated by potential barrier, that is crossed around 0.7 eV and then it rapidly grows. The classical calculation leads to $1/E$ behaviour near the onset and quantum calculation provides bigger cross section for classically forbidden region, where the tunnel effect is involved (figure 4.2). For larger energies, the cross section of quantum calculation is lower because it respects, that crossing this barrier doesn't leads strictly to detachment. The local potential is still growing even after crossing and the non-local the time the particle spends behind crossing is not long enough (in comparison with width) to detach the electron. Although the $^2\Sigma_u^+$ is dominant for low energies, for energies $E \gtrsim 2\,\mathrm{eV}$ total detachment of the other state prevails.

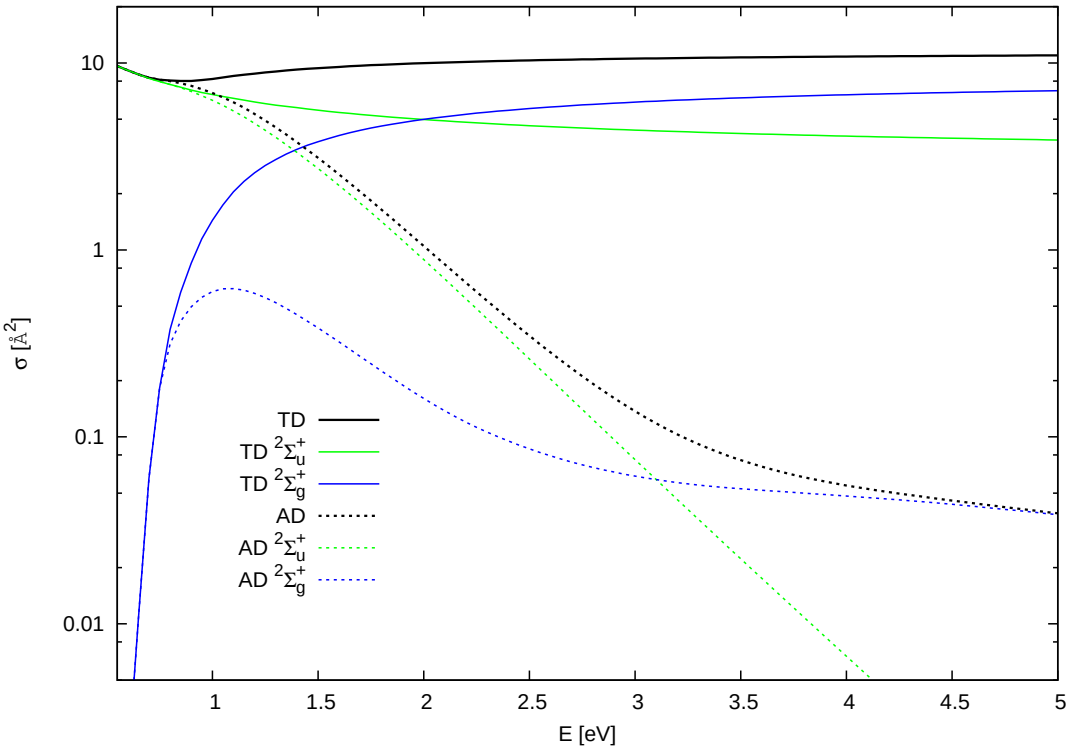

Figure 4.3: Total detachment (TD) and associative detachment(AD) cross section for interaction H + H$^-$. This figure shows contribution to AD (dashed lines) and TD (solid lines) from both initial states $^2\Sigma_g^+$ (green) and $^2\Sigma_u^+$ (blue) for energy were is the contribution from gerade state relevant.

Let us now look in more detail on the total and the associative detachment (see figure 4.3). We can see there that the collision detachment (difference between total detachment and associative detachment) channel opens shortly after outset of detachment for $^2\Sigma_g^+$ state. The $^2\Sigma_u^+$ is much more important for associative detachment. The maximal contribution of $^2\Sigma_g^+$ state is around 10% at energy of

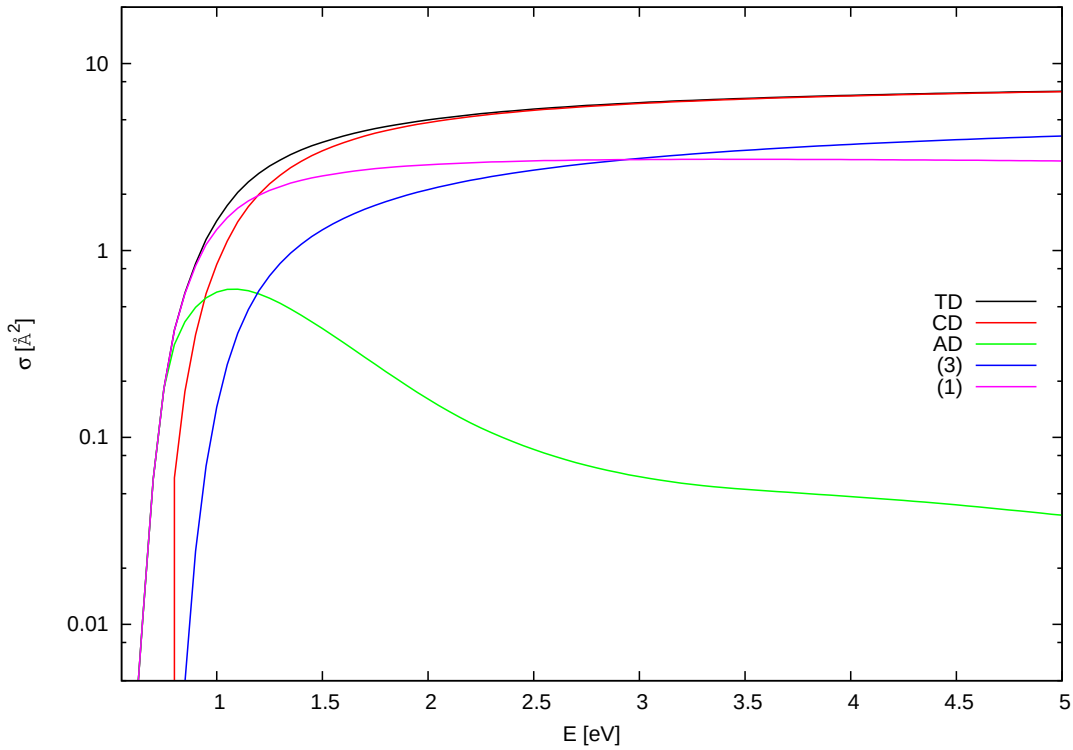

Figure 4.4: Different channel for detachment of $^2\Sigma_g^+$ initial state. The associative detachment is low due to the steep growth of local potential as well as opening of the channel with electron p-wave.

1 eV. Although it decreases much slower than the associative detachment cross section for $^2\Sigma_u^+$ state, when it reaches the comparable values (around 3 eV), it is probably too small for any practical purpose. There are several reasons for the cross section to be small. One is that there is the competing collision detachment channel to excited dessociative $^3\Sigma_u^+$ state of neutral molecule. The width corresponding to this channel is larger than the one corresponding to the ground state, but it is suppressed by higher angular momentum of electron and also by higher offset for opening of this channel. The other reason for the smallness of the associative detachment cross section is the threshold behaviour of the $\Gamma^{(g)\to(1)}$. This causes that the autodetachment occurs fast after arrival to the autodetachment zone, where the bound states of the molecule overlap only slightly and so most of the detachment it so the collisional detachment channel. This can be seen on figure 4.4. The detachment to the $^3\Sigma_u^+$ channel opens slower and around 3 eV takes over the other the channel to the electronic ground state of neutral molecule.

4.2 Electron spectra and final states distributions

We are also interested about spectrum of electrons that leave after the associative or collision detachment interaction. The cross section for outgoing electron with energy E_{el} and initial kinetic energy E is

$$\frac{\mathrm{d}}{\mathrm{d}E_{el}}\sigma(E_{el},E) = \sum_J \sum\!\!\!\!\!\!\int_\nu \sigma_{\nu J}(E)\delta(E - E_{\nu J} - E_{el}), \tag{4.3}$$

where $\sigma_{\nu J}$ is cross section for J-th partial wave and neural molecules (including continuum states) in state ν (the sum includes all rotation-vibrational states of the neutral molecule that has non-zero cross section $\sigma_{\nu J}$) . We use discretised continuum in our calculation, and so, strictly speaking, we cannot calculate this cross section. More to the point, no experimental set-up can measure with infinitely sharp electron energy resolution. When we assume that the detector measures with Gaussian distribution with width s we must convolute this distribution with the previous formula and we get

$$\sigma(E_{el},E) = \frac{1}{s\sqrt{2\pi}} \sum_J \sum\!\!\!\!\!\!\int_\nu \sigma_{\nu J}(E) \exp\left(-\frac{1}{2}\left[\frac{E - E_{\nu J} - E_{el}}{s}\right]^2\right). \tag{4.4}$$

This also solves our problem of discretised continuum, because we can use large enough width s so that our sampling of continuum is dense enough to give right result for the cross section. We confirmed the accuracy by increasing the density of continuum sampling and calculate the same cross section. The results for initial energies 0.75, 1, and 2 eV can be seen on figure 4.5. We choose the first energy slightly after the opening of the associative detachment channel of gerade state, the second one to be around the maximum of associative detachment of gerade state and the third one is around where the contribution from both symmetries to the total detachment cross section are the same. The cross section of $^2\Sigma_g^+$ state is most important in the low electron energy part of the spectrum.

The reason for this is following. The release of low energy electron is suppressed in $^2\Sigma_u^+$ contribution since only p-wave contributes with $E_{el}^{3/2}$ threshold behaviour. On the other hand the $^2\Sigma_g^+$ state decays also through release of s-wave electron with sharper threshold onset $E_{el}^{1/2}$. This explains dominance of the $^2\Sigma_g^+$ contributions in electron spectra close to the zero energy.

For better understanding of this process we can draw probability w of different modes of detachment depending on classical impact parameter b, e.g.

$$b = \frac{J}{\sqrt{2\mu E}}, \tag{4.5}$$

$$w = \sum_\nu \frac{2\mu E}{\pi}\frac{\sigma(\nu)}{2J+1}, \tag{4.6}$$

where J is initial angular momentum, E is initial energy, μ is the reduced mass of our system and sum goes over final states ν, that will contribute to process in

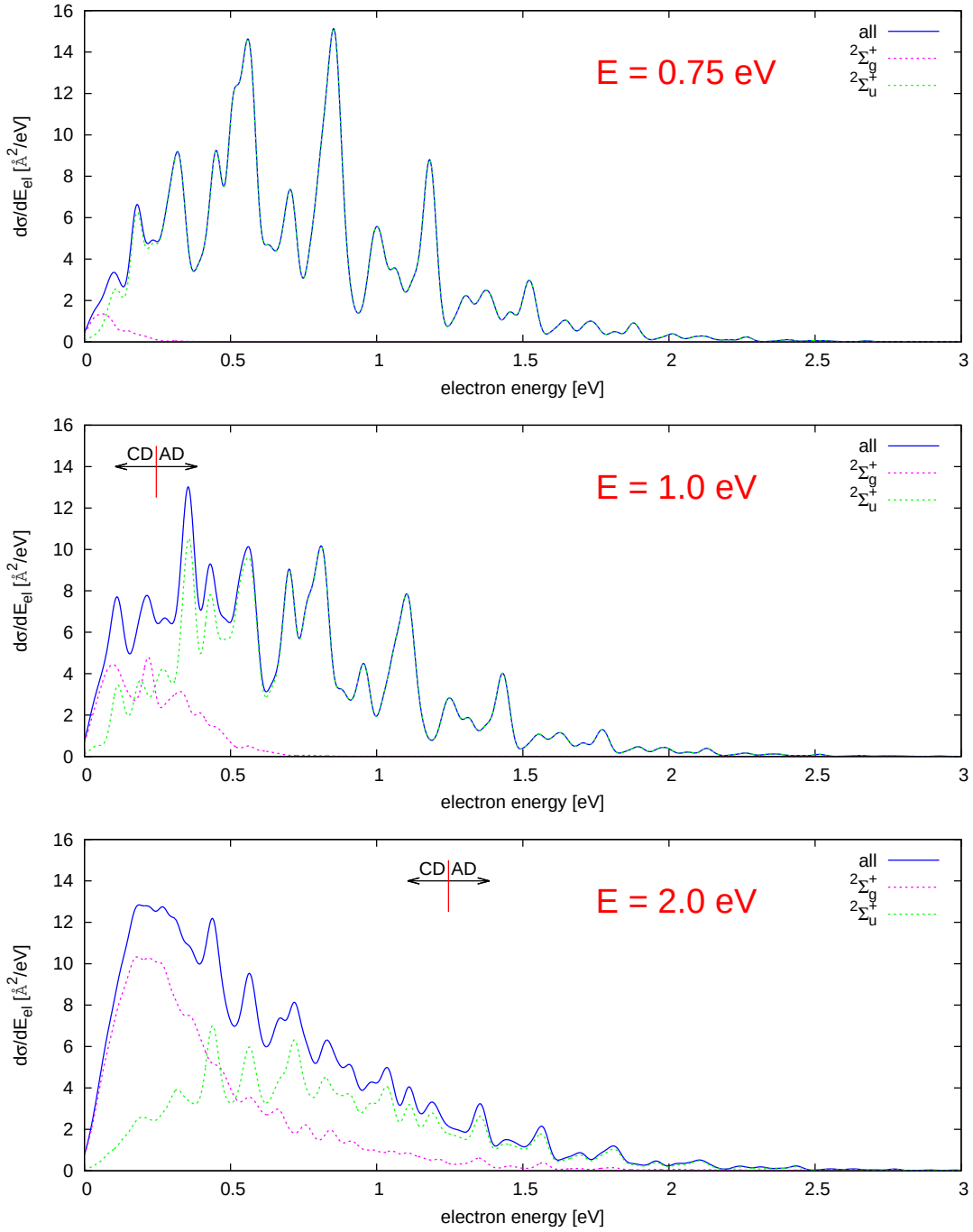

Figure 4.5: Cross sections for outgoing electrons energy in H + H$^-$ collision convoluted with Gaussian of the width of 20 meV. The figures from top to bottom are for initial energies 0.75, 1 and 2 eV. We show contribution of $^2\Sigma_g^+$ and $^2\Sigma_u^+$ initial states and we have marked the energy where the collision detachment changes to associative detachment (for 0.75 eV the collision detachment channel is closed).

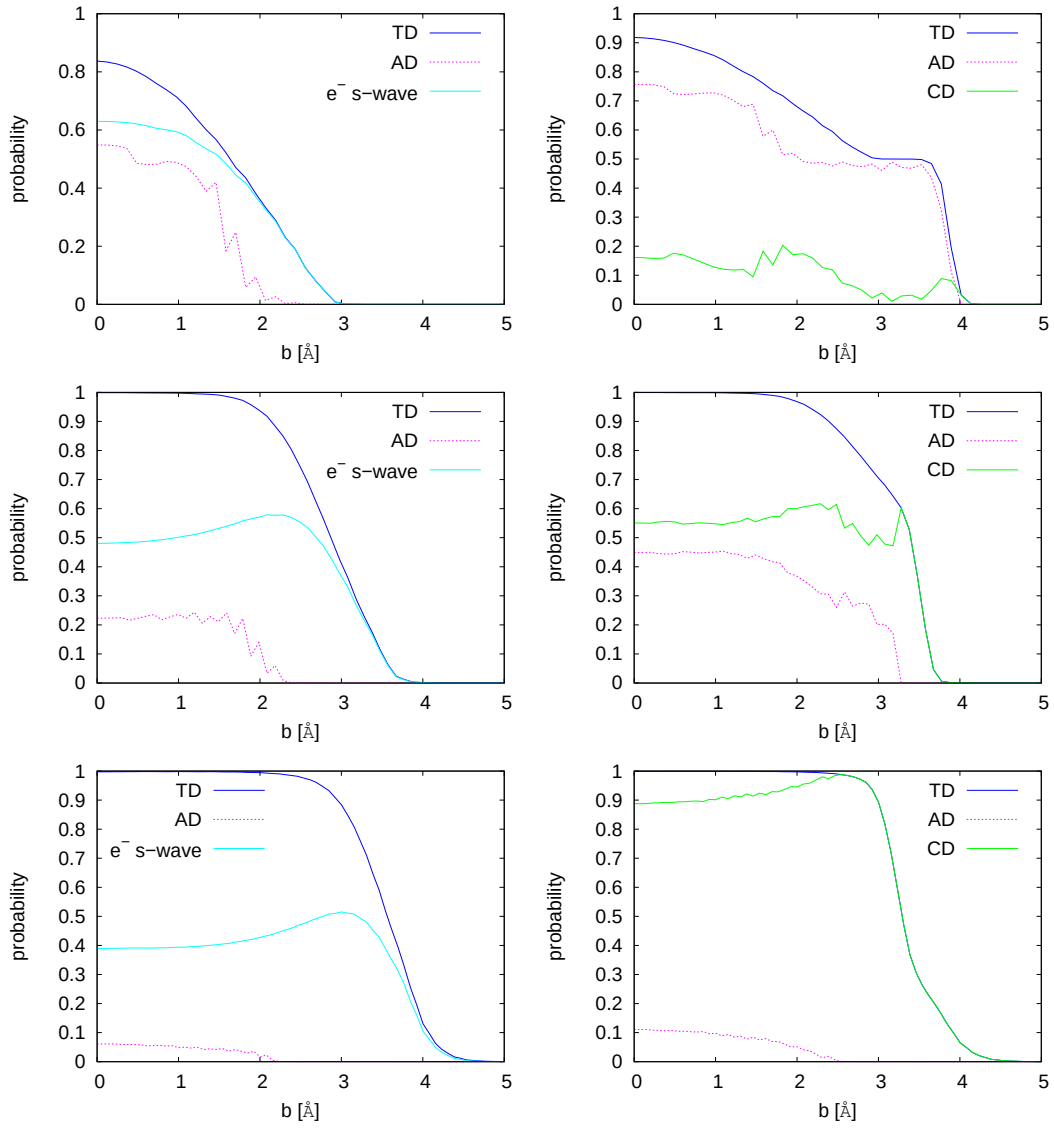

Figure 4.6: Probability of detachments depending on impact parameter for $^2\Sigma_g^+$ initial state on the left and complete H+H$^-$ collision on the right for energies from top to bottom 1, 1.5, and 2.5 eV. We are showing total detachment (TD), associative detachment (AD). For $^2\Sigma_g^+$ in the left part we also show separately the contribution from $^1\Sigma_g^+$ continuum as cyan curve. For the complete H + H$^-$ collision on the right the green curve denotes the contribution of collisional detachment(CD) alone.

question. In figure 4.6 we show these for a energies 1, 1.5, and 2 eV. This is a good indicator of the range of interaction that are relevant for the processes.

On the left hand side of figure 4.6 there is detail on the $^2\Sigma_g^+$ initial state. We can see that associative detachment contribution is more localized than the full total detachment, as the particle must penetrate deeper into the autodetachment region. For the larger impact energies the contribution to s-wave continuum grows before closing of detachment channel. This is caused by the threshold behaviour of the competing p-wave channel that is suppressed for large b.

On the right hand side are graphs for probability calculations from both gerade

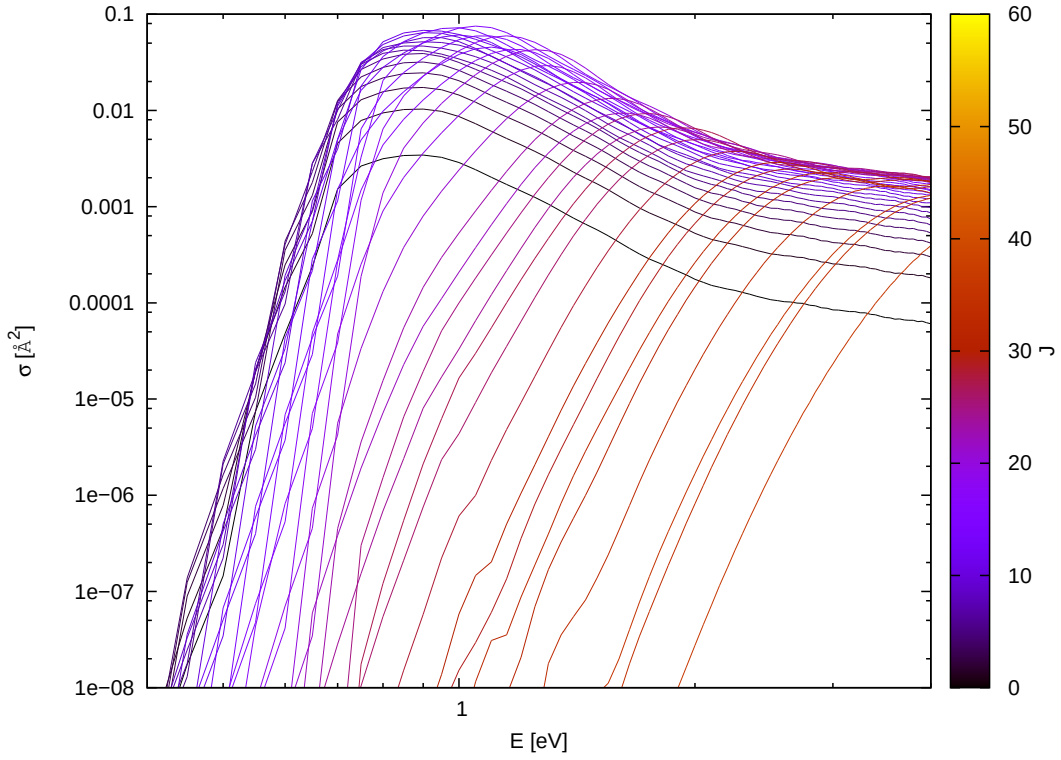

Figure 4.7: Detachment cross section to channels with different angular momentum of final HD molecule. This includes only Σ_g^2 initial state of H + D^- collision.

and ungerade channels. At the top there is good example of difference between the two channels. The gerade channel discussed above (left hand side of the figure) contributes as a brad between the $b = 0 - -3\mathring{A}$. The ungerade channel is flat followed by sharp drop at $b = 4$ which is consequence of the attractive interaction all the way to the autodetachment region.

We have calculated partial cross sections for associative detachment to all final states of molecule H_2 created in the process, but it is too extensive to present everything here. The data are included in the attachment that is described in appendix A.

In figure 4.7 we present present differential cross section for specific final angular momentum for H + H^- collision. We show this isotope, because statistical factors $s_i = 1/2$ are the same for the cross section increase for low J is mainly due to the statistical factor $(2J + 1)$ in equation (2.59). The low energy cross section is suppressed by centrifugal barrier for higher values of J.

Some additional data for partial cross sections are also shown in figures 4.13 and 4.14 in the section about isotopic effect.

4.3 Isotopic effect

In the classical analysis of total detachment cross section there is no difference between the isotopes. If we look at this situation from quantum perspective, more partial waves will contribute in heavier system. This is compensated by smaller cross section for individual partial waves and these two effects cancels each other and only small discrepancies remain in the total detachment cross sections (figure 4.8 for Σ_u^2), For Σ_g^2 contribution (figure 4.9) the difference is after all noticeable ($\sim 3\%$). This may be attributed to repulsive nature of the potential. The cross section is the highest for the D_2 which spends most time at the turning point.

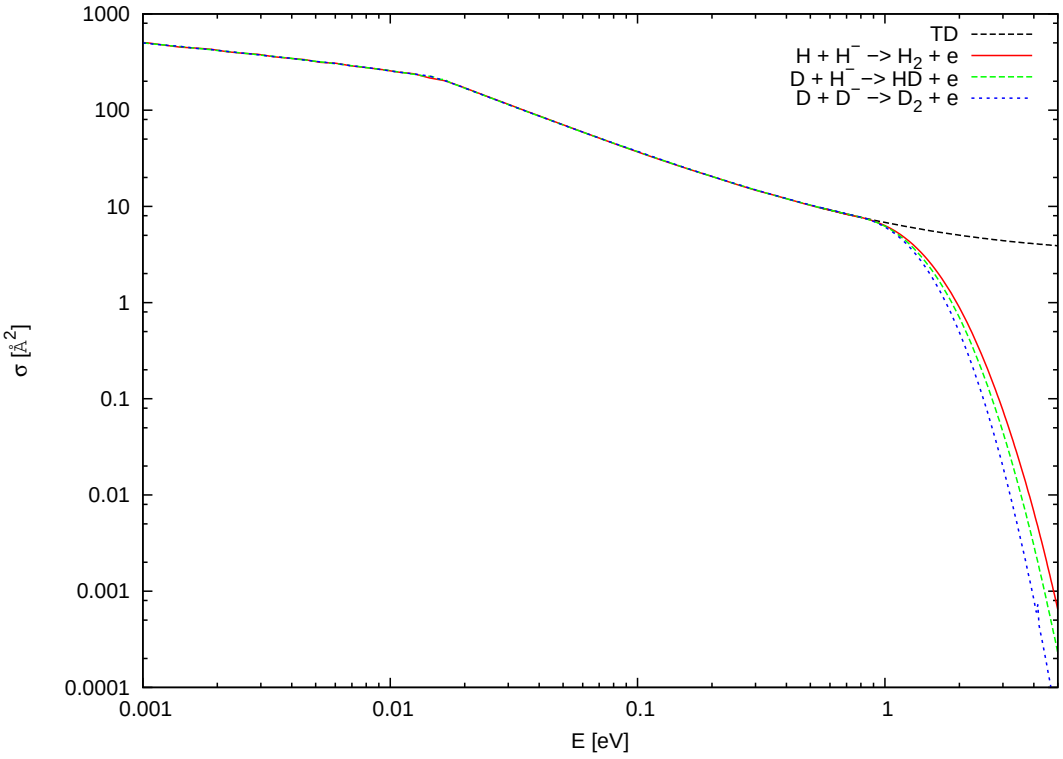

Figure 4.8: Isotopic effect of cross section for associative detachment and total detachment of $^2\Sigma_u^+$ initial state. The isotopic effect is notable, after opening of collision detachment channel. There is no noticeable isotopic effects in total detachment so we present only one line for the total detachment..

But if we look at associative detachment (figures 4.8 for Σ_u^2 and 4.10 for Σ_g^2) we can see large differences after the threshold for collision detachment. This is expected as the heavier system is more adiabatic and so the electron has more time to autodetach on the border of autodetachment region and with less energy transferred to it and the neutral system ends up more likely with more energy. The associative detachment cross section thus, in general, decreases faster, for heavier systems. This is also true for Σ_g^2 contribution in figure 4.10.

But interesting exception is for system in gerade symmetry around initial energy 1 eV. As we can see in figure 4.10 the highest cross section in this region is for H + D^-. To better understand this we point to the electron spectrum of this collisions at figure 4.11. There is comparison of electron spectra for all three system (convoluted with Gaussian of the width of 20 meV) for the Σ_g^2 state. The

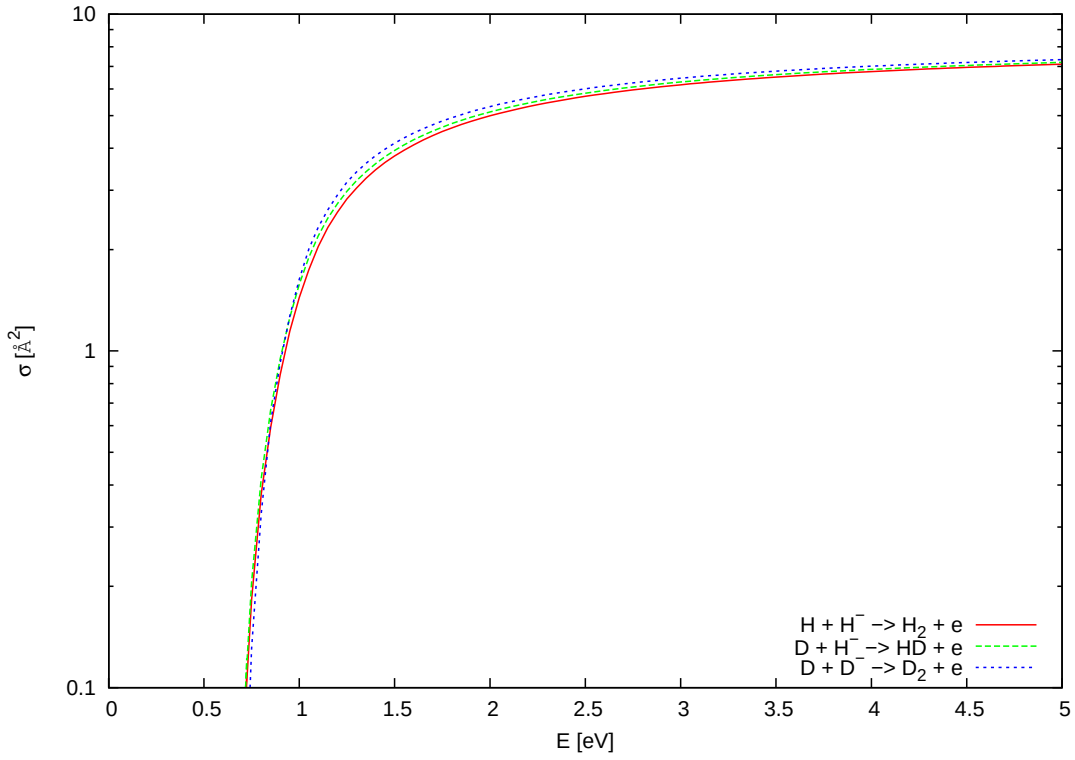

Figure 4.9: Isotopic effect of cross section for total detachment of $^2\Sigma_g^+$ initial state. There is nearly no difference in total cross section between different isotopes of hydrogen.

HD spectrum is much smoother. This is caused by the statistical factors s_i that in the case of HD don't depend on angular momentum. We marked the threshold between the associative and collisional detachment ($E_{el} = 0.246\,\mathrm{eV}$). We can see that this threshold is situated after the large spike in cross section for H_2 as well as D_2. These are caused mainly by statistical factor mentioned earlier. The D_2 has larger mass and so is more adiabatic as mentioned at the beginning of this section. This is consistent with the fast decrease of the differential cross section in electronic spectrum for larger electron energies. This also correspond with smaller associative detachment cross section that we see in figure 4.10.

We also include the spectra for outgoing electrons that includes both symmetries (figure 4.12) this time for impact energy 2 eV. At this energy the spectrum is dominated by contribution from the gerade states for lower electron energies and the contribution from ungerade states dominates at high energies (as can be see in figure fig:el-spect). We can see that smoothness of spectrum for HD collision is much less smoother (in comparison to the other two), especially around electron energy 0.5 eV, where contributions from gerade and ungerade parts are comparable. As pointed previously for heavier particles the spectrum decreases faster with electron energy, but has higher contribution on low electron region. This agrees with the fact, that associative detachment is smaller for heavier systems.

The experiments often measure reaction rates rather than the cross sections directly. Reaction rate has inherent isotopic affect. If we look at equation (4.20) for calculation of reaction rate from cross section we can see that only factor $1/\sqrt{\mu}$ deepens on mass and everything else depends only on energy. This and the

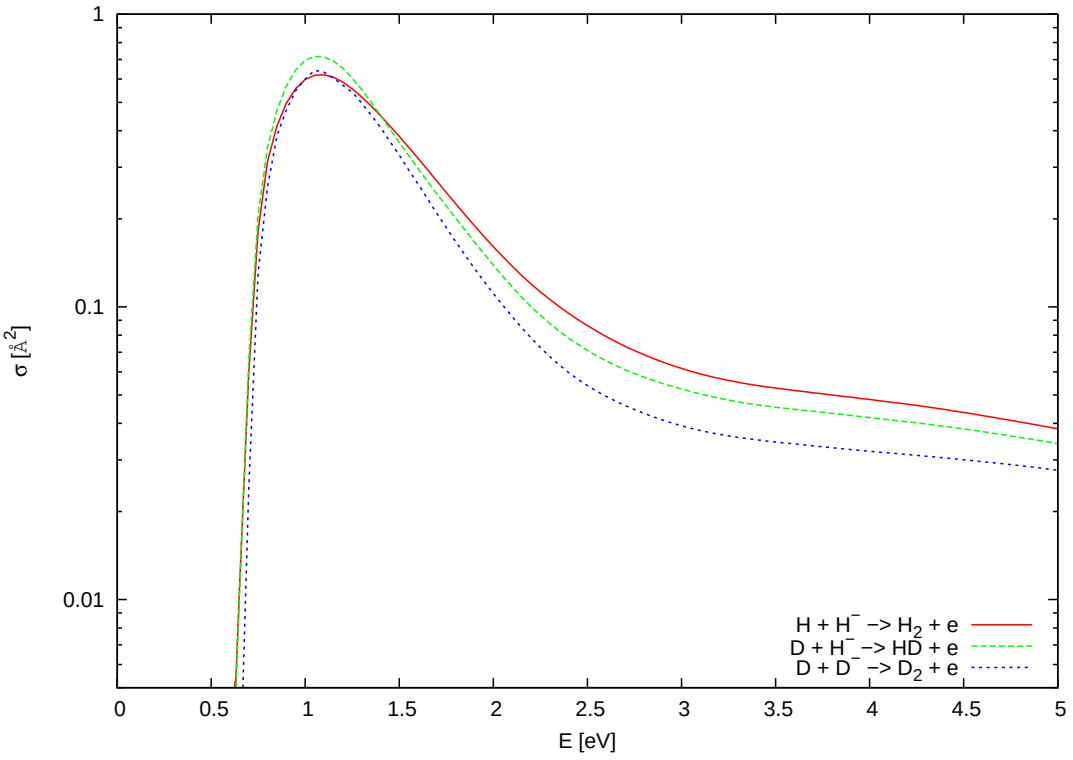

Figure 4.10: Isotopic effect of cross section for total detachment of $^2\Sigma_u^+$ initial state. There is nearly no difference in total cross section between different isotopes of hydrogen.

small differences between (energy dependent) cross section leads to

$$k = k_0 \sqrt{\frac{\mu_0}{\mu}}, \tag{4.7}$$

where the k_0 are reaction rates for system with reduced mass μ_0 and the μ is reduced mass of the system we want to calculate new reaction rate r.

The interesting comparison is also in figures 4.13 and 4.14 where we show individual partial cross sections for selected rotation-vibrational states of neutral molecule. We choose states with vibrational quantum number $v = 1$ and $v = 6$. We can see the above mentioned fact that the cross section getting smaller but the number of partial waves growing. We can also see that the frequency of oscillations decreases with the reduced mass. The oscillations can be explain by changing of overlap of incoming wave and the final state modulated by coupling. This is faster for the higher vibrational states as their wave functions oscillating faster. The isotopic effect then shifts the cross sections to the higher energies as the vibrational states are situated deeper in the interaction region. This effect is partially compensated by increased number of vibrational states for the heavier molecules.

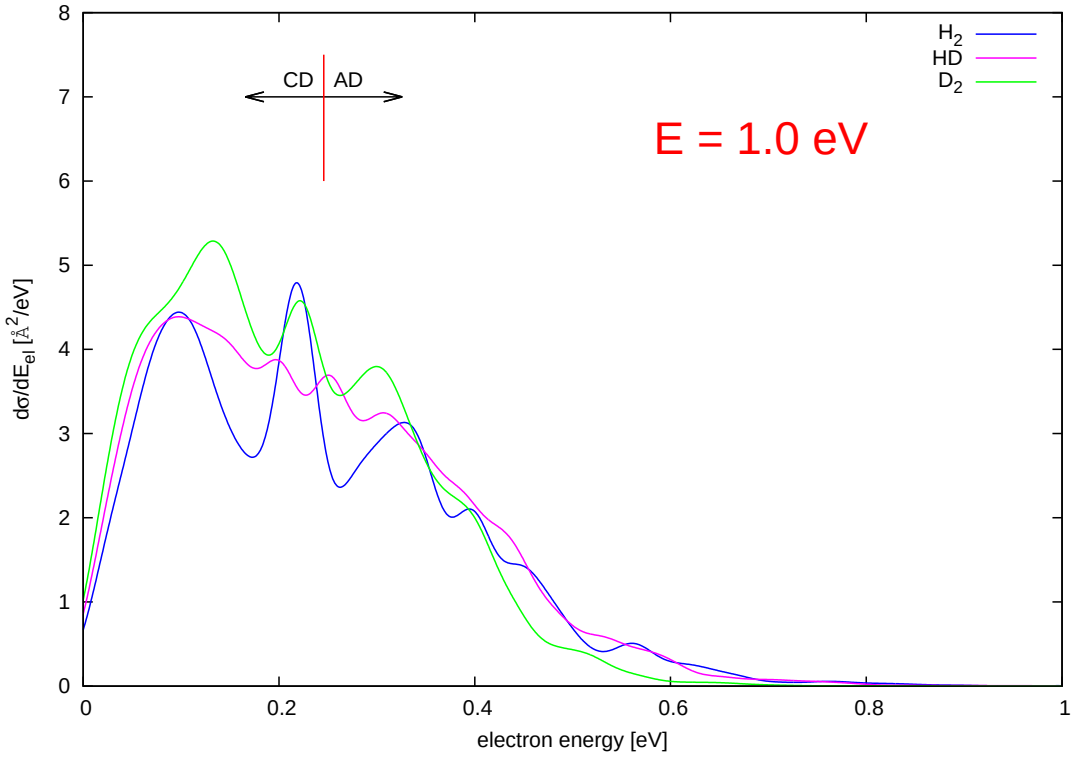

Figure 4.11: Spectra of outgoing electrons energy for H + H^- collision for collision energy 1 eV for the Σ_g^2 state. We are comparing spectra of different isotopes. The data are convoluted with Gaussian of the width of 20 meV.

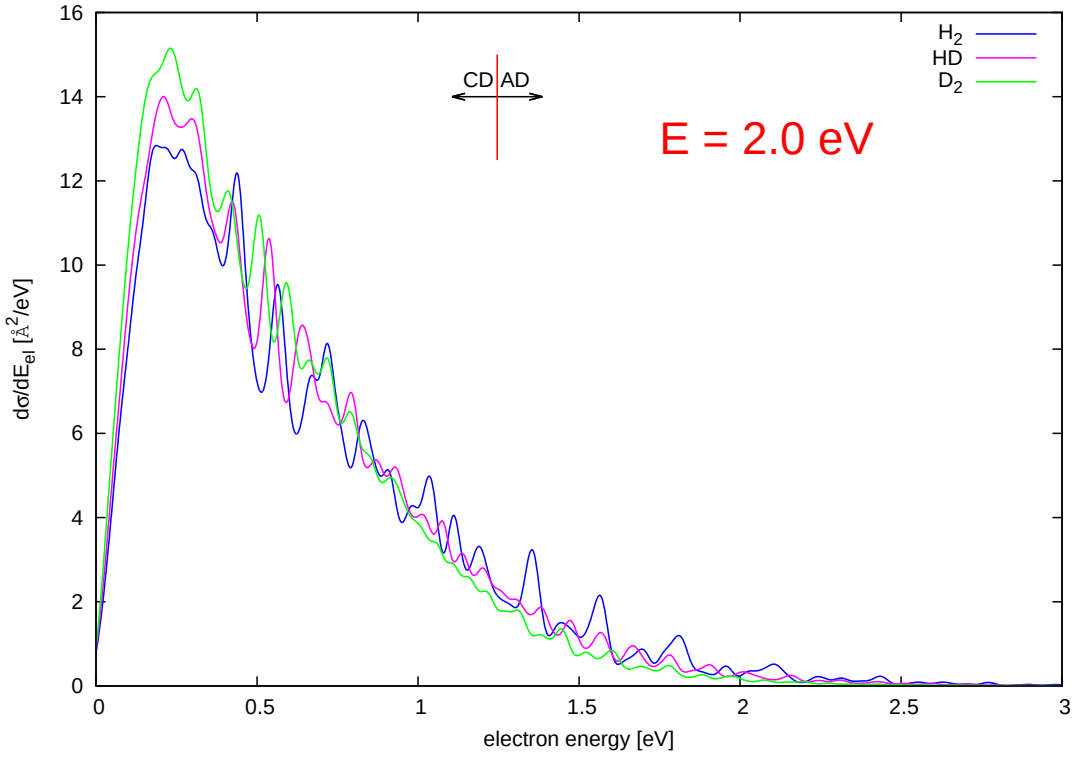

Figure 4.12: Spectra of outgoing electrons energy for H + H^- collision for collision energy 2 eV . We are comparing spectra of different isotopes. The data are convoluted with Gaussian of the width of 20 meV.

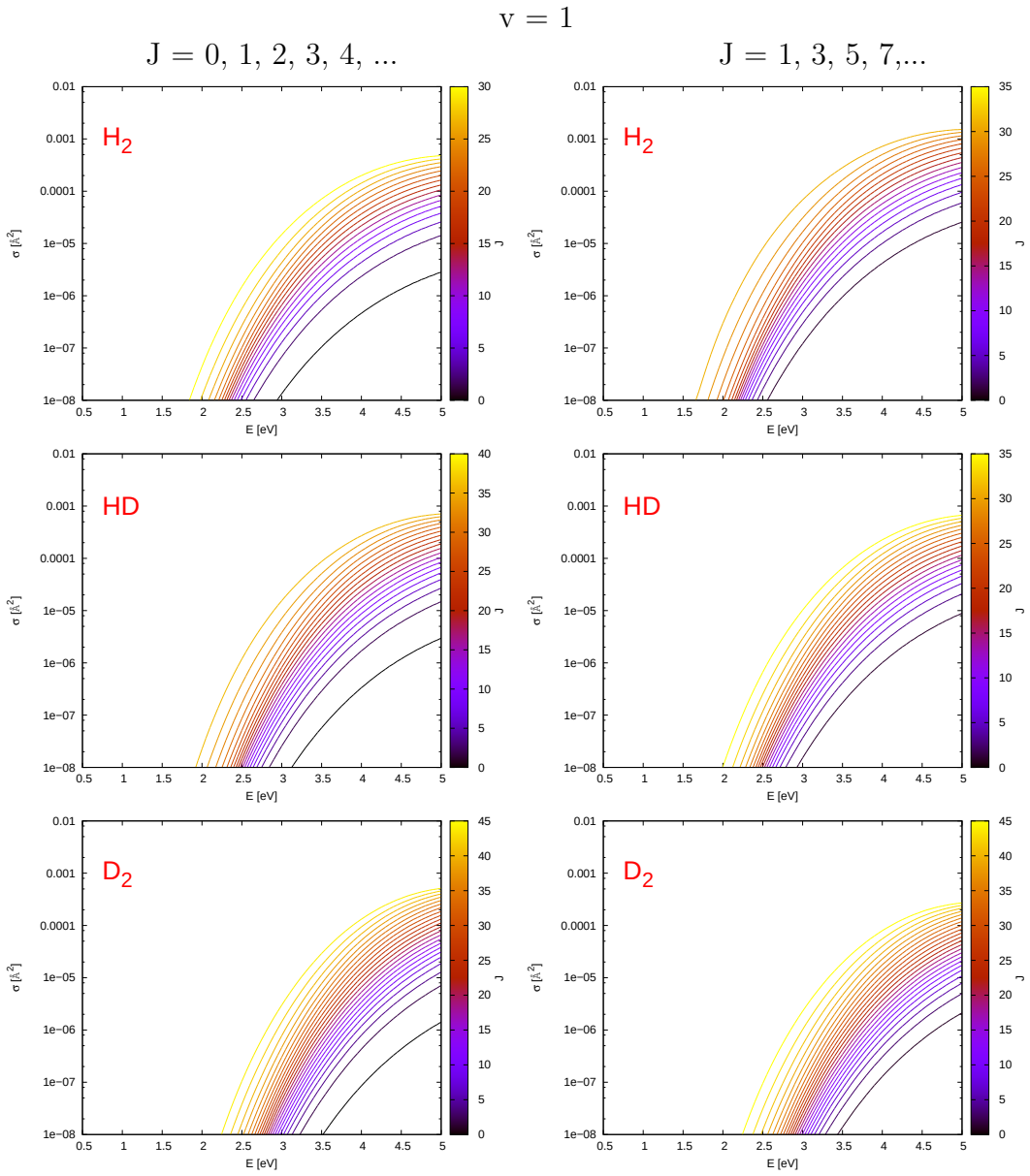

Figure 4.13: Cross sections of associative detachment with final molecule in the lowest vibrational state and different angular momentum l (even on the right and odd on the left) for initial state Σ_g^2 and collision of H + H^- (top), H + D^- or D + H^- (middle), and D + D^- (bottom).

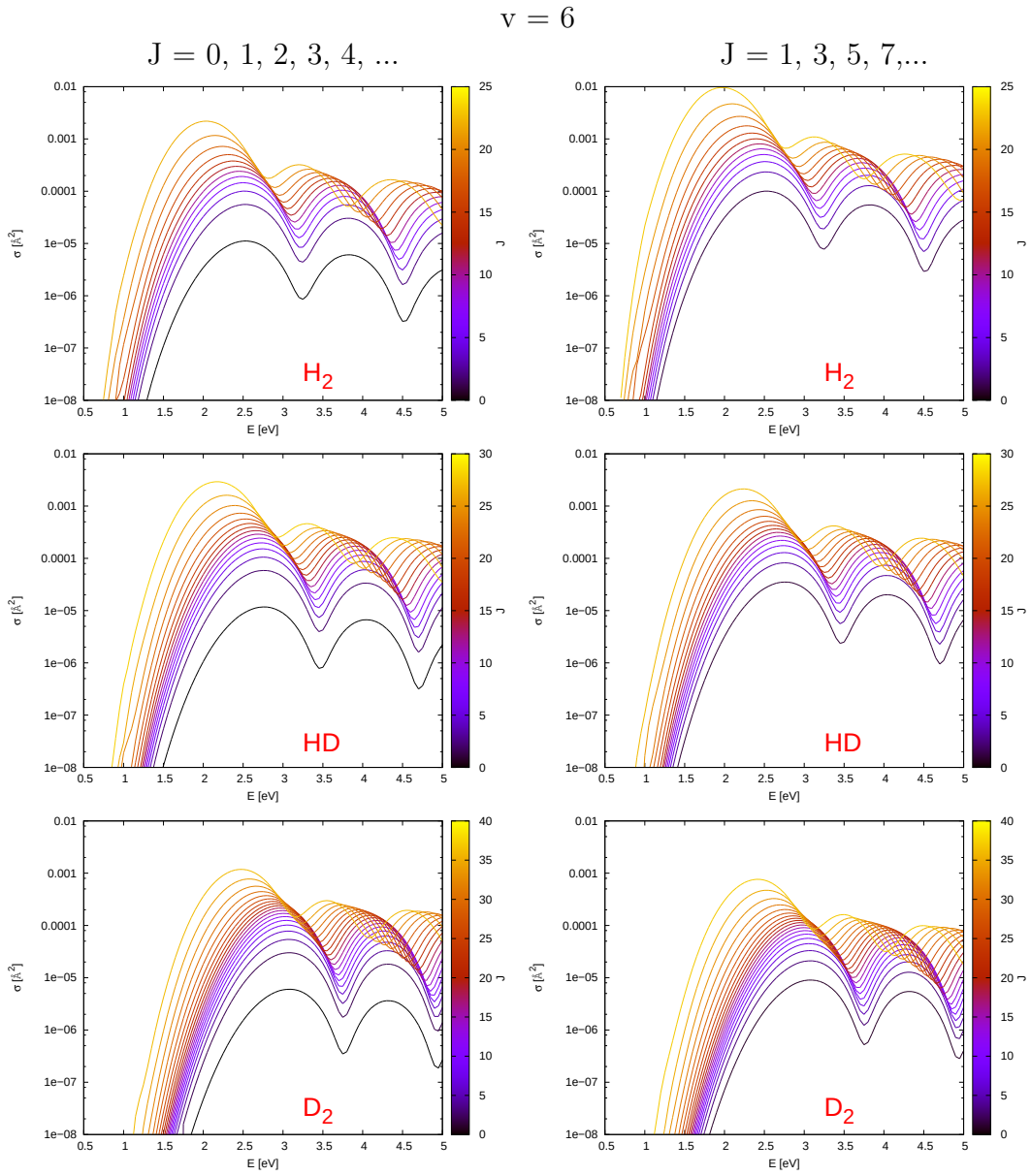

Figure 4.14: Cross sections of associative detachment with final molecule in the sixth lowest vibrational state and different angular momentum l (even on the right and odd on the left) for initial state Σ_g^2 and collision of H + H^- (top), H + D^- or D + H^- (middle), and D + D^- (bottom).

4.4 Charge transfer and elastic scattering

We will start this section with few paragraphs about theoretical description of these precesses and in particular with the questions arising from the symmetry of the system.

Particularly important case of diatomic system arises in collisions of two atoms with similar nuclei, i.e. with the same charge of the nucleus. The lowest state of such a system is inherently degenerate for large R, as both $A^- + A$ and $A + A^-$ must have the same energy. It is easy to see that electronic problem has an inversion symmetry and the wave function can be either even or odd (space inversion preserves wave function or it changes it's sign). It is obvious that hydrogen molecule has this symmetry and we will use it as an example. We can see on figure 2.1, that for large inter-nuclear distances the potential curves merge and as R gets lower it behaves differently for different symmetry – the gerade symmetry is more attractive for neutral molecule and repulsive for anion plus atom and ungerade vice versa.

Parity is quantum number that will be preserved throughout studied processes. We use standard terminology for these; gerade and ungerade (from German words meaning even and odd). It is obvious that both gerade and ungerade electron functions will have the same electron density around both nuclei for the large R. As we will be dealing only with the lowest electronic states we can simply define that the normalised sum of electron functions give wave function with electron on the left and the difference give wave function with electron localised on the right. Let us now discuss how this will reflect in nuclear motion.

We will first solve problems for each symmetry separately as these two problems decouple. We mentioned this earlier in chapter 3. This is achieved by solving equation (2.54) which gives the solutions $\phi^{(u)}$ and $\phi^{(g)}$. (We will omit the index J that stands for the angular moment of the partial wave, except for equations for the cross sections.) These functions describe the strange incoming boundary condition: linear combination of states with ion coming from the left ($H^- + H$) plus and minus ion coming from the right ($H + H^-$) respectively.

For the description of right the charge transfer we will need to decouple these boundary condition.

$$\phi^L = \frac{1}{\sqrt{2}}(\phi^{(u)} + \phi^{(g)}), \tag{4.8}$$

$$\phi^R = \frac{1}{\sqrt{2}}(\phi^{(u)} - \phi^{(g)}). \tag{4.9}$$

Using these states with localised extra electron we can describe charge transfer and find its S-matrix element and cross sections. The S-matrix can be expressed in terms of gerade and ungerade sub-problems.

$$\begin{aligned}\langle\phi^L|S|\phi^R\rangle &= \frac{1}{2}\left(\langle\phi^{(g)}| + \langle\phi^{(u)}|\right)|S|\left(|\phi^{(g)}\rangle - |\phi^{(g)}\rangle\right) = \\ &= \frac{1}{2}\left(\langle\phi^{(g)}|S|\phi^{(g)}\rangle - \langle\phi^{(u)}|S|\phi^{(u)}\rangle\right) = \frac{1}{2}\left(S^{(g)} - S^{(u)}\right),\end{aligned} \tag{4.10}$$

where $S^{(u)}$ and $S^{(g)}$ are S-matrices of ungerade and gerade sub-problem respectively and we used the fact that the mixed elements of S-matrix are identically

zero due to the inversion symmetry

$$\langle\phi^{(u)}|S|\phi^{(g)}\rangle = \langle\phi^{(g)}|S|\phi^{(u)}\rangle = 0. \tag{4.11}$$

Now we can use partial wave expansion and calculate S-matrices for each partial wave using NRM as described above. Large number of partial waves contributes to charge transfer. This calculation can be very expensive even though the non-local part potential does not contribute to the S-matrix.

Cross section for charge transfer is

$$\sigma^{CT} = 4\pi \sum_J (2J+1) \frac{|s_J^{(g)} - s_J^{(u)}|^2}{16p^2} = \pi \sum_J (2J+1) \frac{\sin^2(\Delta_J)}{p^2}, \tag{4.12}$$

Where the Δ_J is the difference between phase shifts for the gerade and the ungerade channels. The charge transfer is therefore highly sensitive to the difference of the long range potential between gerade and ungerade states.

We can also define the S-matrix elements for the elastic scattering in similar manner:

$$\begin{aligned} \langle\phi^L|S|\phi^L\rangle &= \frac{1}{2}\left(\langle\phi^{(g)}| + \langle\phi^{(u)}|\right)|S|\left(|\phi^{(g)}\rangle + |\phi^{(g)}\rangle\right) = \\ &= \frac{1}{2}\left(\langle\phi^{(g)}|S|\phi^{(g)}\rangle + \langle\phi^{(u)}|S|\phi^{(u)}\rangle\right) = \frac{1}{2}\left(S^{(g)} + S^{(u)}\right). \end{aligned} \tag{4.13}$$

The only difference between this and the S-matrix element for charge transfer is the sign between the terms. This means that the elastic cross section is much more sensitive to the long range potential, especially the polarization potential that is the same for both symmetries of initial state. The elastic cross section can be calculated as

$$\sigma^{ES} = 4\pi \sum_l (2l+1) \frac{|s^{(g)} + s^{(u)} + 2|^2}{16p^2}. \tag{4.14}$$

It can be expressed as a function of sine and cosine of the sum and difference of the phase shifts for each symmetry, but we will not be using it as it is not practical when the absorption to other channels is involved.

For the identical nuclei H^- + H and D^- + D the charge transfer is indistinguishable from the elastic process. We therefore concentrate on H^- + D in the calculation of charge transfer. As we discussed in the introduction there are some older calculation, but they are at much higher energies than we are interested in here – usually in order of keV. We can estimate the cross section for energies where one channel is absorbed and the other is not. Then the cross section of charge transfer should be a half of the associative detachment cross section. It should be mentioned, that this is never entirely true – there are always partial waves that are absorbed only partially and this can both increase or decrease charge transfer cross section. The similar assumption can be made about elastic scattering, but to elastic scattering contribute the partial waves that has similar phase shift in both symmetries (of electronic problem) that is cancelled out in charge transfer. Because of this, we expect the elastic cross section to be higher.

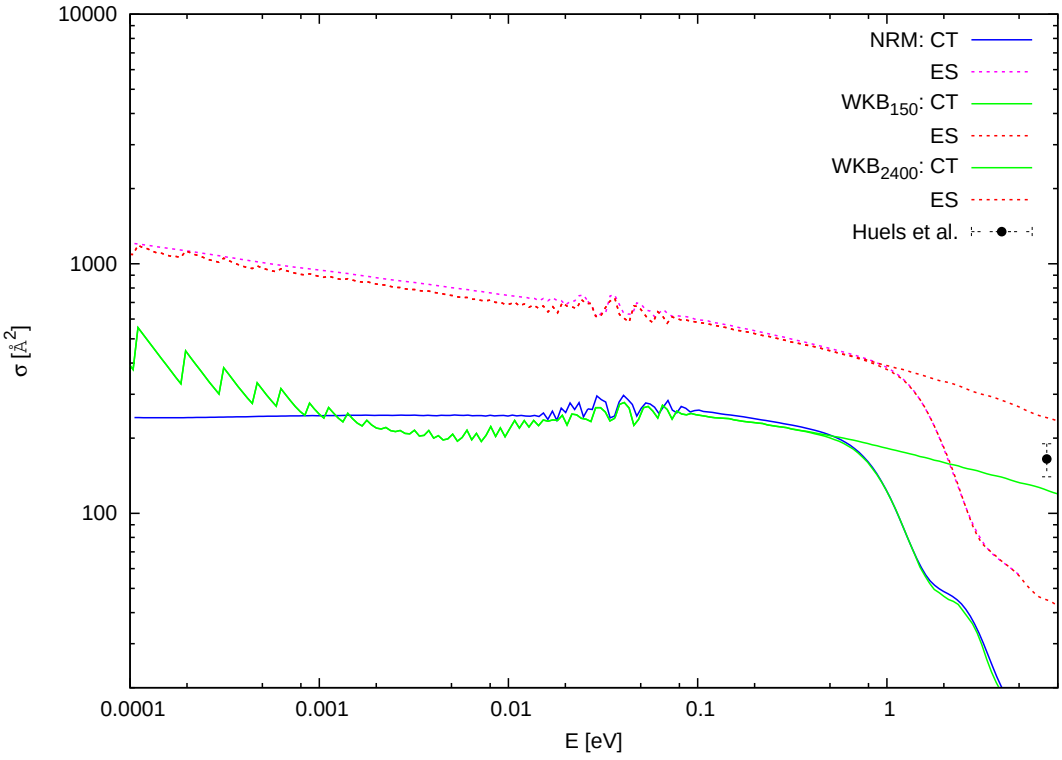

Figure 4.15: Cross sections for charge transfer and elastic scattering for $H^- + D$. Comparison of non-local resonance model (NRM) calculation with 150 partial waves, WKB approximation with 150 partial waves and converged WKB approximation with 2400 partial waves. We are comparing this with the measurement of Huels et al. [54] for charge transfer process.

We can use semi-classical calculation, namely WKB approximation, to calculate difference between phase shifts of gerade and ungerade system. Let us outline this method here. WKB approximation defines wave function in system with potential $V(r)$ as

$$\psi(r) = \frac{2}{\sqrt{p(r)}} \sin\left(\int_a^r p(r')\,\mathrm{d}r' + \frac{\pi}{4}\right), \tag{4.15}$$

where

$$p(r) = \sqrt{2m\left[E - V(r) - \frac{J(J+1)}{2mr^2}\right]}, \tag{4.16}$$

and a is classical turning point. If we compare it with asymptotic behavior of radial function

$$\psi(x \to \infty) \sim \sin\left(px - \frac{J\pi}{2} + \delta_J(p)\right), \tag{4.17}$$

where $p = \sqrt{2mE}$ we get equation for phase shift in WKB approximation

$$\delta_J(p) = \lim_{x\to\infty} \int_a^x [p(r') - p]\,\mathrm{d}r' - pa + \frac{(2J+1)\pi}{4}. \tag{4.18}$$

Charge transfer S-matrix element as well as cross section is depend only on difference of phase shift of ungerade and gerade system as mentioned above. This

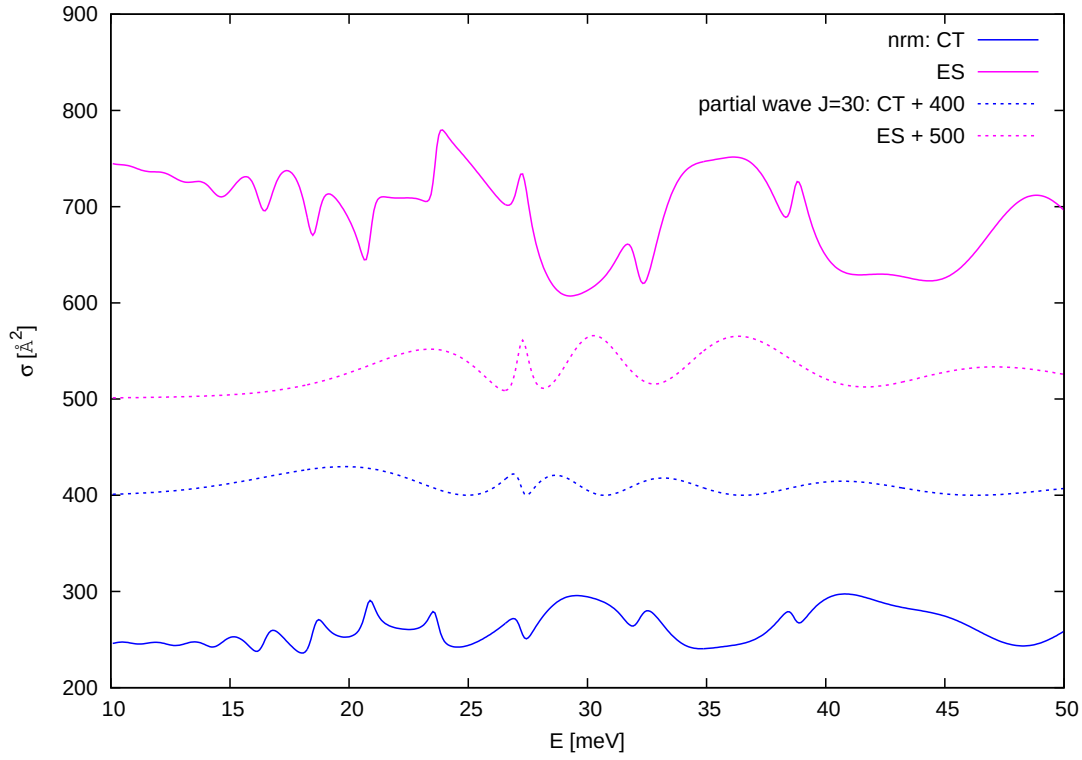

Figure 4.16: Detail of cross sections for charge transfer and elastic scattering for $H^- + D$. We can see the structures caused by resonances of $^2\Sigma_u^+$ initial state.

difference can be expressed as

$$\Delta\delta_J = \delta_J^{(g)} - \delta_J^{(u)} = \int_{a^{(g)}}^{\infty} \left[p^{(g)}(r') - p\right] \mathrm{d}r' - \int_{a^{(u)}}^{\infty} \left[p^{(u)}(r') - p\right] \mathrm{d}r', \qquad (4.19)$$

where $a^{(g)}$ and $a^{(u)}$ are classical turning points for gerade and ungerade symmetry respectively. The WKB approach can not give good description of the detachment process (like final-state distribution or spectra) but we saw, that the semi-classical methods give reasonable result of integral quantities like total detachment. We will see that it also gives good results for charge transfer and elastic scattering for higher collisional energies.

We used WKB formula for calculation of charge transfer and elastic scattering cross section with adiabatic (local) potentials with this simple model:

If it is classically allowed for particle to get over crossing of adiabatic potential curves for atom-ion system and for neutral molecule, we assume that the particle is absorbed to electron detachment channel and S-matrix will be zero. We used $R = 100\,\mathrm{au}$ as upper bound of integrals in WKB approximation and corrected phase shifts for partial waves to that of free particle there. This is important for cross section of elastic scattering, and has no relevance in charge transfer, where only difference between phase shifts is relevant.

We computed cross section for charge transfer and for elastic scattering for first 150 partial waves using non-local resonant model and compare it with the same number of partial waves in WKB approximation. We also add all contributing partial waves in this approximation. Comparison of the results can be seen in figure 4.15.

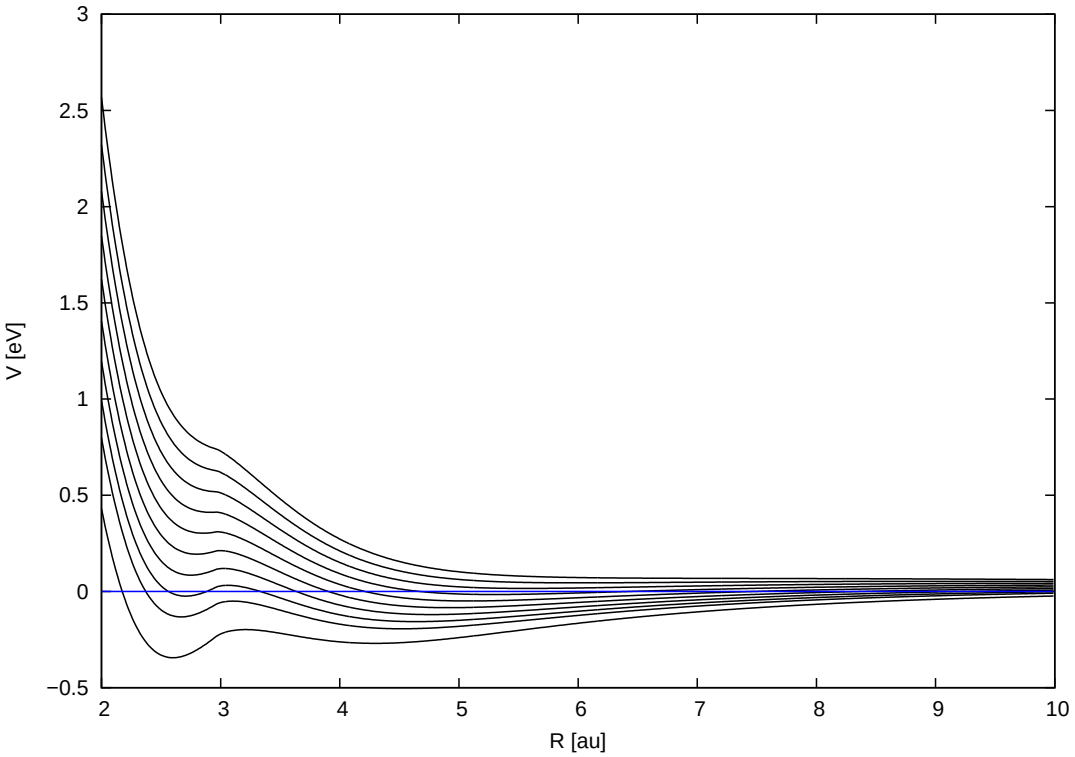

Figure 4.17: Effective potential $V(R) = V_d(R) + \frac{J^2+J}{2\mu R^2}$ for the $^2\Sigma_u^+$ state and partial waves $J = 25$ to 33 (from bottom to top). We indicated zero kinetic energy with blue line.

We can see good agreement of WKB approximation and non-local resonance model for higher energies. WKB approximation is not accurate for low energies, where only few lowest partial waves are involved. This is expected as WKB approximation is not that accurate there as well as the simple model of absorption of whole partial wave that can reach the autodetachment region. Large number of partial waves contributes to cross section for $E > 0.5\,\mathrm{eV}$. It would be very computationally demanding to converged results with the full non-local resonance model, but as we see in figure 4.15 that the WKB calculation limited to 150 partial waves is almost identical with full calculation for $E > 0.5\,\mathrm{eV}$. We therefore prolong the cross section with WKB calculation in this energy region.

At energies between 10 and 50 meV we can see structures caused by resonances in $^2\Sigma_u^+$ channel. The detail of this region can be seen on figure 4.16 together with one of the contributing partial waves ($J = 30$). We can see a narrow peak caused by the resonance in this partial wave around 27 meV. The other oscillations are from the Ramsauer-Townsend effect, as the phases shift of the background increases by more than 2π (see figure 4.19). Not that these resonances are closely related with long lived states of H^2_- reported in [73].

For H + D^- collision, these resonances can be found between 24 and 32 partial wave. This resonance behaviour can be explained by the shape of the effective potential for these partial waves (figure 4.17). We will look at these resonances in more detail. At the lower angular momentum, this resonances causing the increase in associative detachment as there is overlap with neutral potential. This can be illustratively seen on Argand diagram of elastic element

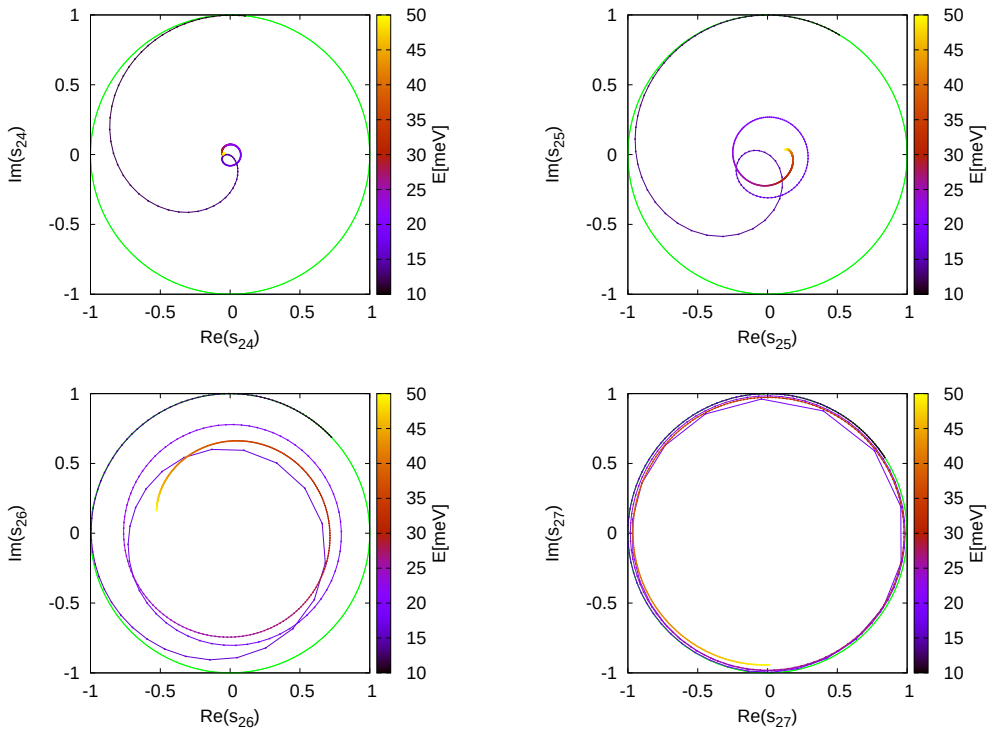

Figure 4.18: Argand diagrams for elastic element of S-matrix for different angular momenta. From top left to bottom right it is 24 to 27. We can see that the collision is more elastic with growing angular momenta and that the resonance growing wider.

of S-matrix for individual partial waves s_J. If the element of S-matrix lies on unit circle, there is no associative detachment. And as it approaches zero, the probability of associative detachment grows to one (as no other channel is open in this energy region). On figure 4.18 we can see the resonance region for partial wave 24, 25, 26 and 27. The resonance can be identified as a loop around the coordinate origin with much lower point density (as it is rapid change of phase shift). For greater angular momenta the associative detachment channel is closing and Argand diagram converges to the unit circle. The other variable we can obtain from S-matrix element for elastic process is the phase shift δ_l (shifted of hole number multiple of 2π). Resonances can be recognises as rapid change of phase shift by 2π radians. We present phase shifts for partial waves 27, 30, 32, 33 figure 4.19). We can see that there resonances are narrower for lower partial waves and that grows wider and less pronounced for larger angular momentum. For the last shown partial wave with angular momentum $J = 33$ the resonance disappeared entirely. We can see background that is responsible for the Ramsauer-Townsend effect as we mentioned earlier.

For experiments the reaction rates are important as we mentioned earlier. These can be expressed in terms of cross section as

$$k = \langle \sigma v \rangle_T = \sqrt{\frac{8}{\pi \mu (k_B T)^3}} \int \mathrm{d}E \sigma(E) E \exp\left(-\frac{E}{k_B T}\right), \tag{4.20}$$

where μ is reduced mass and k_B is Boltzmann constant and T it the temperature

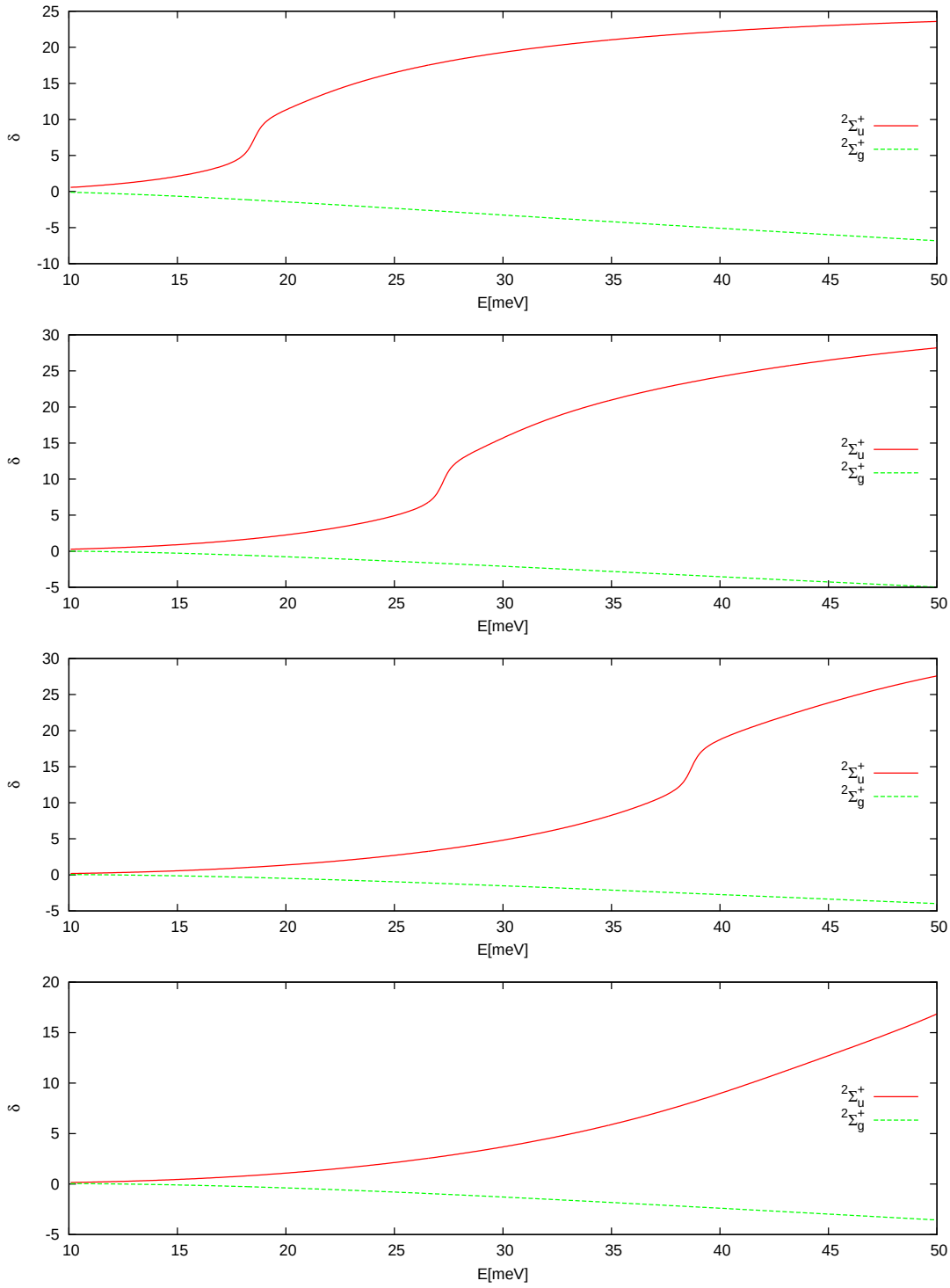

Figure 4.19: Dependence of phase shift on energy in the region with resonances and comparison of gerade and ungerade initial states phase shifts. We show angular momenta (from top) 27, 30, 32, 33.

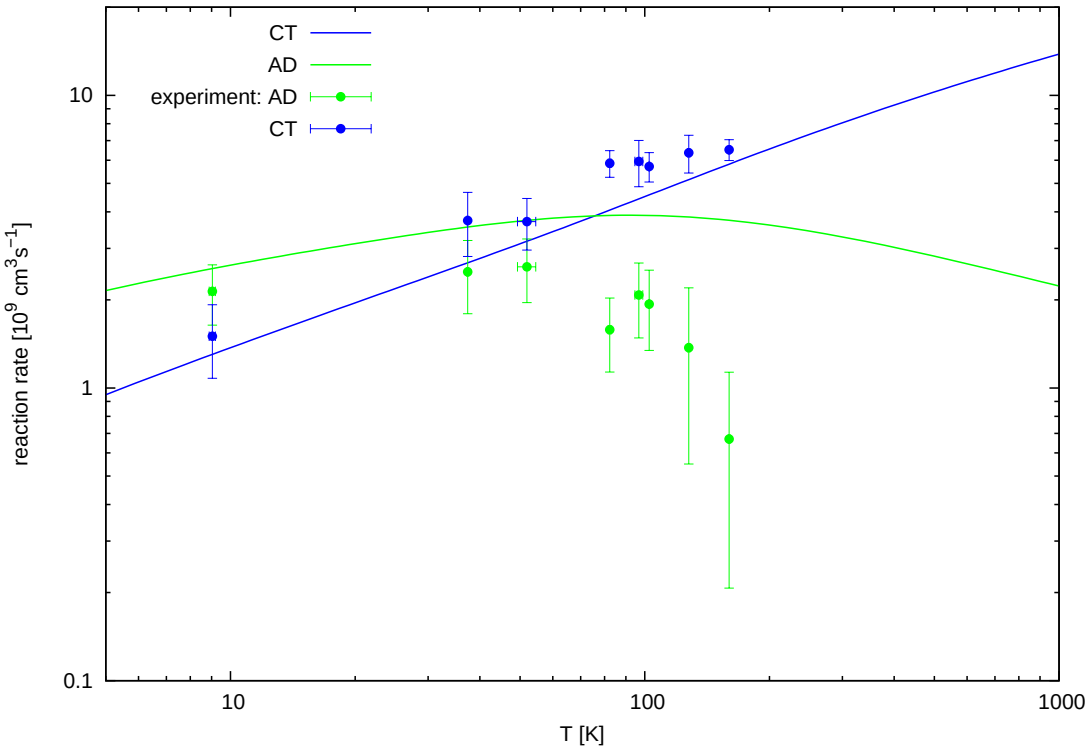

Figure 4.20: Temperature dependence of reaction rates for charge transfer $H + D^- \rightleftharpoons H^- + D$ compared with associative detachments $H + D^- \rightarrow HD + e^-$. We are also comparing these with experimental data measured by Roučka et al.[74].

of reactants. We calculated rates for charge transfer and associative detachment for temperatures from 5 to 1000 K and we are showing these on the figure 4.20 together with measured data from Roučka et al. [74].

In our calculation we totally ignore 0.4 meV difference between $H + D^-$ and $D + H^-$ channels. This difference goes beyond Born-Oppenheimer type approximation which we use. We expect that this will have small effect for energies $E \gtrsim 1\,\mathrm{meV}$.

5. Conclusions and future prospects

We have studied collisions of H + H^- and its isotopes. We calculated associative detachment cross section in low energy region, that corresponds to the temperatures from one to tens of thousand of Kelvins. This region is important for the astrophysics – plasma with temperature in this region is important in forming of the first protogalaxies and stars where the hydrogen and deuterium molecules are important coolants and thus our results can supply the associative detachment cross sections to the astrophysical models to get more realistic results. To get accurate cross section for $E \gtrsim 0.7\,\mathrm{eV}$ we had to add the cross sections for $^2\Sigma_g^+$ symmetry that has small but measurable (on the edge of measurability) contribution and we compare it with experiment. In addition to the associative detachment cross section, we show the total detachment cross section and the details about associative detachment like the partial cross section for individual rotation-vibrational states of the final molecules (see appendix A). We also presented the electronic spectra for a few selected energies that suggest, that the contribution from $^2\Sigma_g^+$ could be seen in the low electron energy end of the spectra. We analysed isotopic effect of these collisions and we found that the total detachment cross section is not dependent on the isotopic effect, but the redistribution of the states of neutral molecule depends on it, and so the associative detachment changes after opening the collision detachment channel. As we expected the associative detachment lowers with the increase of mass of isotopes, for which the collision is more adiabatic. The reaction rates of course change with the mass of the electron as they are dependent also on the velocity of the colliding particles and not only on the kinetic energy.

We have also calculated the charge transfer cross section and the rates and compared it with the preliminary experimental results close to energy region we are interested in. There are some interesting structures created by orbiting resonances in the region around 30 meV, but we do not know of any experiments that would be able to measure these.

The construction of our model is not ideal as we are using one dimensional data to fit two dimensional couplings. (These depend on the inter-nuclear distance as well as on the energy of the electron in the continuum.) This could be remedied by calculation of the couplings similarly as the Mündel, Berman and Domcke did for the $^2\Sigma_u^+$ state. We compared a few models and estimated the accuracy of total cross section of the final model to be about 10%. We never considered the complex phase of the coupling. We expect that the integral quantities like cross sections for charge transfer, total detachment or associative detachment are insensitive to this approximation, but the final state distribution and electronic spectra can be influenced.

As mentioned earlier, the measurement of electronic spectra would provide a new insight into the reactions in question. It is possible that the isotopic effects that we calculated would be observable in the electronic spectrum. The contribution of $^2\Sigma_g^+$ state would be better observable in electronic spectrum as well. Last but not least, these measurements would provide good test of the

constructed models.

In the future we may also include non-adiabatic corrections leading to 0.4 meV difference in the energies between H + D^- and D + H^- channels. This would improve charge transfer calculations as very low energies.

References

[1] Petr Čársk ý and Čurík Roman, editors. *Low-Energy Electron Scattering from Molecules, Biomolecules and Surfaces*. CRC Press, 2012.

[2] R. H. Doherty. Importance of associative detachment and dissociative attachment in the lower ionosphere as shown by LF radio measurements. *Journal of Geophysical Research*, 73(7):2429–2440, 1968.

[3] F.C. Fehsenfeld, A.L. Schmeltekopf, H.I. Schiff, and E.E. Ferguson. Laboratory measurements of negative ion reactions of atmospheric interest. *Planetary and Space Science*, 15(2):373 – 379, 1967.

[4] F. C. Fehsenfeld, D. L. Albritton, J. A. Burt, and H. I. Schiff. Associative-detachment reactions of O- and O2- by O2(1Δg). *Canadian Journal of Chemistry*, 47(10):1793–1795, 1969.

[5] F. J. Gordillo-Vázquez and A. Luque. Electrical conductivity in sprite streamer channels. *Geophysical Research Letters*, 37(16), 2010.

[6] A. Luque and F. J. Gordillo-Vázquez. Mesospheric electric breakdown and delayed sprite ignition caused by electron detachment. *Nature Geoscience*, 5:22–25, 2012.

[7] Torsten Neubert and Olivier Chanrion. On the electric breakdown field of the mesosphere and the influence of electron detachment. *Geophysical Research Letters*, 40(10):2373–2377, 2013.

[8] V. Vuitton, P. Lavvas, R.V. Yelle, M. Galand, A. Wellbrock, G.R. Lewis, A.J. Coates, and J.-E. Wahlund. Negative ion chemistry in titan's upper atmosphere. *Planetary and Space Science*, 57(13):1558 – 1572, 2009.

[9] J. H. Black, A. Porter, and A. Dalgarno. The emission spectrum of H2 from associative detachment and ultraviolet pumping. *Astrophysical Journal*, 249:138–144, 1981.

[10] Edward B. Jenkins and Antonio Peimbert. Molecular hydrogen in the direction of zeta orionis a. *The Astrophysical Journal*, 477(1):265, 1997.

[11] Cynthia Barckholtz, Theodore P. Snow, and Veronica M. Bierbaum. Reactions of C-n and CnH- with atomic and molecular hydrogen. *The Astrophysical Journal Letters*, 547(2):L171, 2001.

[12] Brian Eichelberger, Theodore P. Snow, Cynthia Barckholtz, and Veronica M. Bierbaum. Reactions of h, n, and o atoms with carbon chain anions of interstellar interest: An experimental study. *The Astrophysical Journal*, 667(2):1283, 2007.

[13] T. P. Snow, M. Stepanovic, N. B. Betts, B. R. Eichelberger, O. Martinez, and V. M. Bierbaum. Formation of Gas-Phase Glycine and Cyanoacetylene via Associative Detachment Reactions. *Astrobiology*, 9:1001–1005, 2009.

[14] Zhibo Yang, Brian Eichelberger, Marshall Y. Carpenter, Oscar Martinez Jr, Theodore P. Snow, and Veronica M. Bierbaum. Experimental and theoretical studies of reactions between H atoms and carbanions of interstellar relevance. *The Astrophysical Journal*, 723(2):1325, 2010.

[15] Zhibo Yang, Callie A Cole, Jr. Oscar Martinez, Marshall Y. Carpenter, Theodore P. Snow, and Veronica M. Bierbaum. Experimental and theoretical studies of reactions between H atoms and nitrogen-containing carbanions. *The Astrophysical Journal*, 739(1):19, 2011.

[16] S. C. Glover, D. W. Savin, and A.-K. Jappsen. Cosmological implications of the uncertainty in H– destruction rate coefficients. *The Astrophysical Journal*, 640(2):553, 2006.

[17] H. Kreckel, H. Bruhns, M. Čížek, S. C. O. Glover, K. A. Miller, X. Urbain, and D. W. Savin. Experimental results for H2 formation from H^- and H and implications for first star formation. *Science*, 329(5987):69–71, 2010.

[18] Carla M. Coppola, Savino Longo, Mario Capitelli, Francesco Palla, and Daniele Galli. Vibrational level population of H2 and H+ 2 in the early universe. *The Astrophysical Journal Supplement Series*, 193(1):7, 2011.

[19] Timothy S. Zwier, M. Matti Maricq, C. J. S. M. Simpson, Veronica M. Bierbaum, G. Barney Ellison, and S. R. Leone. Direct Detection of the Product Vibrational-State Distribution in the Associative Detachment Reaction Cl^-+H→HCl(v)+e^-. *Physical Review Letters*, 44:1050–1053, 1980.

[20] Timothy S. Zwier, James C. Weisshaar, and Stephen R. Leone. Nascent product vibrational state distributions of ion-molecule reactions: The H+F^-→HF(v)+e^- associative detachment reaction. *The Journal of Chemical Physics*, 75(10):4885–4892, 1981.

[21] Mark A. Smith and Stephen R. Leone. Product vibrational state distributions in thermal energy associative detachment reactions: F^-+H, D → HF(v), DF(v)+e^-. *The Journal of Chemical Physics*, 78(3):1325–1334, 1983.

[22] S. Živanov, M. Allan, M. Čížek, J. Horáček, F. A. U. Thiel, and H. Hotop. Effects of Interchannel Coupling in Associative Detachment: Electron Spectra for H+Cl^- and H+Br^- Collisions. *Physical Review Letters*, 89:073201, 2002.

[23] P. Jusko, Š. Roučka, R. Plašil, and J. Glosík. Determining the energy distribution of electrons produced in associative detachment: The electron spectrometer with multipole trap. *International Journal of Mass Spectrometry*, 352(0):19 – 28, 2013.

[24] J. Deiglmayr, A. Göritz, T. Best, M. Weidemüller, and R. Wester. Reactive collisions of trapped anions with ultracold atoms. *Physical Review A*, 86:043438, 2012.

[25] A. L. Schmeltekopf, F. C. Fehsenfeld, and E. E. Ferguson. Laboratory Measurement of the Rate Constant for $H^- + H \rightarrow H_2 + e^-$. *Astrophysical Journal Letters*, 148:L155, 1967.

[26] Oscar Martinez, Zhibo Yang, Nicholas B. Betts, Theodore P. Snow, and Veronica M. Bierbaum. Experimental determination of the rate constant for the associative detachment reaction $H^- + H \rightarrow H_2 + e^-$ at 300 K. *Astrophysical Journal*, 705(2):L172, 2009.

[27] M Čížek, J Horáček, and W Domcke. Nuclear dynamics of the H_2^- collision complex beyond the local approximation: associative detachment and dissociative attachment to rotationally and vibrationally excited molecules. *Journal of Physics B: Atomic, Molecular and Optical Physics*, 31(11):2571, 1998.

[28] H. Bruhns, H. Kreckel, K. A. Miller, X. Urbain, and D. W. Savin. Absolute energy-resolved measurements of the $H^-+H \rightarrow H_2+e^-$ associative detachment reaction using a merged-beam apparatus. *Physical Review A*, 82(4):042708, 2010.

[29] Dieter Gerlich, Pavol Jusko, Štěpán Roučka, Illia Zymak, Radek Plašil, and Juraj Glosík. Ion trap studies of $H^- + H \rightarrow H_2 + e$ - between 10 and 135 K. *The Astrophysical Journal*, 749(1):22, 2012.

[30] Joseph C. Y. Chen. Theory of atomic collisions with negative ions: Associative detachment. *Physical Review*, 156:12–25, 1967.

[31] Herman Feshbach. Unified theory of nuclear reactions. *Annals of Physics*, 5(4):357 – 390, 1958.

[32] A. Herzenberg. Electron-detachment in slow collisions between atoms and negative ions. *Physical Review*, 160:80–94, 1967.

[33] A. Dalgarno and J. C. Browne. The Associative Detachment of H and Hˆ-. *Astrophysical Journal*, 149:231, 1967.

[34] Joseph C. Y. Chen and Jerry L. Peacher. Interaction Potential between the Ground States of H and H^-. *Physical Review*, 167:30–38, 1968.

[35] Joseph C. Y. Chen and Jerry L. Peacher. Associative Detachment: $H+H^- \rightarrow H_2{}^*+e$. *Physical Review*, 168:56–63, 1968.

[36] W. Kołos and L. Wolniewicz. Potential-Energy Curves for the $X^1\Sigma^+{}_g$ $b^3\Sigma^+{}_u$ and $C^1\Pi_u$ States of the Hydrogen Molecule. *The Journal of Chemical Physics*, 43(7):2429–2441, 1965.

[37] Junya Mizuno and Joseph C. Y. Chen. Theoretical Investigation of Complex Potentials for Atomic Collisions. I. Numerical Solution of Model (H^-,H) Collisions. *Physical Review*, 187:167–192, 1969.

[38] R. J. Bieniek and A. Dalgarno. Associative detachment in collisions of H and H^-. *Astrophysical Journal*, 228:635–639, 1979.

[39] R J Beiniek. A source of errors in cross sections of curve-crossing processes. *Journal of Physics B: Atomic and Molecular Physics*, 13(22):4405, 1980.

[40] W. Domcke. Theory of resonance and threshold effects in electron-molecule collisions: The projection-operator approach. *Physics Reports*, 208(2):97 – 188, 1991.

[41] Claus Mündel, Michael Berman, and Wolfgang Domcke. Nuclear dynamics in resonant electron-molecule scattering beyond the local approximation - Vibrational excitation and dissociative attachment in H2 and D2. *Physical Review A*, 32:181–193, 1985.

[42] Michael Berman, Claus Mündel, and Wolfgang Domcke. Projection-operator calculations for molecular shape resonances: The ${}^2\Sigma^+{}_u$ resonance in electron-hydrogen scattering. *Physical Review A*, 31:641–651, 1985.

[43] J. Senekowitsch, P. Rosmus, W. Domcke, and H.-J. Werner. An accurate potential energy function of the H_2^- ion at large internuclear distances. *Chemical Physics Letters*, 111(3):211 – 214, 1984.

[44] K. Sakimoto. Ion-molecule reactions at extremely low energies: $H^-+H \rightarrow H_2+e$. *Chemical Physics Letters*, 164:294–298, 1989.

[45] J. M. Launay, M. Le Dourneuf, and C. J. Zeippen. The reversible H + H(-) yields H2(v, j) + e(-) reaction - A consistent description of the associative detachment and dissociative attachment processes using the resonant scattering theory. *Astronomy & Astrophysics*, 252:842–852, 1991.

[46] Ronald James Bieniek. Complex potential and electron spectrum in atomic collisions involving fast electronic transitions: Penning and associative ionization. *Physical Review A*, 18:392–413, 1978.

[47] M Čížek, J Horáček, F A U Thiel, and H Hotop. Associative detachment in low-energy collisions between hydrogen atoms and atomic halogen anions. *Journal of Physics B: Atomic, Molecular and Optical Physics*, 34(6):983, 2001.

[48] S Živanov, M Čížek, J Horáček, and M Allan. Electron spectra for associative detachment in low-energy collisions of Cl- and Br- with H and D. *Journal of Physics B: Atomic, Molecular and Optical Physics*, 36(16):3513, 2003.

[49] A Dalgarno and M R C McDowell. Charge transfer and the mobility of h - ions in atomic hydrogen. *Proceedings of the Physical Society. Section A*, 69(8):615, 1956.

[50] J N Bardsley. Electron detachment and charge transfer in H-H^- collisions. *Proceedings of the Physical Society*, 91(2):300, 1967.

[51] Swati Sinha and J. N. Bardsley. Symmetric charge transfer in low-energy ion-atom collisions. *Physical Review A*, 14:104–113, 1976.

[52] D. M. Davidović and R. K. Janev. Resonant charge exchange of the negative ions in slow collisions with atoms. *Physical Review A*, 186:89–95, 1969.

[53] M.I. Chibisov and R.K. Janev. Asymptotic exchange interactions in ion-atom systems. *Physics Reports*, 166(1):1 – 87, 1988.

[54] M. A. Huels, R. L. Champion, L. D. Doverspike, and Yicheng Wang. Charge transfer and electron detachment for collisions of H^- and D^- with H. *Physical Review A*, 41:4809–4815, 1990.

[55] K. A. Miller, H. Bruhns, J. Eliášek, M. Čížek, H. Kreckel, X. Urbain, and D. W. Savin. Associative detachment of $H^- + H \rightarrow H_2 + e^-$. *Physical Review A*, 84:052709, 2011.

[56] K. A. Miller, H. Bruhns, M. Čížek, J. Eliášek, R. Cabrera-Trujillo, H. Kreckel, A. P. O'Connor, X. Urbain, and D. W. Savin. Isotope effect for associative detachment: $H(D)^- + H(D) \rightarrow H_2(D_2)+e^-$. *Physical Review A*, 86:032714, 2012.

[57] J. Fedor, M. Cingel, J. D. Skalný, P. Scheier, T. D. Märk, M. Čížek, P. Kolorenč, and J. Horáček. Dissociative electron attachment to hbr: A temperature effect. *Physical Review A*, 75:022703, 2007.

[58] Martin Čížek. *Resonant processes in atomic collisions*. PhD disertation, Charles University in Prague, 1999.

[59] J. Horáček, F. Gemperle, and H.-D. Meyer. Calculation of dissociative attachment of electrons to diatomic molecules by the schwinger-lanczos approach. *The Journal of Chemical Physics*, 104(21):8433–8441, 1996.

[60] W Domcke and C Mundel. Calculation of cross sections for vibrational excitation and dissociative attachment in hcl and dcl beyond the local-complex-potential approximation. *Journal of Physics B: Atomic and Molecular Physics*, 18(22):4491, 1985.

[61] J Horáček. Extrapolation technique for solution of scattering integral equations. *Journal of Physics A: Mathematical and General*, 22(4):355, 1989.

[62] H.-D. Meyer, J. Horáček, and L. S. Cederbaum. Schwinger and anomaly-free kohn variational principles and a generalized lanczos algorithm for nonsymmetric operators. *Physical Review A*, 43:3587–3596, 1991.

[63] H.-D. Meyer and S. Pal. A band-lanczos method for computing matrix elements of a resolvent. *The Journal of Chemical Physics*, 91(10):6195–6204, 1989.

[64] Hinne Hettema, editor. *Quantum Chemistry: Classic Scientific Papers*. World Scientific Series in 20th Century Chemistry. World Scientific Pub Co Inc, 2000.

[65] I Paidarova and Ph Durand. private communication.

[66] Darian T Stibbe and Jonathan Tennyson. Electron-h_2 scattering resonances as a function of bond length. *Journal of Physics B: Atomic, Molecular and Optical Physics*, 31(4):815, 1998.

[67] A.K. Belyaev, A.S. Tiukanov, and W. Domcke. Generalized diatomics-in-molecule method applied to the anion. *Chemical Physics*, 325(2–3):378 – 388, 2006.

[68] Milton Abramowitz and Irene Stegun, editors. *Handbook of Mathematical Functions*. Dover Publications, 1964.

[69] J N Bardsley and J S Cohen. Variational calculations of resonant states of H_2^-. *Journal of Physics B: Atomic and Molecular Physics*, 11(21):3645, 1978.

[70] J. N. Bardsley and J. M. Wadehra. Dissociative attachment and vibrational excitation in low-energy collisions of electrons with H2 and D2. *Physical Review A*, 20:1398–1405, 1979.

[71] V A Esaulov. Electron detachment and charge exchange in H - scattering by atomic deuterium. *Journal of Physics B: Atomic and Molecular Physics*, 13(20):4039, 1980.

[72] Eugene P. Wigner. On the behavior of cross sections near thresholds. *Physical Review*, 73:1002–1009, 1948.

[73] Martin Čížek, Jiří Horáček, and Wolfgang Domcke. Long-lived anionic states of H_2 , HD, D_2 , and T_2. *Phys. Rev. A*, 75:012507, 2007.

[74] Štěpán Roučka. private communication.

Appendices

A. Description of detailed data attached on DVD

The attached DVD contains data from our calculation corresponding to the associative and total detachment. It is also available in electronic form as attachment data.zip. In directory (folder) data you can find files named like this:

`isotopes-minimal_energy_in_eV-maximal_energy_in_eV-symmetry.dat`

Here the symmetry is 'g' for the $^2\Sigma_g^+$ state and 'u' for the $^2\Sigma_u^+$ initial state. There are two ranges of energies – the first from 0.1 meV to 2 eV; this data are linear in logarithm scale and we present only data for $^2\Sigma_u^+$ initial state, as the other is mostly zero in this region. The second region is from 0.55 eV to 5.5(5.45) eV and the data are linear in this region. So for example if you want the data for H + H^- collision for energy between 0.55 and 5.5 eV for $^2\Sigma_g^+$ state you can find it in the file

`H_2-0.55-5.5-u.dat`

Files are in text format with six columns. The first is the initial kinetic energy of the reaction. The next is the angular momentum of partial wave (J). The difference between the angular momentum of neutral molecule and the angular momentum J follows. Next two are vibrational quantum number decreased by one and the energy of this state. Finally, we present the cross section we calculated for these parameters.

Hence the total detachment cross section can by obtained as sum over all cross section with the same energy. The associative detachment cross section is only sum over the vibrational state that has negative energy and thus are bound. The electronic spectrum can be obtained using the energy conservation law and the equation (4.3) and we can filter it according to the presented attributes to obtain the other presented data.

B. Publications

B.1 Phys. Rev. A 84, 052709

Associative detachment of $H^- + H \rightarrow H_2 + e^-$ K. A. Miller, H. Bruhns, J. Eliášek, M. Čížek, H. Kreckel, X. Urbain, and D. W. Savin
Phys. Rev. A **84**, 052709 - Published 11 November 2011

Associative detachment of $H^- + H \rightarrow H_2 + e^-$

K. A. Miller,[1] H. Bruhns,[1,*] J. Eliášek,[2] M. Čížek,[2] H. Kreckel,[1,†] X. Urbain,[3] and D. W. Savin[1]
[1]*Columbia Astrophysics Laboratory, Columbia University, New York, New York 10027, USA*
[2]*Institute of Theoretical Physics, Faculty of Mathematics and Physics, Charles University Prague, CZ-180 00 Praha 8, Czech Republic*
[3]*Institute of Condensed Matter and Nanosciences, Université Catholique de Louvain, B-1348 Louvain-la-Neuve, Belgium*
(Received 22 July 2011; published 11 November 2011)

Using a merged-beams apparatus, we have measured the associative detachment (AD) reaction of $H^- + H \rightarrow H_2 + e^-$ for relative collision energies up to $E_r \leqslant 4.83$ eV. These data extend above the 1-eV limit of our earlier results. We have also updated our previous theoretical work to account for AD via the repulsive $^2\Sigma_g^+$ H_2^- potential energy surface and for the effects at $E_r \geqslant 0.76$ eV on the experimental results due to the formation of long-lived H_2 resonances lying above the H + H separated atoms limit. Merging both experimental data sets, our results are in good agreement with our new theoretical calculations and confirm the prediction that this reaction essentially turns off for $E_r \gtrsim 2$ eV. Similar behavior has been predicted for the formation of protonium from collisions of antiprotons and hydrogen atoms.

DOI: 10.1103/PhysRevA.84.052709 PACS number(s): 34.50.Lf, 52.20.Hv, 95.30.Ft, 97.10.Bt

I. INTRODUCTION

One of the simplest molecular formation reactions is associative detachment (AD) via

$$H^- + H \rightarrow H_2 + e^-. \quad (1)$$

This reaction is of interest for fundamental atomic and molecular physics and also because it plays an important role in protogalactic and first star formation in the early universe [1–3]. Two groups have recently reported measurements of this reaction. Martinez *et al*. [4] measured the thermal rate coefficient at 300 K using a flowing afterglow technique. Our group has measured this reaction over a collision energy range from 4 meV to 1 eV using a merged-beams method [3,5,6]. Our results lie 2.2 ± 0.9 times above those of [4]. The quoted uncertainty represents the quadrature sum of the estimated total experimental 1σ confidence level for each measurement. We have also taken into account minor corrections to our earlier data, which are described below.

In [6] we hypothesized that this discrepancy is due to an error in the measured rate coefficient of [7] for

$$H + Cl^- \rightarrow HCl + e^-, \quad (2)$$

which [4] used to determine their neutral H number density and thereby normalize their results. Our apparatus is not configured to study reaction (2) and test this hypothesis, but we have been able to extend our measurements of reaction (1) to higher energies and thereby provide additional benchmarks for theory. We have also investigated and ruled out several possible sources of systematic errors in our previous experimental results. Additionally, we have more carefully considered the pressure dependence of our detection method. Last, we have updated our previous theoretical results of [3,8] to account for AD via the repulsive $^2\Sigma_g^+$ H_2^- state and for the effects at $E_r \geqslant 0.76$ eV on the experimental results due to the formation of long-lived H_2 resonances lying above the H + H separated atoms limit.

The rest of the paper is organized as follows: Sec. II describes the experimental method and the various modifications performed for this work. Section III discusses the experimental uncertainties. Our new theoretical calculations are briefly described in Sec. IV. In Sec. V we present our results and compare them to theory. A discussion of our results is given in Sec. VI and a short summary in Sec. VII.

II. EXPERIMENT

Here we briefly describe the experiment and the changes relevant to our new results. Further details about the apparatus and experimental method can be found in [3,5,6].

A. Method

We begin by extracting H^- from a duoplasmatron source and forming a beam with an energy of $E_{H^-} = -e(U_s + U_f/2)$. Here e is the unit charge, $U_s \approx -10$ kV is the nominal source voltage, and U_f is a small correction voltage, which is defined below. Using standard ion-optical elements, we shape, steer, and direct the beam into a photodetachment chamber that houses a floating cell biased to a potential U_f. The anion energy inside the floating cell is $E_{H^-} = -e(U_s + U_f/2) + eU_f$. Near the center of the floating cell, we cross the anions with an infrared laser and convert a portion of the H^- beam into a beam of ground-state H atoms of energy $E_H = -e(U_s - U_f/2)$. The resulting merged beams exit the floating cell, whereupon the H^- beam returns to its initial energy, while the H beam energy remains unchanged. The beam-beam interaction energy is controlled by varying U_f.

Shortly after leaving the photodetachment chamber, the two beams enter an interaction region of length L. Two beam profile monitors (BPMs) are used to determine the beam-beam overlap $\langle\Omega(z)\rangle$ within the interaction region, where the z axis is defined by the bulk velocity vectors of the copropagating beams. We also use the BPMs to verify the alignment of the

*Present address: Inficon GmbH, D-50968 Cologne, Germany.
†Present address: Department of Chemistry, University of Illinois, 600 South Mathews Avenue, Urbana, Illinois 61801, USA.

beam axes. The relative energy E_r between the beams depends, in part, on this alignment and is given by [9] as

$$E_r = \mu\left(\frac{E_{H^-}}{m_{H^-}} + \frac{E_H}{m_H} - 2\sqrt{\frac{E_{H^-}E_H}{m_{H^-}m_H}}\cos\theta\right). \quad (3)$$

Here $\mu = m_{H^-}m_H/(m_{H^-} + m_H)$ is the reduced mass of the colliding system, m_{H^-} and m_H are the masses of the H^- and H, respectively, and θ is the angle of intersection. E_r is controlled by varying U_f. This merged-beams approach allows us to reach collision energies on the order of a few meV, limited only by the alignment of the beams, the spread in collision angles between the two beams, and the energy spread of each beam. We used geometrical simulations [3,5,6] to determine the average collision energy $\langle E_r\rangle$ versus U_f, taking into account the spreads in beam energies and angles.

Both beams are chopped out of phase in order to extract the signal H_2 generated in the interaction region from various backgrounds. Any H_2 formed in the interaction region has an energy of $E_{H_2} = E_{H^-} + E_H = -2eU_s = 20$ keV, neglecting the $\lesssim$3.7 eV kinetic energy of the detached electron and the similarly small internal energy of the H_2 formed. At the end of this region, an electrostatic quadrupole deflector is used to direct the H^- into a Faraday cup where the current I_{H^-} is read and recorded. The parent H and daughter H_2 beams continue on into a gas cell kept at a helium pressure of 2×10^{-4} Torr for most measurements. Inside the cell a fraction of the H_2 is ionized by the stripping collisions forming $\approx$20 keV H_2^+. Additionally, stripping of the H beam and dissociative ionization of the H_2 can produce $\approx$10 keV H^+.

After the gas cell, the neutrals and resulting ions enter the analyzer region involving two double-focusing, electrostatic cylindrical deflectors in series [10] and a channel electron multiplier (CEM). A hole in the outer plate of the first or lower cylindrical deflector (LCD) allows neutrals to pass through and travel into a neutral detector. The neutral particle current I_H, as measured in amperes, is monitored by measuring the secondary negative particle emission from the target inside the neutral detector. The voltages on the LCD and upper cylindrical deflector (UCD) are selected to transmit the 20-keV H_2^+ signal ions into the CEM while rejecting any of the 10-keV H^+ formed in the gas cell.

We study reaction (1) from the number of H_2^+ ions detected in the CEM. Experimentally, we measure the cross section σ_{AD} times the relative velocity v_r between the H^- and H beams convolved with the velocity spread of the experiment. This gives the rate coefficient [6]

$$\langle\sigma_{AD}v_r\rangle = \frac{1}{\sigma_{st}N_{He}}\frac{S}{T_aT_g\eta}\frac{e^2}{I_{H^-}I_H}\frac{v_{H^-}v_H}{L\langle\Omega(z)\rangle}. \quad (4)$$

The left-hand-side average is over the experimental energy spread. On the right side, σ_{st} is the stripping cross section for H_2 on He forming H_2^+ [11], N_{He} is the gas cell helium column density, S is the background-subtracted, pressure-corrected H_2^+ signal, T_a is the transmittance of the combined LCD-UCD analyzer, T_g is the transmittance of the grid in front of the CEM, η is the CEM efficiency, and v_{H^-} and v_H are the velocities of the H^- and H beams, respectively.

B. Modifications

The present work uses a current meter with a fast response time, enabling us to directly measure the H^- current at each phase in the chopping pattern, which is on the millisecond scale, and monitor it throughout each data run. Thus we are able to measure the anion current when the laser is on, $I_{H^-}^{on}$, over the course of a data run. This is used for I_{H^-} in Eq. (4). We were also able to monitor the anion current with the laser off, $I_{H^-}^{off}$, and determine the attenuation factor

$$f = 1 - \frac{I_{H^-}^{on}}{I_{H^-}^{off}}, \quad (5)$$

which is needed to extract the background-corrected S [6]. This situation is to be contrasted with our previous results [3,6], where, due to equipment limitations, the H^- current was averaged over the H^- chopping cycle and the resulting $\langle I_{H^-}^{chop}\rangle$ was recorded using a slow current meter. As a result, for that work f was not measured during data collection but under simulated data collection conditions, and an average value was used. Additionally, this factor was used to extract $I_{H^-}^{on}$ and $I_{H^-}^{off}$ from $\langle I_{H^-}^{chop}\rangle$.

For the present work we are also using a new calibrated neutral detector in combination with a fast current amplifier to record the H particle current at each phase in the chopping pattern and to monitor it throughout each data run. This modification is described in [6]. Thus, during a data run, we are now able to directly measure I_H, which is needed in Eq. (4). In our previous work, the H particle current was also monitored with a fast current amplifier; however, the neutral detector was not designed for absolute measurements. So to analyze those results, using the new detector we measured the H particle current due to photodetachment (PD), I_H^{PD}, to determine the neutral-to-anion (nta) ratio

$$f_{nta} = \frac{I_H^{PD}}{I_{H^-}^{off}} \quad (6)$$

under simulated data collection conditions. This factor, combined with the extracted $I_{H^-}^{off}$ discussed above, was then used in [6] to determine I_H for Eq. (4).

We have also installed a BPM immediately before the neutral detector, at a distance of 2055 mm from the first BPM in the interaction region. Turning off the voltage of the LCD allows the H^- beam to pass through the hole in the outer plate of the LCD. We used this additional BPM to measure the position of both the H and H^- beams and verified the alignment of the beams over a much longer lever arm than was previously possible using only the two BPMs in the interaction region. We find that the full angle between the beam axes measured here is in good agreement with that reported in [6].

C. Pressure corrections

Any H_2^+ formed in the gas cell can be destroyed by subsequent collisions with He in either the gas cell or the analyzer region. The resulting products are not transmitted by the electrostatic deflectors into the CEM, thereby reducing the apparent signal and rate coefficient. This small systematic shift in our data was overlooked in our previous work [3,6]. Here

we quantified this minor correction for both our previous and present results.

We measured the H_2^+ attenuation using an approach similar to the one we used to determine the He gas cell column density in Refs. [3,6]. Reconfiguring the ion source to produce H_2^+ and the apparatus to transmit H_2^+ beams, we used the electrostatic quadrupole after the interaction region to direct the beam into a Faraday cup, where we measured the unattenuated H_2^+ current $I^o_{H_2^+}$. We then guided the beam through the gas cell and measured the transmitted current, $I^o_{H_2^+}$, on the outer plate of the UCD. With no He in the gas cell, the UCD reading was over 95% of that in the Faraday cup. The measured attenuated data were corrected for this slight difference in the unattenuated current readings.

The H_2^+ attenuation as a function of gas density is given by

$$\frac{I_{H_2^+}}{I^o_{H_2^+}} = \exp(-\sigma_d N_{He}), \tag{7}$$

where σ_d is the total H_2^+ destruction cross section and N_{He} is the helium column density. Following the methodology of [6], the column density can be expressed as

$$N_{He} = \int_{quad} n_{He}(l)dl + \int_{gas\,cell} n_{He}(l)dl + \int_{analyzer} n_{He}(l)dl. \tag{8}$$

Here $n_{He}(l)$ is the helium density, and dl is the infinitesimal path length. Using the same model as [6], we take the pressure to be constant in each of these regions and reexpress Eq. (8) as

$$N_{He} = n_1 l_1 + n_2 l_2 + n_3 l_3. \tag{9}$$

The He density in the quadrupole is n_1, and the path length $l_1 = 5.0 \pm 1.0$ cm. In the gas cell the He density is n_2, and the path length $l_2 = 78.7 \pm 1.0$ cm. The He density in the analyzer region is n_3, and the path length $l_3 = 35.4 \pm 1.0$ cm is the distance that the ions travel before striking the UCD. All uncertainties here and throughout the paper are given at an estimated 1σ statistical confidence level. The respective densities were calculated from the measured pressures using the ideal gas law at the laboratory temperature, which was stabilized at 293 K for both the work of [3,6] and our new results here. The ratio of the measured pressures in each section were $p_1/p_2 = 0.137 \pm 0.019$ and $p_3/p_2 = 0.105 \pm 0.034$. The uncertainties in these ratios are due to the manufacturer-quoted accuracies of the pressure gauges (10% for p_1 and p_2 and 30% for p_3).

Attenuation data were collected for pressures up to $\approx 4.5 \times 10^{-4}$ Torr and are shown in Fig. 1. From a fit to these data we extracted a cross section of $(2.75 \pm 0.29) \times 10^{-16}$ cm^2 at an energy of 10 keV amu^{-1}. This estimated uncertainty is due to the error in the attenuated and unattenuated current readings (3% each) and the uncertainty in the He column density (10%). The error in this latter quantity was estimated by adding the uncertainties from each segment $n_i l_i$ of the total column density. The errors in the path lengths and gas densities (i.e., pressures) have been given above.

Collisional destruction of H_2^+ has also been studied by Suzuki *et al.* [12], who reported cross sections of various outgoing channels for ion energies from 2 to 8 keV amu^{-1}.

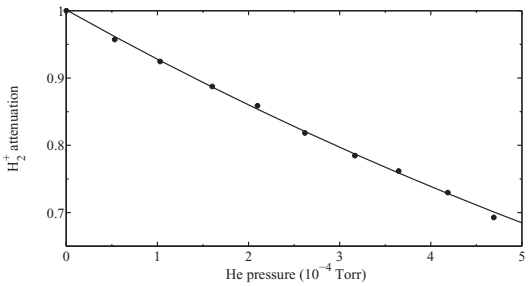

FIG. 1. Attenuation of the H_2^+ ion beam as a function of helium gas cell pressure. The circles represent the statistically weighted mean from three sets of measurements. The error bars are smaller than the plotted circles. The line shows the best exponential fit.

We have derived a total destruction cross section by summing the relevant channels in [12]. Those results, shown in Fig. 2, indicate that the cross section is essentially constant between 2 and 8 keV amu^{-1}. Our result at 10 keV amu^{-1}, also shown in Fig. 2, is in good agreement with this trend.

To determine the expected signal attenuation factor and correct for the H_2^+ signal loss we use our measured H_2^+ destruction cross section combined with Eq. (7). The appropriate He column density is given by

$$N'_{He} = \tfrac{1}{2} n_2 l_2 + n_3 l'_3, \tag{10}$$

where the factor of $1/2$ takes into account that on average the H_2^+ ions will be formed in the center of the gas cell and $l'_3 = 57.9 \pm 1.0$ cm is the distance from the end of the gas cell to the CEM mouth. Using these values, we calculate from Eq. (7) that the signal attenuation with 2×10^{-4} Torr He in the gas cell is 0.92 ± 0.01. The signal must be divided by this factor to correct for the attenuation. This corresponds to an $(8.6 \pm 1.2)\%$ upward shift in the data. The uncertainty in this correction is estimated by propagating through Eq. (7) the quadrature sum of the uncertainties from both N'_{He} in Eq. (10) and σ_d.

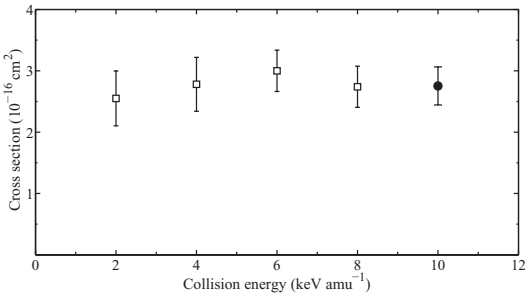

FIG. 2. Experimental cross sections for total H_2^+ destruction vs ion beam energy for $H_2^+ + He$. The open squares are the results of [12], while the circle represents our measurement. The error bars for each data set give the total 1σ experimental uncertainty.

TABLE I. Summary of systematic uncertainties at an estimated 1σ confidence level. Uncertainties are treated as random sign errors and added in quadrature.

Source	Error (%)
Background subtraction	5
Anion current	3
Neutral current	10
Beam overlap	3
Total relative errors from above	12
Stripping cross section	16
Effects of unknown rovibrational population	10
Analyzer transmittance	1
Grid transmittance	1
CEM detection efficiency	2
Overlap length	1
Helium gas cell column density	7
H_2^+ Attenuation	1
Total systematic uncertainty	24

III. UNCERTAINTIES

The various systematic uncertainties for the measurement are given in Table I. Values are listed at an estimated 1σ statistical confidence level. We have grouped them into two sets. The errors listed in the top third of Table I add in quadrature to $\pm 12\%$ for each data point. This represents the relative uncertainty between our old and new data sets and also at different energies within each set. Adding this in quadrature with the remaining uncertainties in the bottom two-thirds of Table I yields the total systematic error of $\pm 24\%$. A detailed discussion is given in [3,6] for the various uncertainties not already discussed here.

IV. THEORY

A. Earlier calculations

In our previous work, the AD cross section was calculated using nonlocal resonance theory and considering only the coupling of the $H + H^-$ and $H_2 + e^-$ channels through the lowest metastable H_2^- state of $^2\Sigma_u^+$ symmetry (see [3,8] for details). This state is one of two connected to the $H + H^-$ asymptote (not counting the spin degeneracy). Potential energy curves for both states are shown in Fig. 3. The second state of $^2\Sigma_g^+$ symmetry is repulsive and is usually neglected in the calculations. The validity of this approximation is supported by the very good agreement between our experimental results [3,6] and our nonlocal calculations [3,8] below 1 eV, even after the $\sim 9\%$ pressure correction of the H_2^+ signal described in Sec. II C, which was not accounted for in [3,6].

B. New calculations

We have extended our experimental results to ~ 5 eV, entering a regime where AD via the $^2\Sigma_g^+$ state becomes possible. Figure 3 shows that for sufficiently large energies the colliding $H + H^-$ can penetrate into the autodetachment region along the repulsive $^2\Sigma_g^+$ state. This region is defined as the range of internuclear separations R where an electron can

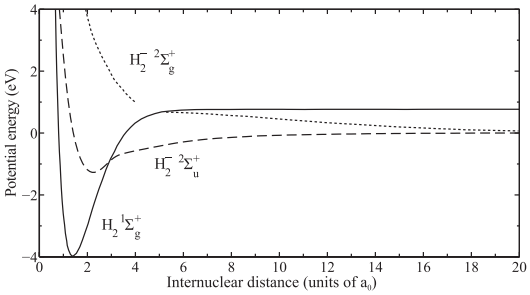

FIG. 3. H_2^- and H_2 potential curves vs internuclear distance in units of the Bohr radius a_0. The H_2^- attractive $^2\Sigma_u^+$ electronic state is given by the dashed curve [13], and the repulsive $^2\Sigma_g^+$ electronic state is given by the dotted curve constructed using the data of [14,15] below $\sim 4a_0$ and those of [16] above $\sim 5a_0$. The separated atoms limit (SAL) for these two potential energy curves is $H^-(^1S) + H(^2S)$. The solid curve shows the $H_2\ ^1\Sigma_g^+$ electronic state from [17] with a SAL of $H(^2S) + H(^2S)$. The energy difference between the two limits is determined by the H electron affinity energy $E_{EA} = 0.76$ eV [18].

escape the anionic system, i.e., the potential energy curves of the H_2^- system are above those for neutral H_2. This occurs for the $^2\Sigma_g^+$ state at $R < 5a_0$, where a_0 is the Bohr radius. Particles colliding along this state can penetrate into the autodetachment region for energies $\gtrsim 0.75$ eV motivating calculations for AD via this state.

Due to the different symmetry of the molecular orbitals, the $^2\Sigma_u^+$ and $^2\Sigma_g^+$ contributions to the AD cross section can be calculated separately. Thus we need only carry out new calculations for the $^2\Sigma_g^+$ state. A brief description of our approach is presented below, using atomic units. A more detailed discussion will be given in a future presentation.

Nonlocal resonance theory is explained in detail by [19]. The main idea is as follows. The electronic state ϕ_d, describing the colliding partners in the $H + H^-$ channel, is diabatically prolonged to small R. It is also assumed to be coupled to the $H_2 + e^-$ electronic continuum states ϕ_k through the matrix element

$$V_{dk}(R) = \langle \phi_d | H_{el} | \phi_k \rangle,$$

where H_{el} is the electronic Hamiltonian. The nonlocal resonance model is parametrized by three functions: $V_0(R)$, $V_d(R)$, and $V_{dk}(R)$. The potential energy curves for the neutral molecule $V_0(R)$ and for the anion $V_d(R)$ are functions only of R. The coupling element $V_{dk}(R)$, however, depends on both R and the momentum of the detached electron k.

Once $V_0(R)$, $V_d(R)$, and $V_{dk}(R)$ are known, the electronic dynamics of the system is fully parametrized, and the nuclear dynamics can be treated as a motion in the nonlocal energy-dependent effective potential:

$$V_d(R) + \int V_{dk}\left[E - \tfrac{1}{2}k^2 - T_N - V_0(R) + i\varepsilon\right]^{-1} V_{dk}^* k\, dk\, d\Omega_k.$$

T_N is the kinetic energy operator for the nuclei, $d\Omega_k$ is the differential solid angle for the outgoing electron, and ε is the usual positive infinitesimal of scattering theory. We solve the nuclear dynamics and calculate the cross sections using the method of [8].

In order to include ϕ_d for the $^2\Sigma_g^+$ state, we have to fix the parameters of the nonlocal resonance model for this state. The proper procedure for calculating these parameters involves extracting the discrete state ϕ_d from the continuum ϕ_k, employing the projection-operator technique. This procedure was followed in [20] for the $^2\Sigma_u^+$ state, and we used it as an input for our calculation [8]. But it is also possible to fix the model parameters by fitting the fixed-nuclei scattering data. We follow this latter procedure here.

To fix the coupling amplitude, we assume the separable form $V_{dk}(R) = g(R)f(k)$, where the k dependence is determined by the Wigner threshold law [21] with an exponential cutoff:

$$f(k) \sim k^{2l+1} e^{-\alpha k^2}, \tag{11}$$

where α is the cutoff parameter. The angular momentum l value in Eq. (11) is given by the lowest electron partial wave allowed by symmetry (discussed below). The R dependence is determined from the calculated local decay widths $\Gamma(R)$ of [14]. The potential energy curve for the anion $V_d(R)$ is constructed from [14,15] and extended to larger R using the data of [16]. The data for the potential near the crossing of the neutral and anion potential energy curves are missing. Nevertheless, the analytic behavior near the crossing has been discussed in detail by [19]. With this knowledge, the potential energy curve can be interpolated through the crossing as has been done before for hydrogen halides [22]. The actual shape of the $V_d(R)$ and $V_0(R)$ crossing is modified by the interaction of the electron scattering continuum with the threshold behavior given by Eq. (11). V_0 is from [17].

The decay of the odd-symmetry anion $^2\Sigma_u^+$ state to the even neutral $^1\Sigma_g^+$ state is possible only through release of an electron with odd angular momentum. In [3,8] we considered only $l = 1$ (p-wave scattering) since the calculations of [23] show that the next allowed $l = 3$ contribution is suppressed by almost two orders of magnitude for the energy range of interest. For the anion $^2\Sigma_g^+$ state decaying to the neutral $^1\Sigma_g^+$ state, the symmetry remains unchanged, requiring release of an electron with even angular momentum. Here we considered only $l = 0$ (s-wave scattering). In each case, as Eq. (11) shows, V_{dk} is strongly suppressed for higher angular momenta at the $k < 1$ values in our experimental results.

The anion $^2\Sigma_g^+$ state can also decay to the first excited $^3\Sigma_u^+$ state of H_2. These states are both repulsive and lie very close together. This decay, however, requires an odd value for l. With $l = 1$ and $k < 1$, $f(k)$, and hence V_{dk}, is strongly suppressed compared to the $^2\Sigma_g^+$ to $^1\Sigma_g^+$ decay channel with $l = 0$. The effect from the transition between repulsive states is thus expected to be small at low energies and was not included here.

Once the model parameters are fixed, σ_{AD} can be calculated using the methods described in [8]. Figure 4 shows our results. As expected from the previous good agreement of our experimental and theoretical results, the new contribution is small and notable only for $E_r \gtrsim 0.75$ eV. This is the threshold where the colliding particles overcome the barrier in the repulsive interaction potential and penetrate into the autodetachment region.

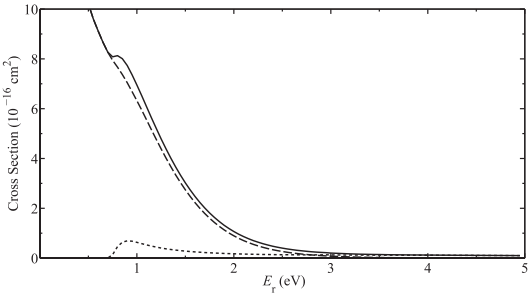

FIG. 4. Theoretical cross section for $H^- + H \rightarrow H_2 + e^-$ as a function of the relative collision energy E_r. The dashed curve shows the results via the attractive H_2^- $^2\Sigma_u^+$ state, the dotted curve shows the repulsive H_2^- $^2\Sigma_g^+$ state, and the solid curve shows the sum of the two.

Both the $^2\Sigma_u^+$ and $^2\Sigma_g^+$ contributions decay rapidly to zero for energies above ~1 eV. This is due to the competing process of collisional detachment,

$$H^- + H \rightarrow H + H + e^-, \tag{12}$$

which opens up for $E_r = 0.76$ eV and wins at higher energies. This is discussed in Sec. VI from the point of view of general energy-conservation arguments.

C. Contributions from quasibound H_2 states

At high angular momentum ($J > 10$), the colliding H^- and H systems can autodetach into quasibound H_2. These states, sometimes referred to as orbiting or shape resonances, lie above the separated-atoms limit for $H + H$. Such high J levels, temporarily stabilized by the centrifugal barrier, will eventually dissociate spontaneously and are therefore generally not considered in AD cross-section calculations. However, the lifetime for all but a few of these resonances well exceeds the flight time from the interaction region to the gas cell, and so most are expected to contribute to the experimental signal.

The H_2 flight time from the interaction region to the gas cell is (737 ± 640) ns. The mean is the center-to-center distance, the upper limit is from the start of the interaction region to the end of the gas cell, and the lower limit is from the end of the interaction region to the start of the gas cell. Quasibound H_2 (i.e., in high J levels) can strip in the He gas cell and will form H_2^+ in similarly high J levels. As the H_2^+ potential supports stable rovibrational levels up to $J = 35$, we assume that any such H_2^+ formed will be stable and will reach the detector.

In order to compare to our measured results, we have added the contribution of these quasibound H_2 states to our calculations for AD via the $^2\Sigma_u^+$ state. So as to mimic the range of experimental lifetimes, we have investigated the effect of cutting out states with lifetimes less than 100, 700, and 1400 ns and found no significant differences. In the end we included contributions from all resonances with lifetimes longer than 700 ns. The contribution of these states is of comparable size to the $^2\Sigma_g^+$ state contribution. The effect of these resonances for AD via the $^2\Sigma_g^+$ state has not been considered as that would

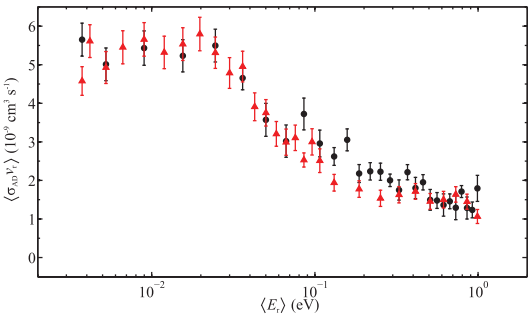

FIG. 5. (Color) Experimental rate coefficient $\langle \sigma_{AD} v_r \rangle$ as a function of the collision energy $\langle E_r \rangle$. The black circles show our new results, and the red triangles show our previous results from [3,6] corrected for the H_2^+ attenuation. Although our new results extend up to $\langle E_r \rangle \leqslant 4.83$ eV, here we show only up to the maximum $\langle E_r \rangle$ of our previous results for comparison. The error bars show the 1σ statistical uncertainties. There is an additional $\pm 12\%$ relative systematic error on each data point that is not shown.

be a small correction to an already small contribution. Last, we note that the significance of these resonances for molecular hydrogen formation in plasma environments will depend on whether the states can relax to stable states of H_2 before they dissociate by tunneling.

V. RESULTS

Relative energies E_r are controlled by varying the potential of the floating cell U_f. In [3,6] data were collected for $E_r \leqslant 1$ eV ($|U_f| \leqslant 281$ V). Here we have extended the energy range to $E_r \leqslant 4.83$ eV ($|U_f| \leqslant 621$ V). Data are collected by stepping U_f in voltage. The present work uses voltage ranges smaller than our earlier measurements. For $|U_f| \leqslant 441$ V, U_f was scanned across 60 V ranges in 10 V steps, and for $|U_f| \geqslant 441$ V the scanning was across 120 V ranges in 20 V steps.

Our measured rate coefficients for reaction (1) are plotted in Fig. 5 as a function of average collision energy $\langle E_r \rangle \leqslant 1.0$ eV. The black circles represent our new results, and the red triangles represent our previous work. Both have been corrected for the attenuation of the H_2^+ ions. The error bars on each data point display the 1σ statistical uncertainty. There is an additional $\pm 12\%$ relative systematic error on each data point that is not shown. The good agreement between our new and previous results indicates that there were no hidden systematic errors due to our previous inability to measure and monitor f and f_{nta} during data acquisition.

A final potential source of systematic error that we investigated was to verify the linearity of the gas-stripping method used to convert the product H_2 molecules into the measured H_2^+ signal. Here we measured the AD rate coefficient as a function of helium gas cell pressure for $(1-3) \times 10^{-4}$ Torr. Table II the results of these AD measurements at $\langle E_r \rangle = 16$ meV versus pressure. Taking into account the attenuation of the H_2^+ signal ions, to within the uncertainties the data show no dependence on gas cell pressure.

Given the good agreement between our results in [3,6] and our new data, we have merged them together using a statistically weighted averaging method. We also included our pressure-test results in this average. The 1σ counting statistics of each data point were used for the weighting. All data sets were also measured on the same relative energy grid. Figures 6 and 7 present the averaged data for $\langle E_r \rangle \leqslant 1$ eV plus the new data we have collected for 1.0 eV $\leqslant \langle E_r \rangle \leqslant 4.83$ eV. Also shown are the cross-section calculations of [3,8], supplemented by our new theoretical work here, multiplied by v_r, and convolved with the experimental energy spread. Figure 7 shows the theoretical results with and without the effects of the H_2 orbiting resonances included. As is clear from Figs. 6 and 7, we find good agreement with theory throughout the measured energy range. The contribution due to orbiting resonances of H_2 can also be seen in Fig. 7, as the experimental data are shifted to slightly higher energy compared to the calculations which do not include these resonances.

VI. DISCUSSION

The good agreement that we find here both with our previous results and with our updated theory strengthens our confidence that theory and experiment have finally converged for reaction (1). Including AD via the repulsive $^2\Sigma_g^+$ state increases the cross section by an amount smaller than we are currently able to measure experimentally. The resulting theoretical thermal rate coefficient is only 1.3% larger than that for only the attractive state at temperatures of 4000 K, 3.5% at 8000 K, and 4.4% larger at 10 000 K. These are significantly smaller than the ≈25% experimental accuracy with which we have been able to benchmark theory. Hence, we continue to recommend the thermal rate coefficient of [3] for modeling plasma temperatures below 10^4 K.

Additionally, our results continue to imply that the reason for the discrepancy seen with the results of [4] lies in the data of [7] used for normalization. This is further supported by the theoretical AD work on hydrogen halides of [24]. They used the same theoretical approach as we do here and found systematically higher AD rate coefficients than the

TABLE II. Rate coefficient results at $\langle E_r \rangle = 16$ meV versus helium gas cell pressure. Our theoretical results are also shown for comparison.

Pressure (10^{-4} Torr)	Rate Coefficient (10^{-9} cm^3 s^{-1})		
	Value	Statistical uncertainty	Relative uncertainty
1.0	5.6	±0.5	±0.7
2.0	5.2	±0.4	±0.6
3.0	5.2	±0.4	±0.6
Theory	5.0		

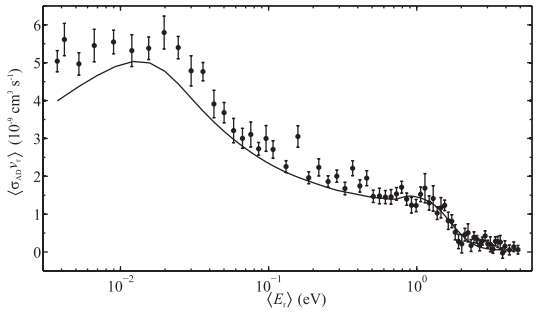

FIG. 6. The circles show the statistically weighted mean of the experimental rate coefficients $\langle \sigma_{AD} v_r \rangle$ from our previous [3,6] and current work as a function of the collision energy $\langle E_r \rangle$ (see text). For $\langle E_r \rangle \geqslant 1.0$ eV the data are solely from the current measurement. The error bars represent the 1σ statistical uncertainties. The solid line is from the cross-section calculations of [3,8], supplemented by our new theoretical work here, multiplied by v_r, and convolved with our experimental energy spread. The effects of the H_2 orbiting resonances have been included in the calculations shown here.

experimental work of [7]. It appears to us that a remeasurement of reaction (2) using a technique different from that of [7] is clearly called for to resolve this dilemma.

Our results also verify the predictions of [8] and our new theoretical work here that the AD cross section for reaction (1) should decrease to essentially insignificant values for $E_r \gtrsim 2$ eV, as shown in Fig. 6. A simplified adiabatic description of the AD reaction can provide good insight into the physics behind this prediction. We consider here only the $^2\Sigma_u^+$ symmetry. Similar arguments can also be given for the $^2\Sigma_g^+$ state.

Initially, the H^- and H approach one another along the attractive $^2\Sigma_u^+$ electronic state. This state crosses into the autodetachment region at $R \sim 3a_0$. Adiabatic theory dictates that the system remains electronically in the ground state. Inside the autodetachment region the ground state is the $^1\Sigma_g^+$ state of neutral H_2 plus a free electron with zero kinetic energy. Conservation of energy requires that the final state energy equals that initially available

$$E_v = E_r + D_0 - E_{EA}. \tag{13}$$

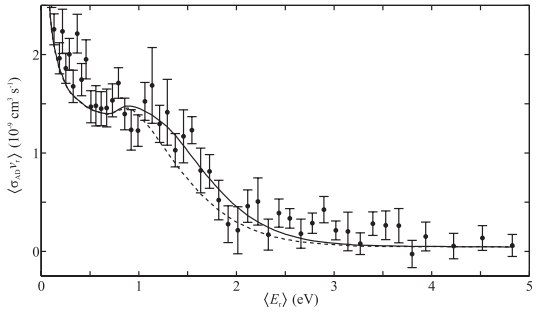

FIG. 7. Same as Fig. 6, but on a linear scale. The dotted curve shows the calculations without the effects of the H_2 orbiting resonances included.

Here E_v is the excitation energy of the vibrational level v formed in the process, D_0 is the 4.48-eV dissociation energy gained by formation of H_2 in the $v = 0$ vibrational and $J = 0$ rotational level [25], and $E_{EA} = 0.76$ eV is the electron affinity required to neutralize the H^- and form H [18]. For $E_r > E_{EA}$, the system lies in the dissociation continuum ($E_v > D_0$), resulting in the formation of $H + H + e^-$ and not $H_2 + e^-$.

In reality the AD process is not exactly adiabatic. This is manifested by the release of an electron with a nonzero kinetic energy E_e, and we can rewrite (13) as

$$E_v + E_e = E_r + D_0 - E_{EA}. \tag{14}$$

The nonadiabatic exchange of energy between the electron and protons is weak though; detached electrons do not have a large kinetic energy. Our full calculations for the $^2\Sigma_u^+$ state [8] show that only a negligible amount of electrons can have energy above ~1.5 eV. Taking into account that the largest possible value of E_r will occur for $E_v = D_0$, this leads to the prediction that the AD process will cease for $E_r \gtrsim E_{EA} + 1.5$ eV. For reaction (1), this corresponds to $E_r \gtrsim 2.26$ eV. A similar argument has been suggested for the decrease in the cross section for protonium formation in collisions of antiprotons with hydrogen atoms (see [26] for a review). Note that we have ignored the insignificant kinetic energy of the final H_2 molecule E_{H_2}, as conservation of momentum gives $E_{H_2} = (m_e/m_{H_2})E_e \ll E_e$.

Continuing the protonium analogy, one would expect a sharp decrease in σ_{AD} immediately after the collisional detachment threshold at $E_r = 0.76$ eV. In the $H^- + H$ collision, the drop in the cross section occurs at higher energies. This is related to the threshold law given by Eq. (11) with $l = 1$ for the dominant ungerade channel. As a result, the coupling V_{dk} vanishes for zero detached electron energy and rises smoothly as the energy increases. The electron energy in Eq. (14) thus cannot be exactly zero, but remains relatively small. The smooth decrease in σ_{AD} above 1 eV, confirmed by the present experiment, thus provides a good test of the theoretical description of the electron release amplitude.

Last, the decrease of the AD cross section is indeed slightly weakened by positive contributions of the $^2\Sigma_g^+$ state, as shown in Fig. 4, and orbiting resonances, as seen in Fig. 7. However, the decreasing trend above 1 eV, controlled by V_{dk}, is still dominant (e.g., Fig. 6).

VII. SUMMARY

We have modified the experimental methods used in [3,5,6] to measure reaction (1) up to $E_r \leqslant 4.83$ eV. Additionally, we have performed several modifications to better control potential systematic errors. We find good agreement between our previous and new data sets. To within the experimental uncertainties, we also continue to find good agreement with the calculations of [3,8], which have been extended here to include contributions from the repulsive $^2\Sigma_g^+$ H_2^- state and for the effects on the experimental results due to orbiting resonances of H_2 for $E_r \geqslant 0.76$ eV. In particular, we confirm the predictions of [8] that this reaction turns off for $E_r \gtrsim 2$ eV. Similar behavior has been predicted for the formation of protonium from collisions of antiprotons and hydrogen atoms [26].

ACKNOWLEDGMENTS

The authors thank M. Lestinsky and S. A. Marino for stimulating discussions and D. Thomas for technical assistance. This work was supported in part by NSF Grant Nos. CHE-0520660, AST-0606960, AST-0807436, and AST-0905832. H. Bruhns was supported in part by the German academic exchange service DAAD. M. Čížek and J. Eliášek were supported in part by Grant No. GACR 208/10/1281 from the Czech Republic. X. Urbain acknowledges support from the Fund for Scientific Research (FNRS).

[1] S. C. Glover, D. W. Savin, and A.-K. Jappsen, Astrophys. J. **640**, 2 (2006).
[2] S. C. O. Glover and T. Abel, Mon. Not. R. Astron. Soc. **388**, 4 (2008).
[3] H. Kreckel, H. Bruhns, M. Čížek, S. C. O. Glover, K. A. Miller, X. Urbain, and D. W. Savin, Science **329**, 69 (2010).
[4] O. Martinez Jr., Z. Yang, N. B. Bettes, T. P. Snow, and V. M. Bierbaum, Astrophys. J. **705**, L172 (2009).
[5] H. Bruhns *et al.*, Rev. Sci. Instrum. **81**, 013112 (2010).
[6] H. Bruhns, H. Kreckel, K. A. Miller, X. Urbain, and D. W. Savin, Phys. Rev. A **82**, 042708 (2010).
[7] C. J. Howard, F. C. Fehsenfeld, and M. McFarland, J. Chem. Phys. **60**, 5086 (1974).
[8] M. Čížek, J. Horáček, and W. Domcke, J. Phys. B **31**, 2571 (1998).
[9] R. A. Phaneuf, C. C. Havener, G. H. Dunn, and A. Müller, Rep. Prog. Phys. **62**, 1143 (1999).
[10] H. Kreckel, H. Bruhns, K. A. Miller, E. Wåhlin, A. Davis, S. Höckh, and D. W. Savin, Rev. Sci. Instrum. **81**, 063304 (2010).
[11] R. Browning, C. J. Latimer, and H. B. Gilbody, J. Phys. B **3**, 667 (1970).
[12] Y. Suzuki, T. Kaneko, M. Tomita, and M. Sakisaka, Phys. Soc. Jpn. **55**, 3037 (1986).
[13] J. Senekowitsch, P. Rosmus, W. Domcke, and H.-J. Werner, Chem. Phys. Lett. **111**, 211 (1984).
[14] D. T. Stibbe and J. Tennyson, J. Phys. B **31**, 815 (1998).
[15] D. T. Stibbe and J. Tennyson, Chem. Phys. Lett. **308**, 532 (1999).
[16] J. N. Bardsley and J. M. Wadehra, Phys. Rev. A **20**, 1398 (1979).
[17] L. Wolniewicz, J. Chem. Phys. **103**, 1792 (1995).
[18] J. Horáček, M. Čížek, K. Houfek, P. Kolorenč, and W. Domcke, Phys. Rev. A **70**, 052712 (2004).
[19] W. Domcke, Phys. Rep. **208**, 97 (1991).
[20] M. Berman, C. Mundel, and W. Domcke, Phys. Rev. A **31**, 641 (1985).
[21] E. P. Wigner, Phys. Rev. **73**, 1002 (1948).
[22] M. Čížek, J. Horáček, and W. Domcke, Phys. Rev. A **60**, 2873 (1999).
[23] M. Berman, C. Mündel, and W. Domcke, Phys. Rev. A **31**, 641 (1985).
[24] K. Houfek, M. Čížek, and J. Horáček, Phys. Rev. A **66**, 062702 (2002).
[25] Y. P. Zhang, C. H. Cheng, J. T. Kim, J. Stanojevic, and E. E. Eyler, Phys. Rev. Lett. **92**, 203003 (2004).
[26] J. S. Cohen, Rep. Prog. Phys. **67**, 1769 (2004).

B.2 Phys. Rev. A 86, 032714

Isotope effect for associative detachment: $H(D)^- + H(D) \rightarrow H_2(D_2) + e^-$ K. A. Miller, H. Bruhns, M. Čížek, J. Eliášek, R. Cabrera-Trujillo, H. Kreckel, A. P. O'Connor, X. Urbain, and D. W. Savin
Phys. Rev. A **86**, 032714 - Published 27 September 2012

Isotope effect for associative detachment: $H(D)^- + H(D) \rightarrow H_2(D_2) + e^-$

K. A. Miller,[1] H. Bruhns,[1,*] M. Čížek,[2] J. Eliášek,[2] R. Cabrera-Trujillo,[3] H. Kreckel,[1,†]
A. P. O'Connor,[1] X. Urbain,[4] and D. W. Savin[1]

[1]*Columbia Astrophysics Laboratory, Columbia University, 550 West 120th Street, New York, New York 10027, USA*
[2]*Charles University Prague, Faculty of Mathematics and Physics, Institute of Theoretical Physics, 180 00 Praha 8, Czech Republic*
[3]*Instituto de Ciencias Físicas, Universidad Nacional Autónoma de México, Ap. Postal 48-3, Cuernavaca, Morelos, 62251, Mexico*
[4]*Institute of Condensed Matter and Nanosciences, Université Catholique de Louvain, Louvain-la-Neuve B-1348, Belgium*

(Received 1 March 2012; published 27 September 2012)

We report experimental and theoretical results for associative detachment (AD) of $D^- + D \rightarrow D_2 + e^-$. We compare these data to our previously published results for $H^- + H \rightarrow H_2 + e^-$. The measurements show no significant isotope effect in the total cross section. This is to be contrasted with previously published experimental and theoretical work which has found a significant isotope effect in diatomic systems for partial AD cross sections, i.e., as a function of the rotational and vibrational levels of the final molecule formed. Our work implies that though the rovibrational distribution of flux is different for AD of H^- + H and D^- + D, the total flux for these two systems is essentially the same when summed over all possible final channels.

DOI: 10.1103/PhysRevA.86.032714 PACS number(s): 34.50.Lf, 52.20.Hv, 95.30.Ft, 97.10.Bt

I. INTRODUCTION

One of the most fundamental systems for atomic collision studies is the associative detachment (AD) reaction

$$H^- + H \rightarrow H_2 + e^- \quad (1)$$

and its isotopic counterpart

$$D^- + D \rightarrow D_2 + e^-. \quad (2)$$

Only recently, after more than 40 years of effort, have experiment and theory finally converged for reaction (1) [1–3]. However, we know of no published experimental data for reaction (2) and of theory only the results for the 14–17 meV center-of-mass energy range, displaying a small resonance behavior [4].

There are good reasons to suspect an isotope effect in the partial AD cross sections for reactions (1) and (2). For the same collision energy, D moves more slowly than H and penetrates less deeply into the electron cloud of the anion before detachment occurs. The resulting deuterated molecule forms at higher internuclear distances and higher vibrational levels than for the undeuterated molecule [5]. This was seen by the only experimental AD studies we know of which investigate the isotope effect for two-atom collision systems [5,6]. In Ref. [5] experimental and theoretical work was carried out for AD of H and D with Cl^- and Br^- by measuring the relative cross section as a function of the detached electron energy. For AD of $H + F^-$ and $D + F^-$ [6] the relative vibrational level v populations of the resulting HF and DF were determined by measuring the infrared spectra from the excited rovibrational states. These results were supported by later theoretical work [7]. All of these works found a pronounced isotope effect in the partial AD cross section: higher v levels are populated in the deuterated reactions.

Knowledge of reactions (1) and (2) comes also from studies of the time reversed processes of dissociative electron attachment (DEA), namely

$$e^- + H_2 \rightarrow H^- + H \quad (3)$$

and

$$e^- + D_2 \rightarrow D^- + D. \quad (4)$$

Such results can shed light on the AD process by using detailed balance to map the initial molecular rovibrational state in DEA onto the corresponding final state in AD.

Only a few experimental studies exist for reactions (3) and (4). DEA measurements of D_2 found that the cross section at room temperature is at least a couple orders of magnitude smaller than that for H_2 [8–10]. The molecules in these studies were essentially in their ground rovibrational level, suggesting a strong isotope effect for AD into that level. However, AD proceeds primarily through high rovibrational levels [4]. The v dependence of the DEA cross section was studied experimentally by Ref. [11] who found that DEA for D_2 grew more rapidly with v than that for H_2. Various theoretical studies support this trend (reviewed by Ref. [12]), though [13] found that the isotope effect disappears for $v \gtrsim 9$.

Based on these DEA results, we would therefore expect a strong isotope effect in the partial AD cross sections leading to low-lying vibrational states and a weak effect for higher vibrational states. However, it is not clear *a priori* which trend wins out in the total AD cross section. For example, our AD calculations for a series of hydrogen halides show that the isotope effect becomes more important for heavier halogen anions [14].

The total AD cross section can be analyzed theoretically using classical trajectory theories as well as both a classical and quantum opacity function for a given trajectory or partial wave. These approaches all indicate that the total AD cross sections for reactions (1) and (2) are insensitive to the detailed quantum dynamics in the autodetachment region, which occurs for internuclear distances $R < 3a_0$, and that no isotope effect is expected. Systems entering this region rapidly undergo

*Present address: Inficon GmbH, D-50968 Cologne, Germany.
†Present address: Max-Planck-Institut för Kernphysik, Saupfercheckweg 1, 69117 Heidelberg, Germany.

autodetachment resulting in AD. As a consequence, the total AD cross section can be predicted by just calculating which classical trajectories end up in the autodetachment region.

The radial motion of each trajectory with an impact parameter b and relative collision energy E_r is governed by the effective potential

$$V(b,R) = V_i(R) + \frac{b^2 E_r}{R^2}, \tag{5}$$

where $V_i(R)$ is the interaction potential for $H^- + H$ in the absence of any angular momentum and $b^2 E_r/R^2$ is the centrifugal barrier term. Taking $b_c(E_r)$ as the critical value of the impact parameter at which the centrifugal term just prevents the particles from reaching the autodetachment region, then the total AD cross section can be simply given by the geometric cross section

$$\sigma_{AD} = \pi b_c^2. \tag{6}$$

This model only depends on the particle trajectories. Since these trajectories are a function of energy and not velocity, the resulting cross section is independent of mass. We also note that for some potentials it is easy to derive an analytical expression for $b_c(E_r)$. For example, using the polarization potential $V_i(R) = -\alpha/R^4$ in Eq. (6), where α is the polarizability, yields the Langevin cross section $\sigma_L = \pi\sqrt{4\alpha/E_r}$ [15].

The above classical trajectory analysis assumes that every collision crossing into the autodetachment region contributes to AD. For a slightly more involved treatment we can introduce the opacity function $O(b,E_r)$, which gives the probability of the autodetachment for a collision along a trajectory characterized by a given collision energy E_r and impact parameter b. The AD cross section then reads

$$\sigma_{AD}(E_r) = \int 2\pi b\, O(b,E_r) db. \tag{7}$$

This reduces to Eq. (6) if we assume that $O = 1$ for $b < b_c$ and $O = 0$ otherwise. This is a reasonable assumption for a process characterized by a fast autodetachment rate, but in general the opacity function depends on the particle velocity along the trajectory and may thus exhibit an isotope effect.

The explanation of the near disappearance of the isotopic effect can also be derived from a partial wave expansion in the full quantum mechanical treatment. The formula for the cross section can then be written as

$$\sigma_{AD} = \frac{\pi}{2\mu E_r} \sum_L w_L (2L+1) O_L(E_r), \tag{8}$$

where L is the angular momentum, w_L is a statistical weight factor taking into account both nuclear spin and electronic symmetry, and $O_L(E_r) < 1$ is the opacity for the given partial wave. The opacity function is equal to the detachment probability for each partial wave and can be calculated from the partial S-matrix for AD [7,15].

Although Eq. (8) is the exact formula, it gives very similar results for the total AD cross section as does the classical approach. To see this, again we assume that the opacity is approximately equal to one when the incident partial wave L can overcome the centrifugal barrier

$$\frac{L(L+1)}{2\mu R^2} = \frac{b^2 E_r}{R^2}, \tag{9}$$

and enter into the autodetachment region. The opacity is also assumed to be zero when the incident partial waves are shielded from this region. Ignoring the L dependence of the factor w_L, the sum over L produces the factor L_c^2, where L_c is the critical value of L for which O_L vanishes. Using the classical relation between the angular momentum and the impact parameter

$$L_c = b_c\sqrt{2\mu E_r}, \tag{10}$$

one can readily transform Eq. (8) to Eq. (6). The inclusion of the L dependence of w_L, the discrete nature of L_c, and the exact form of O_L all produce a small isotope effect as we will discuss in detail in a subsequent paper focusing on the theory of the reaction.

We conclude that when the opacity function is one for small L and switches rapidly to zero at a certain critical value of L, then both classical and quantum reasoning predicts there will be no isotope effect in the total AD cross section. Such behavior of the opacity function is not automatic as can be demonstrated for the case of hydrogen halides [7]. The opacity function can be expected to switch rapidly from one to zero only if the region of internuclear distances where autodetachment is fast is followed almost immediately by a region where autodetachment is forbidden. Regions of internuclear distances with weak autodetachment would lead to mass dependence in the opacity function and thus to an isotope effect in the total AD cross section.

In an attempt to test these simple theoretical predictions for the isotope effect in the total AD cross section, we have performed both laboratory measurements and fully quantum mechanical theoretical calculations of the total cross section for reaction (2) versus relative collision energy E_r. Our experimental and theoretical approaches have been previously described in detail in Refs. [1–4,16]. Here we give only brief overviews of each.

The rest of this paper is organized as follows. In Sec. II we describe the experimental method. Section III presents our theoretical calculations. We present and discuss our results in Sec. IV. A summary is given in Sec. V.

II. EXPERIMENTAL METHOD

The experiment begins by creating a D_2 plasma in a duoplasmatron ion source. A beam of negative particles is extracted from the source by floating the duoplasmatron to a potential of $U_s \approx -10$ kV. Using charge-to-mass analysis, we form a D^- beam which we further shape and direct into a floating cell at a negative potential U_f. Upon entering the cell, the anions slow down. They are then crossed with a 975-nm laser beam which photodetaches ~10% of the D^-. This creates a beam of ground state, neutral atomic D with a kinetic energy of $\approx -e(U_s - U_f)$, where e is the unit charge. The resulting self-merged, anion-neutral beams exit the floating cell, whereupon the anions return to their initial kinetic energy of $\approx -eU_s$, while that of the neutral atoms remains fixed at $\approx -e(U_s - U_f)$. The exact details are given in Ref. [2]. We varied U_f to set the relative energy E_r.

The merged beams continue into the interaction region where D_2 is formed with a kinetic energy of ≈20 keV. The beginning of this region is defined by a chopping electrode which can be used to deflect the anions and prevent them from

entering the interaction region. We chop the neutrals on and off by switching the laser on and off. By chopping both beams out of phase, we are able to extract any signal D_2 generated in the interaction region from background generated anywhere in the apparatus. Beam profile monitors near the beginning and end of the interaction region allow us to measure the profile of each beam and determine the average overlap form factor of the two beams $\langle\Omega(z)\rangle$ along the z axis set by the trajectory of the overlapping beams. The end of the interaction region is defined by quadrupole electrodes which deflect the anions into a Faraday cup where the current I_{D^-} is measured. The neutral D and daughter D_2 continue into a helium gas cell where a fraction of each are ionized by electron stripping forming $\approx$10 keV D^+ and $\approx$20 keV D_2^+. The remaining neutrals and resulting cations pass into an electrostatic analyzer which consists of a series of cylindrical deflectors. A hole in the outer plate of the lower cylindrical deflector allows the neutral D (and the $\sim 10^{-9}$ smaller amount of D_2) to pass through and continue into a neutral particle detector where we measure the D particle current I_D, expressed in amperes. The voltages on the lower and upper cylindrical deflectors are set to direct the $\approx$20 keV D_2^+ ions onto a channel electron multiplier (CEM) where their rate is measured and recorded as a function of the chopping pattern.

The experiment measures the AD cross section σ_{AD} times the relative velocity between the two beams v_r convolved with the energy spread of the experiment. The energy spread is described in detail in Ref. [2]. The resulting rate coefficient is given by

$$\langle\sigma_{AD}v_r\rangle = \frac{1}{\sigma_{st}N_{He}}\frac{S}{T_aT_g\eta}\frac{e^2}{I_{D^-}I_D}\frac{v_{D^-}v_D}{L\langle\Omega(z)\rangle}. \tag{11}$$

Here σ_{st} is the stripping cross section for D_2 on He; N_{He} is the helium column density in the gas cell; S is the background-subtracted D_2^+ signal corrected for collisionally induced signal loss in the gas cell and energy analyzer; T_a is the transmittance of the energy analyzer; T_g is the transmittance of the grid in front of the CEM; v_{D^-} and v_D are the velocities of the D^- and D beams, respectively; and L is the length of the interaction region. Using our experimental energy spread and the theoretical results described below, we find that the cross section can be accurately extracted from the measured rate coefficient as

$$\sigma_{AD} = \frac{\langle\sigma_{AD}v_r\rangle}{\langle v_r\rangle}, \tag{12}$$

with $\langle v_r\rangle$ averaged over the experimental velocity distribution in the center of mass frame.

Table I lists the experimental nonstatistical uncertainties. Throughout this paper, all uncertainties are given at an estimated 1σ statistical confidence level. We give the errors for our present D results as well as our previous H results for comparison. All uncertainties are treated as uncorrelated and added in quadrature.

When comparing results within a given isotope, the relative error is given by the uncertainties in the background subtraction, beam current measurements, and overlap of the beams. This sum is 12% for each isotope and is dominated by the neutral detector calibration which uses the method outlined in Ref. [3] for H. The detector efficiency for D was calibrated by passing a D^- beam through the helium gas cell as a function of helium pressure and recording both the transmitted D^- and the neutral detector signal. A small correction needs to be made for the unmeasured D^+ generated in the gas cell. For this we used the velocity matched H^- cross sections from Refs. [17,18] for the required D^- single and double electron detachment cross sections. The uncertainties in the detachment cross sections have an insignificant effect on the measured calibration. The dominant uncertainty in the neutral detector calibration is due to the reproducibility of the measured efficiencies.

TABLE I. Summary of nonstatistical experimental uncertainties at an estimated 1σ confidence level. Uncertainties are treated as uncorrelated and added in quadrature. The errors for reaction (1) and (2) are listed separately.

Source	H(%)	D(%)
Background subtraction	5	5
Anion current	3	3
Neutral current	10	10
Overlap of beams	3	3
Relative error within an isotope	12	12
Stripping cross section	16	17
Effects of unknown rovibrational population	10	10
Signal attenuation	1	2
Relative error between isotopes	22	22
Analyzer transmittance	1	1
Grid transmittance	1	1
CEM detection efficiency	2	2
Overlap length	1	1
Helium gas cell column density	7	7
Total nonstatistical uncertainty	24	24

In order to make comparisons between isotopes, one needs to take into account uncertainties that vary between the data sets. These include σ_{st}, the effects of the unknown rovibrational population of the molecules formed, and the collisional destruction of the signal cations before detection. For σ_{st} of D_2 we used the velocity matched results of Ref. [19] for H_2 yielding $(7.7 \pm 1.3) \times 10^{-17}$ cm^2. We corrected for the collisional destruction of the signal D_2^+ using the approach described in Ref. [3]. For the necessary destruction cross section we used the velocity matched results for H_2^+ on He from Ref. [20]. The quadrature sum for the relative error is 22%.

The total nonstatistical error of our measurements for both isotopes is 24% at an estimated 1σ statistical level. This reflects the quadrature sum of all uncertainties listed in Table I. The measurement uncertainties are reviewed in further detail in Refs. [1–3].

III. THEORETICAL METHOD

A. Cross section calculations

The AD cross section calculations for reaction (2) are essentially the same as our previous work for reaction (1) [3]. The basic framework is the nonlocal resonance model described in Ref. [4]. The incoming $H^- + H$ particles move in the attractive potential of the H_2^- $^2\Sigma_u^+$ state, until they penetrate into the $H_2 + e^-$ electronic continuum by crossing

TABLE II. AD cross sections σ_{AD} as a function of relative collision energy $\langle E_r \rangle$. The quoted error represents the 1σ statistical uncertainty.

	σ_{AD} (10^{-16} cm^2)					
	H			D		
$\langle E_r \rangle$ (eV)	Experiment	Error	Theory	Experiment	Error	Theory
0.00374	456	25.4	340	494	39.5	340
0.00418	476	36.1	331	421	60.2	330
0.00524	370	22.1	313	451	33.6	311
0.00665	348	27.3	294	371	48.2	293
0.00898	303	17.0	270	365	26.3	270
0.0119	251	19.9	240	321	38.3	244
0.0155	222	12.3	203	285	19.3	212
0.0197	212	15.9	171	250	29.1	170
0.0245	177	9.64	140	218	15.2	138
0.0300	142	11.8	116	162	19.8	115
0.0361	129	6.52	97.6	147	11.0	96.2
0.0428	96.9	8.96	83.3	111	16.7	81.9
0.0501	84.3	6.13	71.9	105	7.65	70.5
0.0580	68.2	6.81	62.7	83.1	13.0	61.3
0.0666	59.6	5.24	55.1	65.4	7.36	53.8
0.0758	57.7	6.14	48.9	74.0	11.2	47.6
0.0856	47.7	2.92	43.6	65.5	5.27	42.4
0.0961	49.5	5.63	39.2	–	–	–
0.107	42.3	3.59	35.4	47.1	7.08	35.0
0.131	31.9	2.22	29.3	48.0	4.53	29.2
0.158	39.3	3.67	24.7	–	–	–
0.187	23.2	1.87	21.1	38.0	5.13	21.5
0.218	24.5	2.46	19.0	–	–	–
0.252	18.9	1.56	17.1	24.1	3.94	16.9
0.289	19.0	1.54	15.4	–	–	–
0.328	15.0	1.46	14.0	19.4	3.44	14.0
0.369	18.6	1.66	12.8	–	–	–
0.413	13.9	1.30	11.7	17.8	3.26	11.8
0.460	14.7	1.50	10.8	–	–	–
0.509	10.5	1.17	10.0	15.5	2.98	10.1
0.560	10.1	1.40	9.39	–	–	–
0.614	9.46	1.13	8.88	16.0	2.49	9.07
0.671	9.09	1.20	8.50	–	–	–
0.730	9.18	1.01	8.22	11.4	2.08	8.86
0.791	9.83	0.892	8.06	–	–	–
0.855	7.71	0.890	7.96	14.1	1.96	8.50
0.922	6.57	1.09	7.71	–	–	–
0.991	6.30	0.821	7.38	12.3	1.86	7.55
1.06	7.56	0.953	6.98	–	–	–
1.14	8.08	1.84	6.53	5.85	2.10	6.57
1.21	6.01	0.875	6.04	–	–	–
1.29	6.36	1.50	5.51	–	–	–
1.37	4.48	0.738	4.97	–	–	–
1.46	4.95	1.14	4.42	5.29	1.67	4.27
1.54	5.07	0.565	3.88	–	–	–
1.63	3.29	0.908	3.35	–	–	–
1.72	3.16	0.666	2.85	–	–	–
1.82	1.98	0.761	2.38	1.85	1.13	1.97
1.91	1.02	0.689	1.96	–	–	–
2.01	0.774	0.861	1.58	–	–	–
2.12	1.62	0.579	1.26	–	–	–
2.22	1.74	0.822	0.994	−0.09	1.09	0.540
2.33	0.572	0.527	0.781	–	–	–
2.44	1.28	0.469	0.619	–	–	–
2.55	1.08	0.318	0.502	–	–	–

TABLE II. *Continued.*

	σ_{AD} (10^{-16} cm^2)					
	H			D		
$\langle E_r \rangle$ (eV)	Experiment	Error	Theory	Experiment	Error	Theory
2.66	0.564	0.463	0.420	2.51	1.51	0.176
2.78	0.880	0.316	0.358	–	–	–
2.90	1.27	0.401	0.299	–	–	–
3.02	0.628	0.282	0.219	–	–	–
3.14	0.585	0.565	0.218	2.87	1.45	0.0780
3.27	0.222	0.311	0.198	–	–	–
3.40	0.782	0.331	0.183	–	–	–
3.53	0.722	0.397	0.173	–	–	–
3.66	0.698	0.465	0.167	–	–	–
3.80	−0.068	0.364	0.163	–	–	–
3.94	0.390	0.377	0.161	–	–	–
4.22	0.136	0.322	0.161	–	–	–
4.52	0.328	0.303	0.163	–	–	–
4.83	0.141	0.261	0.168	–	–	–

the potential energy curve of the H_2 $^1\Sigma_g^+$ state. The dynamics of nuclear motion are described by the nonlocal energy dependent potential [4,21]. In Ref. [3] we extended this picture to include the contributions of the repulsive H_2^- $^2\Sigma_g^+$ state, in a similar way as Belyaev *et al*. [22], which increases the cross section by about 15% for energies $\gtrsim$0.75 eV.

There are really only two significant differences in the theoretical description for the $D^- + D$ collisions versus the $H^- + H$ case. First, the reduced mass is about two times larger for the deuterated case. This number is easily included in the new calculation, leading to a larger number of partial wave contributions and a larger number of rovibrationally excited D_2 states produced compared to H_2. Second, the deuteron is a boson with spin 1 as compared to spin 1/2 in the case of the fermionic proton. This leads to a different nuclear spin weighting factor for deuterium as compared to hydrogen.

Lastly, AD can produce molecules in highly rotationally excited states which lie above the separate atom limit but are metastable due to the angular momentum centrifugal barrier [3]. These orbiting resonances have angular momentum up to $\approx$30(40) for $H_2(D_2)$ and lifetimes well exceeding the $\approx$1 μs flight time from the interaction region to the detector. Here we included the contribution of these metastable states in our AD cross section calculations, as they contribute to the measured cross section.

B. Scattering simulations of the signal ions

We have investigated the possible scattering effects on the signal H_2^+ and D_2^+ generated by stripping of the AD products in the He gas cell. The scattering cones for each ion could differ, resulting in unequal collection efficiencies for the H_2^+ and D_2^+ signal. Measured from the midpoint of the gas cell, the half angle for the geometric acceptance angle of our CEM is 0.4°, though the actual acceptance half angle is likely to be larger due to focusing effects in the electrostatic analyzer.

Scattering calculations were performed from an electron nuclear dynamics approach. This method uses a time dependent variational principle to derive an approximation to the time-dependent Schrödinger equation (see Refs. [23,24] for further details). The simulations indicate that 97% of the scattered H_2^+ and 99% of the scattered D_2^+ are contained within the CEM half-angle cone of 0.4°. Here we make the assumption that these numbers are 100%, an approximation which has an insignificant effect on the total experimental uncertainty.

IV. RESULTS AND DISCUSSION

The measured H and D data were first collected in November of 2008 using the approach of Refs. [1,2]. Then, using the approach of Ref. [3], the H data were remeasured from January to July of 2010 and the D data from March to July of 2011. Good agreement between the two approaches was found for the H data [3] and we merged the sets together using a statistically weighted averaging method. The D data sets show similar good agreement and we have merged the two data sets using the same averaging method as for the H data. This level of agreement between data sets collected using slightly different approaches and spanning nearly three years gives us a high degree of confidence in the stability of the apparatus over this time.

Our results for reactions (1) and (2) are shown in Fig. 1. The results in red are for deuterium and those in black for hydrogen. The error bars display the 1σ statistical error of the experimental results. The data for hydrogen and deuterium are also presented in Table II. Additionally, we plot the Langevin value [4,25]. This has been reduced by a factor of 2 to take into account that AD proceeds primarily via the H_2^- $^2\Sigma_u^+$ state and the contribution of the $^2\Sigma_g^+$ state is negligible to first order.

Table II presents the cross sections for these reactions in units of cm^2. In Fig. 1, though, we have multiplied the cross section data by $\langle E_r \rangle^{1/2}$. This effectively removes any Langevin-like behavior in the cross section [25]. Were the reaction truly Langevin-like, the resulting $\sigma_{AD}\langle E_r \rangle^{1/2}$ would be independent of $\langle E_r \rangle$. The structure shown in Fig. 1 demonstrates the remaining non-Langevin behavior in the reaction. For energies between $\sim$3 meV and $\sim$1 eV the reaction is faster than Langevin. This is caused by the fact that the

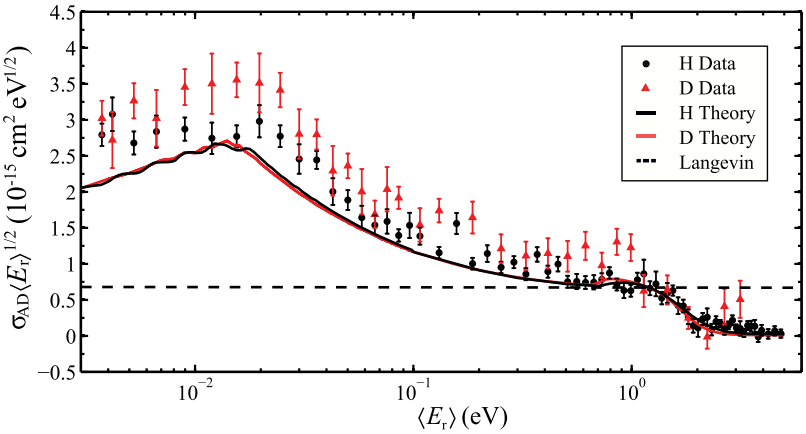

FIG. 1. (Color) Scaled AD cross section versus relative collision energy for reaction (1) is shown in black and for reaction (2) in red. The filled circles are the measured results for the hydrogen and the filled triangles for deuterium. The error bars on each point give the associated 1σ statistical error. The solid curves present our theoretical results, while the dashed line is the Langevin value.

long range interaction potential for $H^- + H$ at distances of $3a_0 - 20a_0$ is much more attractive than indicated by the dipole polarizability of the hydrogen atom. Above ~1 eV, the reaction rapidly turns off due to the opening of the collisional detachment channel

$$H(D)^- + H(D) \rightarrow H(D) + H(D) + e^-, \qquad (13)$$

a process which is not accounted for by the Langevin cross section.

As discussed earlier, theory predicts no significant isotope effect in the total cross section for reactions (1) and (2). Comparing only the two experimental data sets, our measured results are also consistent with there being no isotope effect in the total AD cross section. For a quantitative comparison we focus on energies $\lesssim$0.75 eV, where AD can proceed only via the attractive $^2\Sigma_u^+$ state and which is also below the threshold for collisional detachment [Eq. (13)]. The ratio of the D to H data sets is 1.21 ± 0.03, which is effectively within the estimated 22% relative error between the isotopes.

Comparing the theoretical to the experimental results, for the corresponding energies below 0.75 eV, yields ratios of 0.84 ± 0.01 for the H data and 0.70 ± 0.06 for the D data. With an estimated total nonstatistical uncertainty of 24%, we find good agreement between theory and experiment for the H data, as has been previously reported [1–3]. For the D data, the experimental results differ from theory only at an $\approx 1.25\sigma$ level, which we interpret as being in agreement.

As discussed in the Introduction the lack of an isotope effect is related to both the fast autodetachment rate at small internuclear separations of H^- and H and the fact that the trajectories depend only on the energy and not the mass of the particles. That said, the calculations do indicate that there is a small isotope effect due to nuclear spin at low energies. Additionally, at energies $\gtrsim$0.75 eV, the small differences seen in the predicted cross sections are due to threshold effects associated with opening of the $H(D) + H(D) + e^-$ channel and due to the contribution of the repulsive $^2\Sigma_g^+$ state. These differences are too small to be discernible in our measurements.

V. CONCLUSION

Previous experimental and theoretical work has demonstrated the existence of a large isotope effect for the partial AD cross section of diatomic collision systems. Our theoretical results show no such effect in the total AD cross section for the $H^- + H$ and $D^- + D$ systems studied here. The new experimental data are consistent with this as well as with both the energy dependence and magnitude of the theoretical calculations. Taken all together, our results indicate that though the predicted rovibrational distribution of flux is different for each system, the total flux is essentially the same. We expect to see similar behavior for the AD isotope effect in other collision systems possessing an attractive long range potential where autodetachment is essentially forbidden leading to a region where fast autodetachment turns on and stays on.

ACKNOWLEDGMENTS

The authors thank M. Hahn for stimulating discussions. This work was supported in part by NSF Grants No. CHE-0520660, No. AST-0606960, and No. AST-0807436. H.B. was supported in part by the German academic exchange service DAAD. M.Č. and J.E. were supported in part by Grant No. GACR 208/10/1281 from the Czech Republic. X.U. acknowledges support from the Fund for Scientific Research (FNRS).

[1] H. Kreckel, H. Bruhns, M. Čížek, S. C. O. Glover, K. A. Miller, X. Urbain, and D. W. Savin, Science **329**, 69 (2010).

[2] H. Bruhns, H. Kreckel, K. A. Miller, X. Urbain, and D. W. Savin, Phys. Rev. A **82**, 042708 (2010).

[3] K. A. Miller, H. Bruhns, J. Eliášek, M. Čížek, H. Kreckel, X. Urbain, and D. W. Savin, Phys. Rev. A **84**, 052709 (2011).
[4] M. Čížek, J. Horáček, and W. Domcke, J. Phys. B **31**, 2571 (1998).
[5] S. Živanov, M. Čížek, J. Horáček, and M. Allan, J. Phys. B **36**, 3513 (2003).
[6] M. A. Smith and S. R. Leone, J. Chem. Phys. **78**, 1325 (1983).
[7] M. Čížek, J. Horáček, F. A. U. Thiel, and H. Hotop, J. Phys. B **34**, 983 (2001).
[8] D. Rapp, T. E. Sharp, and D. D. Briglia, Phys. Rev. Lett. **14**, 533 (1965).
[9] G. J. Schulz and R. K. Asundi, Phys. Rev. Lett. **15**, 946 (1965).
[10] E. Krishnakumar, S. Denifl, I. Čadež, S. Markelj, and N. J. Mason, Phys. Rev. Lett. **106**, 243201 (2011).
[11] M. Allan and S. F. Wong, Phys. Rev. Lett. **41**, 1791 (1978).
[12] J. Horáček, M. Čížek, K. Houfek, P. Kolorenč, and W. Domcke, Phys. Rev. A **70**, 052712 (2004).
[13] Y. Xu and I. I. Fabrikant, Appl. Phys. Lett. **78**, 2598 (2001).
[14] K. Houfek, M. Čížek, and J. Horáček, Phys. Rev. A **66**, 062702 (2002).
[15] J. P. Gauyacq, *Dynamics of Negative Ions*, Lecture Notes in Physics Vol. 15 (World Scientific, Singapore, 1987).
[16] H. Bruhns, H. Kreckel, K. Miller, M. Lestinsky, B. Seredyuk, W. Mitthumsiri, B. L. Schmitt, M. Schnell, X. Urbain, M. L. Rappaport, C. C. Havener, and D. W. Savin, Rev. Sci. Instrum. **81**, 013112 (2010).
[17] T. J. Kvale, J. S. Allen, X. D. Fang, A. Sen, and R. Matulioniene, Phys. Rev. A **51**, 1351 (1995).
[18] Atomic Data for Fusion. Vol. 1, edited by C. F. Barnett, Oak Ridge National Laboratory Report No. ORNL-6086, 1, F-12 (1990), http://www-cfadc.phy.ornl.gov/redbooks/redbooks.html.
[19] R. Browning, C. J. Latimer, and H. B. Gilbody, J. Phys. B **3**, 667 (1970).
[20] Y. Suzuki, T. Kaneko, M. Tomita, and M. Sakisaka, Phys. Soc. Jpn. **55**, 3037 (1986).
[21] W. Domcke, Phys. Rep. **208**, 97 (1991).
[22] A. K. Beylaev, A. S. Tiukanov, and W. Domcke, Chem. Phys. **325**, 378 (2006).
[23] R. Cabrera-Trujillo, Y. Öhrn, E. Deumens, and J. R. Sabin, J. Chem. Phys. **116**, 2783 (2002).
[24] E. Deumens, A. Diz, H. Taylor, and Y. Öhrn, J. Chem. Phys. **96**, 6820 (1992).
[25] G. Gioumousis and D. P. Stevenson, J. Chem. Phys. **29**, 294 (1958).